



Isogeometric shell analysis and optimization for structural dynamics

Zhen Lei

► To cite this version:

Zhen Lei. Isogeometric shell analysis and optimization for structural dynamics. Other. Ecole Centrale de Lyon, 2015. English. NNT : 2015ECDL0028 . tel-01355101

HAL Id: tel-01355101

<https://theses.hal.science/tel-01355101v1>

Submitted on 22 Aug 2016

HAL is a multi-disciplinary open access archive for the deposit and dissemination of scientific research documents, whether they are published or not. The documents may come from teaching and research institutions in France or abroad, or from public or private research centers.

L'archive ouverte pluridisciplinaire **HAL**, est destinée au dépôt et à la diffusion de documents scientifiques de niveau recherche, publiés ou non, émanant des établissements d'enseignement et de recherche français ou étrangers, des laboratoires publics ou privés.

ÉCOLE CENTRALE DE LYON

École Doctorale Mécanique, Énergétique, Génie Civil et Acoustique

THÈSE

Isogeometric shell analysis and optimization for structural dynamics

Soutenue le 12 octobre 2015

par

Zhen LEI

en vue d'obtenir le titre de

DOCTEUR DE L'ÉCOLE CENTRALE DE LYON

spécialité

MÉCANIQUE

Devant le jury composé de :

S. COGAN	Charge de Recherche HDR, FEMTO-ST	<i>Rapporteur</i>
T. TISON	Professeur, Univ. de Valenciennes	<i>Rapporteur</i>
A. GRAVOUIL	Professeur, LaMCoS, INSA Lyon	<i>Président</i>
L. JÉZÉQUEL	Professeur, LTDS, ECL	<i>Directeur</i>
F. GILLOT	Maitre de conférences, LTDS, ECL	<i>Co-encadrant</i>

Remerciements

Cette thèse à été réalisée au Laboratoire de Tribology et Dynamique des Systèmes de l'École Centrale de Lyon sous la direction du professeur L.Jézéquel et de monsieur F.Gillot. Je remercie chaleureusement mon directeur de recherche professeur L.Jézéquel pour m'avoir proposé ce sujet et m'avoir aidé durant ces trois années. Son attention et ses encouragements ont alimenté ma recherche.

Je remercie également monsieur F.Gillot pour son aide scientifique. Sa patience, ses conseils ont été précieux tout au long de ces trois années.

Je remercie le professeur A.Gravouil de me faire l'honneur de présider le jury. Je remercie très sincèrement le professeur S.Cogan et monsieur T.Tison qui ont accepté d'être les rapporteurs de mon travail.

Pour la financement de ce travail, je remercie le conseil des bourses d'études de la Chine (China Scholarship Council, CSC) et le service de l'éducation de l'ambassade de Chine en France pour avoir financé mes études en France.

Je souhaite aussi adresser mes remerciements à ma famille et à mes amis. Sans leurs encouragements et leur support de la manière constante, je n'aurais pas pu passer certains moments difficiles.

Résumé

Cette thèse présente des travaux effectués dans le cadre de l'optimisation de forme de pièces mécaniques, sous critère dynamique, par approche isogéométrique. Pour réaliser une telle optimisation nous mettons en place dans un premier temps les éléments coque au travers des formulations Kirchhoff-Love puis Reissner-Mindlin. Nous présentons une méthode permettant d'atteindre les vecteurs normaux aux fibres dans ces formulations au travers de l'utilisation d'une grille mixte de fonctions de base interpolantes, traditionnellement utilisées en éléments finis, et de fonction non interpolantes issues de la description isogéométrique des coques. Par la suite, nous détaillons une méthode pour le couplage de patch puis nous mettons en place la méthode de synthèse modale classique dans le cadre de structures en dynamique décrites par des éléments isogéométriques. Ce travail établit une base pour l'optimisation de forme sous critères dynamique de telles structures. Enfin, nous développons une méthode d'optimisation de forme basée sur le calcul du gradient de la fonction objectif envisagée. La sensibilité de conception est extraite de l'analyse de sensibilité au niveau même du maillage du modèle, qui est obtenue par l'analyse discrète de sensibilité. Des exemples d'application permettent de montrer la pertinence et l'exactitude des approches proposées.

Mots clés: Méthode isogéométrique, Reissner-Mindlin coque, Kirchhoff-Love coque, couplage de patch, synthèse modale, l'optimisation de forme, l'analyse de sensibilité

Acknowledgements

I spend three years in Ecole Centrale de Lyon for preparing this dissertation. There are a great number of people who provide me generous help in the past three years. Without their help, this dissertation would not have been successfully accomplished. I would like to express my sincere gratitude to all of them.

First of all, I would like to express my deep appreciation to my supervisor Professor Louis Jezequel and Doctor Frederic Gillot for accepting me as their student. I appreciate that they give me such an opportunity to stay in Lyon, a beautiful city in France, to prepare my doctoral thesis. I cannot thank them enough for their constant support, encouragement and advising. I also would like to thank Doctor Lyes Nechak, Doctor Renata Troian, Doctor Sebastien Besset for their advising and encouragement.

As a foreign student, without friends, I would not live in a happy life. I would like to thank my Chinese friends and colleagues for their help and encouragement. They are Zhou Changwei, Huang Xingrong, Huang Gang, Jiang Hong, Wang Yonghua, Li Zhe, Sun Xiangkun, Liu Xuchen, Ding He, Bai Yu, Shi Liu, etc. It is not possible to numerate all of them. I will never forget those wonderful moments that we spent together. I also would like to thank other French friends. They are Christophe Droz, Jean-Loup Christen, Mathieu Babaz, Krzysztof Sekua, Alexandr Lozak. I would like to thank all of them for their help.

I would like to thank my parents and my elder sister. It is with their love, help and encouragement that i gathered my courage to face the difficulties in my research. Without their successive support, i would not proceed so far in my research.

Finally, I also would like to acknowledge the China Scholarship Council for their financial support. It is their funding that makes my Doctoral work possible.

Abstract

Isogeometric method is a promising method in bridging the gap between the computer aided design and computer aided analysis. No information is lost when transferring the design model to the analysis model. It is a great advantage over the traditional finite element method, where the analysis model is only an approximation of the design model. It is advantageous for structural optimization, the optimal structure obtained will be a design model. In this thesis, the research is focused on the fast three dimensional free shape optimization with isogeometric shell elements. The related research, the development of isogeometric shell elements, the patch coupling in isogeometric analysis, the modal synthesis with isogeometric elements are also studied.

We proposed a series of mixed grid Reissner-Mindlin shell formulations. It adopts both the interpolatory basis functions, which are from the traditional FEM, and the non-interpolatory basis functions, which are from IGA, to approximate the unknown fields. It gives a natural way to define the fiber vectors in IGA Reissner-Mindlin shell formulations, where the non-interpolatory nature of IGA basis functions causes complexity. It is also advantageous for applying the rotational boundary conditions. A modified reduce quadrature scheme was also proposed to improve the quadrature efficiency, at the same time, relieve the locking in the shell formulations.

We gave a method for patch coupling in isogeometric analysis. It is used to connect the adjacent patches. The classical modal synthesis method, the fixed interface Craig-Bampton method, is also used as well as the isogeometric Kirchhoff-Love shell elements. The key problem is also the connection between adjacent patches. The modal synthesis method can largely reduce the time costs in analysis concerning structural dynamics. This part of work lays a foundation for the fast shape optimization of built-up structures, where the design variables are only relevant to certain substructures.

We developed a fast shape optimization framework for three dimensional thin wall structure design. The thin wall structure is modelled with isogeometric Kirchhoff-Love shell elements. The analytical sensitivity analysis is the key focus, since the gradient base optimization is normally more fast. There are two models in most optimization problem, the design model and the analysis

model. The design variables are defined in the design model, however the analytical sensitivity is normally obtained from the analysis model. Although it is possible to use the same model in analysis and design under isogeometric framework, it might give either a highly distorted optimum structure or a unreliable structural response. We developed a sensitivity mapping scheme to resolve this problem. The design sensitivity is extracted from the analysis model mesh level sensitivity, which is obtained by the discrete analytical sensitivity analysis. It provides flexibility for the design variable definition. The correctness of structure response is also ensured. The modal synthesis method is also used to further improve the optimization efficiency for the built-up structure optimization concerning structural dynamics criteria.

Keywords: Isogeometric Reissner-Mindlin shell, Kirchhoff-Love shell, multiple patches coupling, modal synthesis, shell structure optimization, design sensitivity analysis

Contents

Remerciements	i
Résumé	iii
Acknowledgement	v
Abstract	vii
Contents	ix
List of Figures	xiii
List of Tables	xix
List of Abbreviations	xxi
1 Introduction	1
1.1 Background	1
1.1.1 Shell structure	1
1.1.2 Isogeometric analysis	3
1.1.3 Structural optimization	4
1.2 Motivation	6
1.3 Outline	8
2 Basics on shell models and computer aided geometry design	11
2.1 Shell models deduction	12
2.1.1 Differential geometry	12
2.1.2 Continuum mechanics	13
2.1.3 Kirchhoff-Love shell model	16
2.1.4 Reissner-Mindlin shell model	19
2.2 Computer aided geometry design	22
2.2.1 B-spline	24
2.2.2 Non-uniform rational B-spline	29

2.2.3	NURBS operation	32
2.3	Isogeometric analysis	32
2.4	Summary	37
3	Isogeometric shell structure analysis	39
3.1	Linear Kirchhoff-Love shell	39
3.1.1	Isogeometric Linear Kirchhoff-Love shell implementation	40
3.1.2	Shell benchmark problems	42
3.2	Linear degenerated solid Reissner-Mindlin shell	45
3.3	Mixed grid Reissner-Mindlin formulation: NURBS and Lagrange basis functions	49
3.3.1	Formulations	50
3.3.2	Numerical examples	52
3.3.3	Discussions	58
3.4	Mixed grid Reissner-Mindlin formulation: NURBS and Serendipity basis functions	59
3.4.1	Formulations	59
3.4.2	Numerical examples	62
3.4.3	Discussions	62
3.5	Transverse shear locking test	65
3.6	Modified reduced quadrature scheme	68
3.6.1	Formulations	68
3.6.2	Numerical examples	72
3.7	Summary	75
4	Structural analysis with IGA on multiple domains	77
4.1	Isogeometric multiple patches analysis	77
4.1.1	Isogeometric analysis on multiple patches	77
4.1.2	Multiple patches coupling problem	79
4.1.3	Numerical examples	85
4.1.4	Discussion	94
4.2	Isogeometric modal synthesis	94
4.2.1	The Craig-Bampton method	95
4.2.2	Multiple domains coupling	97
4.2.3	Numerical examples	98
4.2.4	Discussion	107
4.3	Summary	107

5	Shape optimization	109
5.1	Introduction on the IGA based shape optimization	109
5.2	Sensitivity analysis	112
5.2.1	Element level sensitivity analysis	112
5.2.2	Sensitivity mapping	113
5.3	Numerical examples	116
5.4	Summary	121
6	Conclusion	123
6.1	Conclusions	123
6.1.1	Mixed grid IGA Reissner-Mindlin shell	123
6.1.2	Modal synthesis with Isogeometric shell elements	124
6.1.3	IGA based shape optimization	124
6.2	Future work	124
	Appendix	127
	References	131

CONTENTS

List of Figures

1.1	The Roman Pantheon, Italy.	1
1.2	The Anji bridge, China.	1
1.3	The FEM meshes of a cylindrical shell with different mesh densities.	4
1.4	The IGA meshes of a cylindrical shell with different mesh densities [79].	4
1.5	Different types of structural optimization problems, picture from [1].	6
1.6	Estimation of the relative time costs of each step in the engineering design circle, picture from [37]	7
2.1	The geometry of the shell body	12
2.2	The deformation process of the shell body	14
2.3	The deformation process of the Kirchhoff-Love shell body	17
2.4	The deformation process of the Reissner-Mindlin shell body	20
2.5	A three dimensional B-spline curve. The curve lies within the convex hull of the control polygon. The curve is composed of four quadratic polynomial curve pieces. The knot vector is $\Xi = \{0, 0, 0, 0.25, 0.5, 0.75, 0.75, 1, 1, 1\}$	25
2.6	The basis function $N_2(\xi)$ curve. It is composed of two pieces of quadratic polynomial curve. The full polynomial curves are also depicted. It is defined on $\Xi = \{0, 0, 0, 0.25, 0.5, 0.75, 0.75, 1, 1, 1\}$	26
2.7	The basis functions on $\Xi = \{0, 0, 0, 0.25, 0.5, 0.75, 0.75, 1, 1, 1\}$. There are seven quadratic basis functions.	26
2.8	A B-spline surface example.	27
2.9	The map from the parametric space $[0, 1]^2$ to \mathbb{R}^3 in a B-spline surface.	28
2.10	An example of bivariate B-spline, it can be viewed as an tensor product of the univariate ones. The univariate knot vectors are $\Xi_\xi = \Xi_\eta = \{0, 0, 0, \frac{1}{3}, \frac{2}{3}, 1, 1, 1\}$	28
2.11	An example of bivariate B-spline \hat{N}_3 , The univariate knot vectors are $\Xi_\xi = \Xi_\eta = \{0, 0, 0, \frac{1}{3}, \frac{2}{3}, 1, 1, 1\}$	29
2.12	B-spline curve projected to plane $w = 1$ to obtain an NURBS expressed arc.	30
2.13	An NURBS curve example.	30
2.14	An NURBS surface and the corresponding basis functions obtained by setting $w_{13} = 0.7$ in the B-spline surface 2.8.	31

LIST OF FIGURES

2.15	Insertion of new knot 0.3 into the knot vector $\{0, 0, 0, 1, 1, 1\}$. (a) and (b) show the curve before and after insertion, (c) and (d) show the corresponding basis functions.	33
2.16	Order elevation of a NURBS curve, the original knot vector is $\{0, 0, 0, 1, 1, 1\}$, the result knot vector is $\{0, 0, 0, 0, 1, 1, 1, 1\}$, (a) and (b) show the curve before and after insertion, (c) and (d) show the corresponding basis functions.	33
2.17	Examples of the IGA basis functions after refinements. Spline order and knot vectors : (a) $p=2$, $\Xi = \{0, 0, 0, 1, 1, 1\}$. (b) $p=2$, $\Xi = \{0, 0, 0, 0.3, 0.6, 1, 1, 1\}$. (c) $p=3$, $\Xi = \{0, 0, 0, 0, 1, 1, 1, 1\}$. (d) $p=3$, $\Xi = \{0, 0, 0, 0, 0.5, 1, 1, 1, 1\}$	35
3.1	IGA Kirchhoff-Love shell elements in parametric space (a) and physical space (b).	42
3.2	The scordelis-lo roof problem setup.	43
3.3	The pinched cylinder problem setup.	43
3.4	The hemisphere shell problem setup.	43
3.5	The u_z displacement at point A with different NURBS order IGA Kirchhoff-Love shell.	44
3.6	The u_z contour plot.	44
3.7	The deformed structure with a scaling factor 10.	44
3.8	The first 20 frequencies obtained with IGA and FEM, the quadratic NURBS are used.	45
3.9	An example of 3D shell shape description with NURBS basis and Lagrange basis. \mathbf{s} is expressed with NURBS basis. shell director \mathbf{v} with Linear Lagrange interpolation, basis points are the normal at points A , B and C . Normals of points D and E are obtained by interpolation.	51
3.10	An example of 2 order Lagrange (slash lines), 2 order NURBS basis functions and the Lagrange basis points positions (squares) in IGA elements $[0; 0.3]$ and $[0.3; 1]$	51
3.11	Scordelis-Lo roof, u_z vs number of elements per edges with quadratic Lagrange basis ($P_L = 2$) and various NURBS order.	53
3.12	Scordelis-Lo roof, u_z vs number of elements per edges with cubic Lagrange basis ($P_L = 3$) and various NURBS order.	53
3.13	Pinched Cylinder, u_z vs number of elements per edges with quadratic Lagrange basis ($P_L = 2$) and various NURBS order.	54
3.14	Pinched Cylinder, u_z vs number of elements per edges with cubic Lagrange basis ($P_L = 3$) and various NURBS order.	55
3.15	Pinched Cylinder, comparison of our approach with the one of Benson et al. [20] and [50]. Present approach: $p = 2$ indicates ($P_N = 2$, $P_L = 2$) and $p = 3$ ($P_N = 3$, $P_L = 3$), $p = 4$ ($P_N = 4$, $P_L = 3$)	56

3.16 Hemisphere shell, u_x vs number of elements per edges with quadratic Lagrange basis ($P_L = 2$) and various NURBS order.	56
3.17 Hemisphere shell, u_x vs number of elements per edges with cubic Lagrange basis ($P_L = 3$) and various NURBS order.	57
3.18 Double curved free form surface problem setup. Geometry data obtained from Dornisch et al. [50].	57
3.19 Double curved free surface, u_y variation with respect to the reference value ($u_y = 1.02786$) versus number of elements per edges. Results with alternative methods are taken from Dornisch et al. [50].	58
3.20 Combination of NURBS basis orders and Lagrange basis orders.	59
3.21 A schematic of the mixed grid expression of the shell geometry and its nodes.	60
3.22 The Serendipity and Lagrange nodes in an element in the parametrical space $[-1, 1]^2$	60
3.23 The quadratic and cubic polynomial terms in Lagrange and Serendipity basis.	61
3.24 The shell obstacle course results from the NURBS/Lagrange formulation. First row: Scordelis-Lo roof problem. Second row: Pinched cylinder problem. Third row: Hemisphere problem. Left column: The “same order” formulations. Right column: The “lower order” formulations. The abbreviations “N”, “L”, “C” denote the order of NURBS basis, the order of Lagrange basis and the NURBS regularity respectively.	63
3.25 The shell obstacle results from the NURBS/Serendipity formulations. First row: Scordelis-Lo roof problem. Second row: Pinched cylinder problem. Third row: Hemisphere problem. Left column: The “Same order” formulations. Right column: The “Lower order” formulations. The abbreviations “N”, “S”, “C” denote the order of NURBS basis, the order of Serendipity basis and the NURBS regularity respectively.	64
3.26 The simply supported square plate problem setup.	65
3.27 The square plate problem results from the NURBS/Lagrange formulation. Left column: The “Same order” formulations. Right column: The “Lower order” formulations. The abbreviations “N”, “L”, “C” denote the order of NURBS basis, the order of Lagrange basis and the NURBS regularity respectively. The number 10^3 and 10^5 refer to the plate slenderness.	66
3.28 The square plate problem results from the NURBS/Serendipity formulation. Left column: The “Same order” formulations. Right column: The “Lower order” formulations. The abbreviations “N”, “S”, “C” denote the order of NURBS basis, the order of Serendipity basis and the NURBS regularity respectively. The note “L1” is identical with “S1”. The number 10^3 and 10^5 refer to the plate slenderness.	67

LIST OF FIGURES

3.29	The cubic NURBS basis functions within a patch with different regularities.	69
3.30	A schematic about total stiffness matrix assembly procedure with different inter-element regularities for cubic element in IGA.	70
3.31	A schematic of the proposed modified reduced quadrature rule with 13 elements in a patch.	71
3.32	The results from Scordelis-Lo roof problem with the Kirchhoff-Love shell, integrated by the full quadrature and the modified reduced quadrature schemes.	72
3.33	The square plate problem results from the NURBS/Serendipity formulations with modified reduced quadrature scheme. Left column: The “Same order” formulations. Right column: The “Lower order” formulations. The abbreviations “N”, “S”, “C” denote the order of NURBS basis, the order of Serendipity basis and the NURBS regularity respectively. The number 10^3 and 10^5 refer to the plate slenderness.	73
3.34	The shell obstacle results from the NURBS/Serendipity formulations with modified reduced quadrature scheme. First row: Scordelis-lo roof problem. Second row: Pinched cylinder problem. Third row: Hemisphere problem. Left column: The “same order” formulations. Right column: The “lower order” formulations. The abbreviations “N”, “S”, “C” denote the order of NURBS basis, the order of Serendipity basis and the NURBS regularity respectively.	74
4.1	Four connected patches’ layout (b) and the record in a matrix (a).	80
4.2	Four connected patches with various types of meshes.	80
4.3	Two C^0 connected patches and their virtual mutual insertion.	81
4.4	Two G^1 connected patches and their virtual mutual insertion.	83
4.5	The cantilever beam problem setup. Beam length $L = 10$ and height $h = 2$.	86
4.6	The non-matching mesh of the cantilever beam.	87
4.7	Cantilever problem results: The shear stress results along $x = 5$ from different methods with matching meshes and hierarchical meshes. “M”, “H” indicate matching meshes and hierarchical meshes respectively. “Stc”, “P1” and “P2” indicate static condensation method, penalty method with the penalty coefficient 10^7 and 10^{16}	87
4.8	Cantilever problem results: The shear stress results along $x = 5$ from non-matching meshes. “NM” indicates non-matching meshes. Other notations are the same with these in figure 4.7.	87
4.9	Cantilever problem results: u_x differences along the common boundary from different mesh cases and continuity enforcement methods. The meanings of notations are the same with those shown in this example.	88

4.10	Scordelis-Lo roof problem setup. It also shows a case of hierarchical meshes.	89
4.11	Scordelis-Lo roof problem: u_z at point C varies with h refinements. “M”, “H” and “NM” indicate matching, hierarchical and non-matching meshes. “Stc” indicates static condensation method. “P1” indicates penalty method with the penalty coefficient 10^{10} and “P2” with 10^{16} . “Strip” denotes results from bending strip method [87].	90
4.12	Scordelis-Lo roof problem: u_z at point C varies with h refinements. “NM” indicates non-matching meshes. Other notations’ meanings are the same with those in figure 4.11.	91
4.13	Pinched cylinder problem setup. It also shows a hierarchical meshes case.	91
4.14	Pinched cylinder problem: u_z at point B varies with h refinement. “P1” and “P2” indicate penalty method with penalty coefficients 10^9 and 10^{14} . Other notations’ meanings are the same with these in the former example.	92
4.15	Pinched cylinder problem: u_z at point B varies with h refinement.	92
4.16	Pinched cylinder problem: u_z contour plots (only upper part) from non-matching meshes ($N = 10$). Results from static condensation method (a) and penalty method with various penalty coefficients: (b) 10^6 , (c) 10^{16} , (d) 10^9 .	93
4.17	A full structure with two substructures and their nodes.	96
4.18	A schematic about the substructure modes.	97
4.19	The shell substructure and interface control points (a), the bending strip for the substructures coupling (b).	98
4.20	L-shape shell problem setup, the elements (a) and the control points (b).	99
4.21	L-shape shell, the natural frequencies obtained from the modal synthesis and the full structure analysis.	100
4.22	L-shape shell, the relative errors between the full structure analysis and the modal synthesis with different number of fixed interface modes: (a)20, (b)25, (c)35, (d)40.	100
4.23	L-shape shell, some modal shapes from the full structure analysis ($a \sim c$) and the modal synthesis ($d \sim f$).	101
4.24	The curved shell problem setup, the material properties (a) and the meshes (b).	101
4.25	The curved shell, the natural frequencies obtained from the modal synthesis and the full structure analysis	102
4.26	The curved shell, the relative errors between the full structure analysis and the modal synthesis with different number of fixed interface modes: (a)10, (b)15, (c)20, and (d)25.	102
4.27	The curved shell, the first three modal shapes from the full structure analysis ($a \sim c$) and the modal synthesis ($d \sim f$).	103

LIST OF FIGURES

4.28	The structure mesh and the excitation.	104
4.29	The response amplitude $ u_z $ at control point M from the modal synthesis and full structure analysis	104
4.30	The response amplitude $ u_z $ error between the full structure analysis and the modal synthesis with different number of fixed interface modes: (a) 10, (b) 15, (c) 20 and (d) 25.	105
4.31	The response amplitude $ u_z $ obtained from the modal synthesis at fre- quencies 0.4 (a) and 0.4338 (b) and their relative errors with full structure analysis (c) (d)	106
5.1	Initial structure setup and design parameters.	111
5.2	The fine meshed analysis model.	111
5.3	The objective function sensitivity w.r.t analysis model movable control point z coordinates.	114
5.4	Coarse mesh model sensitivity.	115
5.5	Design variables sensitivity.	116
5.6	Example 1, the optimum shape obtained.	117
5.7	Example 1, the optimization iteration history.	117
5.8	Example 2, the geometric model and the substructures.	118
5.9	Example 2, the design part and the design variables.	118
5.10	Example 2, the analysis model and the problem setup.	119
5.11	Example 2, The optimization history of the objective function.	120
5.12	Example 2, The optimization history of the compliance constraint.	120
5.13	Example 2, The optimization history of the mass constraint.	120
5.14	Example 2, the optimum structure shape.	121

List of Tables

2.1	Comparison of finite element analysis and isogeometric analysis based on NURBS, table reproduced from [37].	36
3.1	The Various formulations' element level DOFs.	62
4.1	The stress results at point A obtained from static condensation method with non-matching meshes. "Elem Num" indicates the number of elements on Ω_1 's η direction. "Num-1" and "Num-2" denote the number of basis functions on the common edge in Ω_1 and Ω_2 respectively. "Num-e" indicates the number of effective basis functions, it is the dimension of the space $Null(\mathbf{L})$, \mathbf{L} refers to equation (4.14).	89
4.2	The number of degrees of freedom and time costs in the harmonic response analysis. The "time" denotes the total time used for solving the structure equation in all sample points. The "modes" denote the "fixed interface modes".	105
5.1	Design sensitivities obtained from the full FDM method, full analytical method ($Analytical_1$) and FDM-analytical method ($Analytical_2$).	116
5.2	Example 1, The initial and optimum design variable values and the structural response.	117
5.3	Example 2, the initial and optimum design variable values and the structural response.	121

LIST OF TABLES

List of Abbreviations

- FEM: Finite element method
- IGA: Isogeometric analysis
- CAD: Computer aided design
- CAGD: Computer aided geometric design
- CAE: Computer aided engineering
- PDE: Partial differential equation
- NURBS: Non uniform rational B-spline
- PHT: Spline on hierarchical T-mesh
- THB: Truncated Hierarchical B-spline
- LRB: Local refined B-spline
- IGES: Initial graphics exchange specification
- DOF: Degree of freedom
- KL: Kirchhoff-Love shell
- RM: Reissner-Mindlin shell
- FDM: Finite difference method
- SQP: Sequential quadratic programming
- SLP: Sequential linear programming
- EA: Evolutionary algorithms

Chapter 1

Introduction

1.1 Background

1.1.1 Shell structure

Shell structure is a continua with one dimension being significantly smaller than the other two. It is a frequently used material form in various industrial applications, e.g. automotive, aircraft, due to its high load bearing capacity per weight. The thin thickness of the structure can reduce the dead load and thus save the material. The effect of curvature can be utilized to carry the transverse loading in an optimal way. This type of structure was used long time before people really understood it, like the Roman Pantheon (1.1) which was built in the year about AD 125 and the Anji bridge (1.2) built in the year about AD 600.



Figure 1.1: The Roman Pantheon, Italy.



Figure 1.2: The Anji bridge, China.

It was not until 18th century that researchers began to investigate the shell structures from the mathematical aspect systematically. The initiatory developments of shell models started from observations and heuristic hypothesis. The curved beam, the plate and the shell, they share some characteristics, their progresses interacted with each other. Generations of researchers' efforts gave birth to the EulerBernoulli beam theory [125],

1. INTRODUCTION

the Timoshenko beam theory [125], the Kirchhoff-Love plate/shell theory [4, 45] and the Reissner-Mindlin plate/shell theory [51, 108]. They constitute the traditional thin wall structure theories. The famous hypothesis are the Kirchhoff-Love assumption and the Reissner-Mindlin assumption, which are still widely used today. The former takes account of the shear deformation while the latter does not. It is worth mentioning that the developments of those models beyond the path of continuum theory, although they are subcategories of the latter. The different models give their own structural control equations. And those equations are normally more complicated than that of the three dimensional solid mechanics, e.g. the Euler-Bernoulli beam control equation is a partial differential equation of order four while the solid model equation is only of order two. It is a conflict with the common sense one might have that the problem will become easier when its dimension reduces.

Besides the traditional way of shell model development, some other ways like the geometrical exact shell [123] and the degenerated solid shell [5, 6] are developed from other start points. The geometrical exact shell starts from an exact kinematics description of a two dimensional Cosserat surface [95]. The degenerated solid shell model adopts another idea that applying the shell assumptions after the finite element discretization. Other latest shell models are solid shell [71], which from our point of view is a solid element, and Seven-Parameters shell model [90], which takes account of the shell thickness change. They both allow the use of three dimensional material law. The complexity of the model are also reduced.

Another dimension of the shell research is the solution of the shell control equation. Finite element method (FEM) is the dominant method in the field of solid mechanics. It is a method for solving the partial differential equations (PDE). It is based on the unknown parameter fields approximation in a proper functional space. The approximation with the compact support basis functions gives birth to the element concept, which is also intuitively understandable from the structure physical discretization point of view. There is a close relation between the shell models and their FEM implementations. Some times it might be difficult to distinguish them clearly, which is the case in the degenerated solid shell. It is the requirement of FEM implementation that makes the Reissner-Mindlin shell more popular than the Kirchhoff-Love shell, although from the application point of view the latter is already enough in most cases. A common difficulty that a lot of shell models suffer when using FEM is the numerical locking [32]. Various locking phenomena exist, such as the membrane locking, the shear locking and curvature thickness locking (trapezoidal locking). The superficial reason is the ill-conditioning of the linear structural equation, while the deeper one is the incompatibility of the functional spaces. The spurious energy induced by the functional space incompatibility makes the structure stiffer than it really is. Some great ideas are proposed to relieve this problem, such as reduced integration [140], assumed strain methods [94], B-bar methods [78], enhanced assumed

strain (EAS) method [124].

An overview about shell structure is presented here. Due to the complexity and the variety of this topic, it is definitely not enough for covering all the aspects of the research. One is encouraged to obtain a thorough knowledge by reading the book [23].

1.1.2 Isogeometric analysis

The finite element method is the dominant method in solid mechanics. It was firstly developed by the engineering society in 1950s and then investigated and improved by the academic society. The idea of finite element method is the function approximation. The basis functions used are usually Lagrange polynomials, Hermite polynomials, and Serendipity polynomials. They were all developed nearly half a century ago and are still being widely used in our present commercial FEM software. The isoparametric elements concepts emerged in the late 1960s, most of the elements nowadays are still of this type. The isoparametric element utilizes the same map for both the geometry and the unknown field. Limited by the basis functions, the FEM model will be a faceted approximation of the physical model, the approximation exactness improves with an increase in the mesh density, shown in figure 1.3.

The physical model is normally modelled by the computer aided geometric design (CAGD) technologies nowadays. Its notable development originated from the pioneer work of two excellent French automotive engineers, Pierre Bezier of Renault and Paul de Faget de Casteljau of Citroen. They developed the Bezier curve and surface in the early 1960s. Before that time, the design tools were aboriginal. Engineers used flexible metal strip to design a curve which passed some given measured points. The curve did not have a mathematical description, precise control is thus impossible. The B-spline and the Non uniform rational B-spline (NURBS) emerged later in the Ph.D thesis of Riesenfeld [110] and Versprille [132]. With the help of many efficient and stable manipulation algorithms, such as Coxde Boor recursion [40, 46], the de Boor algorithm [47], the Oslo algorithm [35], NURBS found its dominant position in 1980s. In the year 1983, NURBS based geometric description became the Initial Graphics Exchange Specification (IGES) standard [111].

The development of CAD and CAE were on their own path without interaction. The CAE technology was developed earlier than the CAD. The CAE was pretty matured in the 1970s when CAD was still on fast developing. This made the two systems use different mathematical tools to describe the geometry. A model from the CAD system should be changed into the FEM model to implement the analysis, while this exchange is neither exact nor reversible, it also takes a lot of time to finish this procedure. Things are much more severe than the inconvenience, the inexactness of geometry also leads to large errors in some analysis which are sensible to geometric imperfection, such as the shell buckling [127] and the boundary layer phenomena [13]. Hughes et al. [79] proposed the

1. INTRODUCTION

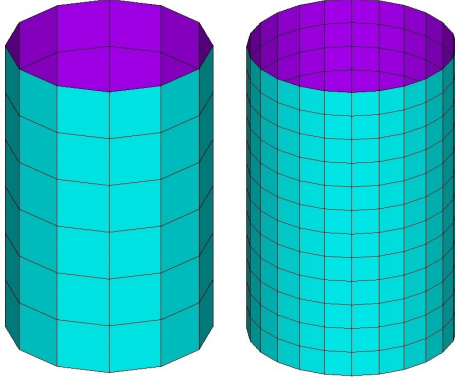


Figure 1.3: The FEM meshes of a cylindrical shell with different mesh densities.

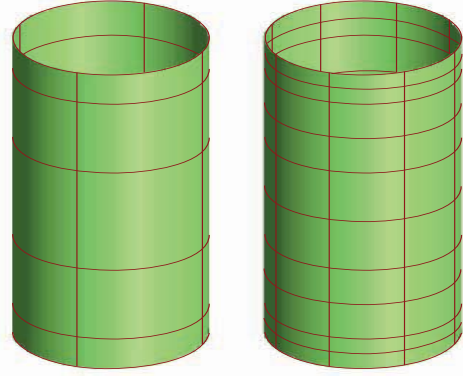


Figure 1.4: The IGA meshes of a cylindrical shell with different mesh densities [79].

isogeometric method in 2005 that can analyse the model without changing the geometry. It cast light on integrating the CAD and CAE. This method was further developed by Bazilevs et al. [14] and Cottrell et al. [38]. The analysis model is as exact as the geometric model in this method. Figure (1.4) shows the analysis model in IGA, it is geometrically exact regardless of the mesh density.

IGA is promising in bridging the gap between CAD and CAE. Besides the NURBS or B-spline based IGA, the basis functions which are commonly used in CAGD also find their application in IGA, such as T-spline [17] and PHT spline (Spline on Hierarchy T-mesh) [98, 136]. The development of IGA also motivates the research in CAGD, some local refinable spline are developed aiming at compensating the drawbacks of NURBS based IGA, such as Hierarchical B-spline (HB) [133], Truncate Hierarchical B-spline (THB) [62] and Local refined B-spline (LRB) [48]. The terminology isogeometric analysis refers to a series of methods which possess the same basis functions in the approximation of both the analysis domain and the unknown fields in this domain.

IGA method has been successfully used in various problems where traditional FEM were used, such as electromagnetic [29], contact [92], fluid [65] and fluid-structure coupling problems [15] and has shown superior performance compared to the traditional finite elements method. Commonly, whereas the FEM is used, IGA can also be used, their essential difference only lies within the basis functions used. This is a great advantage, since less modifications will be required in the existing code to obtain a IGA analysis. A general knowledge about the isogeometric analysis can be found in book [37].

1.1.3 Structural optimization

Structural optimization means finding the optimum material layout of a structure to bear the loads and give acceptable or specific responses according to the designers' intention. Its development greatly relies on the computer science, since both the analysis of the

structures and the solving of the optimization problem need a lot of calculation effort and usually can not be handled without the help of computer. With the computer developments since the 1980s, the structural optimization advanced more and more feasible and finally become a indispensable step in the design circle today [114].

A general structural optimization problem can be formulated as

$$\begin{aligned} & \text{minimize} && f(x, s(x)) \\ & \text{subject to,} && g(x, s(x)) \leq 0 \\ & && h(x, s(x)) = 0 \end{aligned} \tag{1.1}$$

The f indicates the objective function, $s(x)$ is named the state variable, x is the design variable. An indispensable equilibrium constraint is the structural control equation. The constraints as well as the objective function are also called cost functions, they might exchange with each other depending on the user's intention. The state variable in structural optimization normally is the displacement. In the context of structural optimization, x represents some features of the structure. Depending on the features, the structural optimization problem can be divided into three categories, the sizing optimization, the shape optimization and the topology optimization, depicted in figure 1.5.

- *Sizing optimization:* This is when x indicates the thickness of a plate, the section parameters of a beam, the height, length or the depth of a structure, the material property of the structure, etc. The variables defined on the beam section in figure 1.5 are sizing design variables.
- *Shape optimization:* The design variable is the curve in a region or the surface of a volume, x is a function in such case. The bottom curve in figure 1.5 is a shape design variable. For shape design problem, a shape parametrization is normally required to transform this continuum design problem to discrete design problem.
- *Topology optimization:* This is the most general structural optimization case. Neither the geometry nor the topology of the structure is predefined. Only a rough design region, a two or three dimensional space, as well as the boundary condition/loads is given. The optimizer tries to fix the optimum material distribution within this space.

The particularity the structural optimization has over the common mathematical optimization is its physical background. It is constrained by a PDE which is the structural control equation. As a result, the basic concepts, such as convex programming, quadratic/linear programming, and the optimization algorithms, such as sequential quadratic programming (SQP), sequential linear programming (SLP), various evolutionary algorithms (EA) which are studied in general mathematical problems could be also used in structural optimization. However, the structural optimization research focus more on the

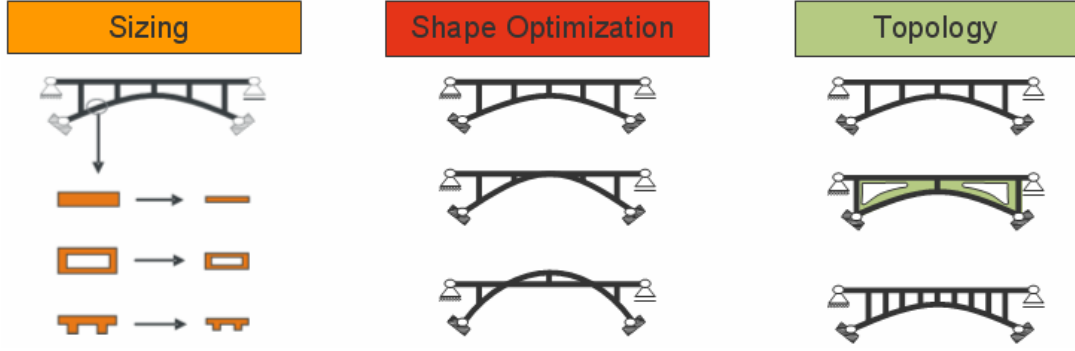


Figure 1.5: Different types of structural optimization problems, picture from [1].

formulation of the problem, i.e. how to translate the design requirements to a mathematical programming, such as, the choose of design variables, the formulation of cost functions. This is far more complicated than one might think. In shape and topology optimization, a lot of efforts are spent on this part, a thorough investigation could be found in [30, 112]. Another emphasis is on the sensitivity analysis, unlike the pure mathematical optimization, the evaluation of the PDE sensitivity in structural optimization is not a easy thing, however is in urgent need in massive design variables case, e.g. topology optimization. One is suggested to read the book [34]. Another research is the surrogate model based optimization [61, 107]. It is due to the fact that the structural analysis is often time costing, it is more time saving to construct a surrogate model to approximate the structural control equation.

Structural optimization, an traditional research topic and widely used design tool in industry, is still in developing. Only a short introduction to this topic is given here, one is encouraged to read the paper listed to have a deeper understanding. The research focus in the thesis is the shape optimization, however it is advantageous to better understand the heritage of the predecessors and base the innovation on their foundation.

1.2 Motivation

IGA method is promising in bridging the gap between the CAD and the CAE. It brings a potential power in the structure optimization and the geometrical parameter study. The motivations of the subject are listed as following:

- *Isogeometric shell element development*: Develop new shell elements under the IGA framework suitable for industrial application.
- *Structural dynamics analysis with IGA shell elements*: Combine the IGA and the traditional structural dynamics analysis framework to improve the efficiency, meanwhile, enjoy the advantages the IGA provides.

- *Shell shape optimization with dynamic criteria*: Develop IGA based shape optimization framework for fast free form surface design with massive design variables, the dynamic criteria are considered.

The exact geometrical map in IGA provides an explicit link between the parametric domain and the physical domain. The analytical parameter sensitivity can thus be obtained, which is of great importance for an efficient large scale optimization. Another advantage that IGA based optimization brings is the manufacturability of the optimum structure, since the optimum shape will be a CAD model rather than a facets expressed geometry.

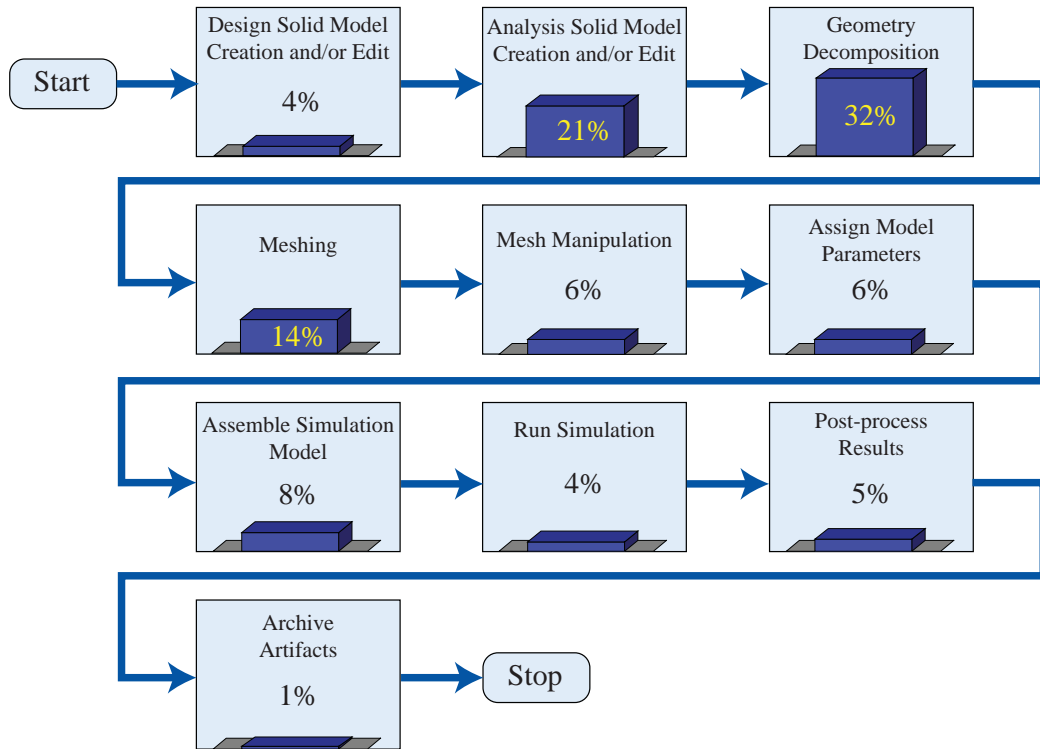


Figure 1.6: Estimation of the relative time costs of each step in the engineering design circle, picture from [37]

The IGA refinement does not destroy the map between the geometry and the mesh. Tracing back to the CAD model is no longer needed. In engineering structural optimization, model reanalysis is an indispensable step. Its efficiency greatly affects the overall efficiency. In the traditional FEM based optimization framework, the fixing of CAD model and creating FEM model account for 80% of overall analysis time cost [37], see figure (1.6). With IGA analysis, large saving can be expected in this part. This is a huge advantage, where massive mesh refinements and adjustments are needed during the iterations. As for the local parameter study or optimization concerning dynamics, where the concerned parameters only relate to several substructures, it is more computational economical to

1. INTRODUCTION

only remesh the corresponding substructures. In such a case, the modal synthesis method will also be needed. This is our motivation to develop the modal synthesis method with IGA shell elements.

The high efficiency, the exact and efficient sensitivity analysis, the manufacturability of the optimum shape, they constitute the main reasons to choose IGA based optimization. In order to conduct efficient local parameters optimization considering dynamics criteria, the modal synthesis method is also needed.

1.3 Outline

The thesis is composed of six chapters, the organization as well as the overall content is described as following:

In the first chapter, we introduced the research background and the motivation. The ultimate aim of the work is to develop a fast shape optimization framework based on isogeometric shell elements. To address this goal, the IGA shell analysis should also be investigated. Meanwhile, the concern of the thesis is the structural dynamics problem, the traditional modal synthesis method is thus studied. In order to achieve a fast and flexible optimization, gradient based optimization method is indispensable, thence the analytical design sensitivity should also be studied. In this chapter, a broad background of the related topics is presented.

We will introduce the foundation of IGA shell analysis in the second chapter. Namely, the shell models and the IGA background (Computer Aided Geometry Design). The shell formulations possess two parts, the shell models and the IGA implementation. We will emphasize on the Kirchhoff-Love model and Reissner-Mindlin model. The deductions from the three dimensional continuum to the shell models are detailed. As for the IGA background, the frequently used CAGD methods are presented. It is a short review about the B-spline, the NURBS, and its related operations. In the end of this chapter, the general IGA analysis framework is presented, as well as its characteristics compared to the traditional FEM method.

The IGA implementation of the pre-introduced shell models are detailed in the third chapter. The linear IGA Kirchhoff-Love shell and the Reissner-Minlin shell implementations are presented here. A series of IGA Reissner-Minlin shell is proposed, namely mixed grid IGA shell. It is under the IGA framework, meanwhile it also adopts the interpolatory Lagrange/Senrendipity basis, which are frequently used in the traditional FEM. A modified reduce quadrature scheme aiming at improving the efficiency in the proposed IGA shell is also presented in this chapter, it can not only improve the efficiency but also relieve the locking phenomenon without introducing the “hourglass” mode.

The engineering structures are normally modelled with multiple patches, patches coupling is needed to analyse such structures. Meanwhile, our focus is on the structural

dynamics analysis. Hence, in the fourth chapter, we will introduce the multiple patch coupling in IGA analysis as well as the modal synthesis method. The tradition modal synthesis method is incorporated into the IGA frame to improve the efficiency of the analysis concerning structural dynamics aspect. It also lays a foundation for the structural optimization with local design variables in the next chapter.

A fast IGA based shell shape optimization framework is presented in the fifth chapter. For massive design variables optimization problem, the sensitivity information is useful to speed up the optimization. The focus in this chapter is thus on the analytical design sensitivities analysis. A sensitivity mapping method is proposed to allow a flexible design variables definition as well as an exact sensitivity evaluation. The element-level discrete analytical sensitivity with respect to the intrinsic shape parameters is firstly calculated, from which the design sensitivity is then extracted with the help of a sensitivity map. The modal synthesis method is also used to avoid a repeated evaluation of some substructures where there are no design variables defined. This framework is efficient and flexible for large scale optimization problem. The IGA method naturally gives CAD expressed optimum model, which is manufacturable. Results show the effectiveness of the method.

A conclusion of the thesis will be given in the sixth chapter.

1. INTRODUCTION

Chapter 2

Basics on shell models and computer aided geometry design

A standard design procedure begins with the modelling of objects in computer aided design software. With the isogeometric method, the design model could be seamlessly transferred to analysis model, this procedure is also reversible. As a result, the obtained optimum model will be a design model. Hence, we adopt isogeometric shell elements to model the design surface with shell properties, we will introduce in this chapter the basics about isogeometric shell formulations.

Isogeometric shell formulation consists of two parts, the shell models and the IGA implementation. In this chapter, we emphasize on the Kirchhoff-Love shell model and Reissner-Minlin shell model. The three dimensional solid mechanics is a general theory that controls the structural response of any material form. Shell structure, as a special form of continua, should also obey this rule. However, its control equation is definitely different with the three dimensional solids. This disparity is due to the imposing of shell assumptions. How to accomplish this transformation is detailed in the first part of the chapter.

IGA shell formulation is a result that applying the IGA method to the solving of the shell control equation. Compared with the traditional FEM, the innovation of IGA is the use of basis functions, which are commonly used in computer aided design, to approximate the unknown fields. Thus, the knowledge of CAGD is needed to well understand it, which constitutes the second part of the chapter.

IGA method succeeds the main analysis framework from the traditional FEM, while it also incorporates some tools from CAGD. Some characteristics of the IGA are thus generated. Meanwhile, the concepts and terminologies in FEM are given new meanings. Those will be introduced in the third part of this chapter.

2.1 Shell models deduction

Shell structure is a special continua, one of whose dimensions is far more smaller than the other two. The three dimensional structure control equation can thus be expressed by the parameters which only relate to the middle surface. There are many methods to achieve such reduction, here we briefly state the one that derived directly from the three dimensional continuum and the degenerated solid method. As for the shell models, there are a large number of shell models, e.g. Reissner-Minlin shell, Kirchhoff-Love shell, solid shell. Some times they are also named with the degrees of freedom in an element, e.g. 5 or 7 degrees of freedom Reissner-Mindlin shell. Other times, they appear in companion with the locking relief strategies. It is a traditional research topic which attracted a lot of brilliant scholars in twentieth century, a large number of literatures were published. Even trying to cover part of this topic needs a lot of effort. One is suggested to read the book [23] to well understand it. In the present thesis, we emphasize on the linear small deformation Kirchhoff-Love shell model and the Reissner-Mindlin shell model. In the following sections, we try to give a systematic introduction about those two models.

2.1.1 Differential geometry

The shell like body is noted as \mathbf{X} , shown in figure 2.1. It is parametrized with three parameters θ^1 , θ^2 and θ^3 . There should exist a middle surface of the shell body, it only relates to two parameters. Those are the conventions and the start points of the deduction.

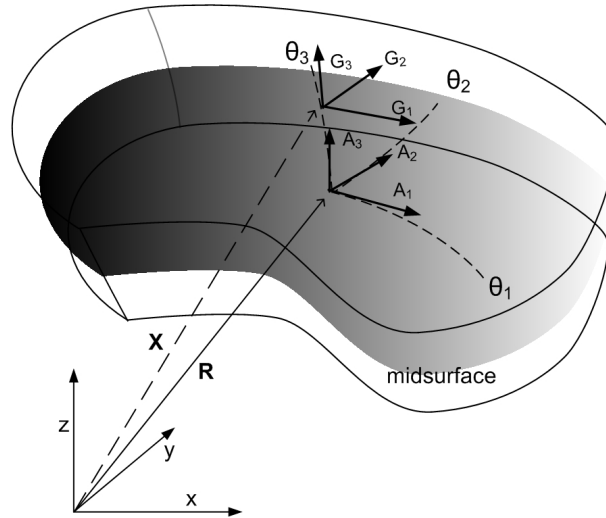


Figure 2.1: The geometry of the shell body

The shell middle surface is notes as

$$\mathbf{R}^0(\theta^1, \theta^2) = \mathbf{X}(\theta^1, \theta^2, \theta^3)|_{\theta^3=0}. \quad (2.1)$$

There exists a curvilinear coordinate system at each point in the shell body. The covariant base vectors at the points in the shell body and on the surface can be expressed respectively as

$$\mathbf{G}_i = \mathbf{X}_{,i}, \quad \mathbf{A}_i = \mathbf{R}_{,i}^0. \quad (2.2)$$

Here, $()_i$ indicates $\partial()/\theta^i$, $i \in \{1, 2, 3\}$. Hereinafter, without specific statement, we adopt all the conventions in the tensor analysis. \mathbf{G}_i is the curvilinear axis of a coordinate system in the shell body, \mathbf{A}_i is the curvilinear axis of the coordinate system on the shell surface. Their metric tensors are

$$\begin{aligned} \mathbf{G} &= G_{ij} \mathbf{G}^i \otimes \mathbf{G}^j = G^{ij} \mathbf{G}_i \otimes \mathbf{G}_j \\ \mathbf{A} &= A_{ij} \mathbf{A}^i \otimes \mathbf{A}^j = A^{ij} \mathbf{A}_i \otimes \mathbf{A}_j \end{aligned} \quad (2.3)$$

Here,

$$\begin{aligned} G_{ij} &= \mathbf{G}_i \cdot \mathbf{G}_j, \quad A_{ij} = \mathbf{A}_i \cdot \mathbf{A}_j \\ G^{ij} &= \mathbf{G}^i \cdot \mathbf{G}^j, \quad A^{ij} = \mathbf{A}^i \cdot \mathbf{A}^j \end{aligned} \quad (2.4)$$

The \mathbf{G}^i and \mathbf{A}^i refer to the contravariant base vectors of the coordinates in the shell body and on the shell surface respectively. Their relationships with the covariant basis are

$$\mathbf{G}_i \cdot \mathbf{G}^j = \delta_{ij}, \quad \mathbf{A}_i \cdot \mathbf{A}^j = \delta_{ij}. \quad (2.5)$$

Here, δ_{ij} indicates the Kronecker delta, which is a function gives 1 if $i = j$ and 0 otherwise.

The second fundamental form of the shell middle surface is defined as

$$\mathbf{B}_{\alpha\beta} = \frac{1}{2}(\mathbf{A}_\alpha \cdot \mathbf{A}_{3,\beta} + \mathbf{A}_\beta \cdot \mathbf{A}_{3,\alpha}). \quad (2.6)$$

2.1.2 Continuum mechanics

The shell body is expressed as a set \mathfrak{B} , it is composed of connected material points \mathfrak{M}_i . The boundary of the body is denoted as $\partial\mathfrak{B}$. The spatial positions of the body points constitute another set named the configuration, expressed as

$$\chi := (\mathfrak{B}, t) \rightarrow \mathfrak{S}.$$

The member in the set \mathfrak{S} is noted as \mathbf{x} , $\mathbf{x} \in \mathbb{R}^3$, it is the image of the material point \mathfrak{M}_i . The reference configuration is the body at time $t = 0$, its image is \mathbf{X} . It denotes the undeformed structure. A deformation process is shown in figure 2.2, it is a evolution of

the configuration with time noted as

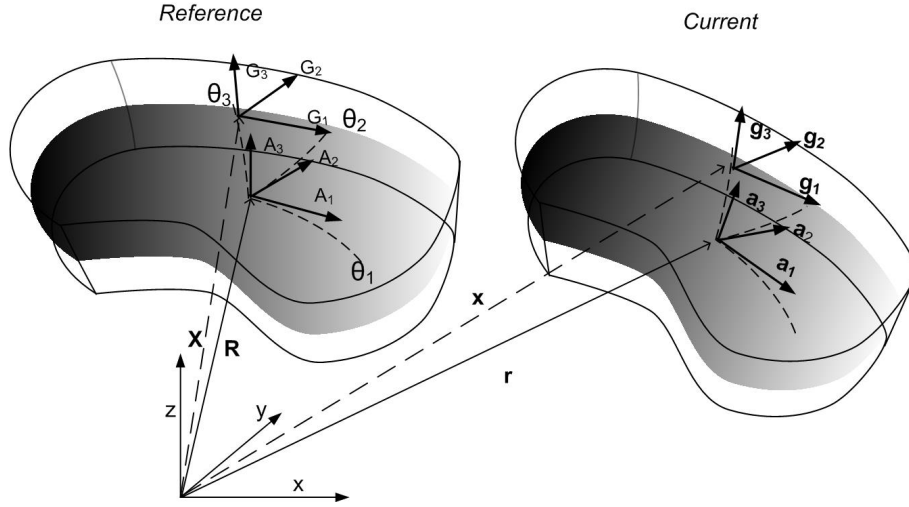


Figure 2.2: The deformation process of the shell body

$$\Phi := (\mathbf{X}, t) \rightarrow \mathbb{R}^3.$$

The current configuration, which denotes the deformed structure, can thus be noted as a function of the initial configuration as

$$\mathbf{x} = \Phi(\mathbf{X}, t). \quad (2.7)$$

The displacement of the structure is

$$\mathbf{u}(\mathbf{X}, t) = \mathbf{x}(\mathbf{X}, t) - \mathbf{X}. \quad (2.8)$$

The material deformation gradient is

$$\begin{aligned} \mathbf{F} &= \nabla \mathbf{x} = \mathbf{g}_k \otimes \mathbf{G}^k \\ &= \nabla(\mathbf{u} + \mathbf{X}) = \nabla \mathbf{u} + \mathbf{G}. \end{aligned} \quad (2.9)$$

Here, \mathbf{g}_k refer to the covariant base vectors of the deformed configuration. Hereinafter, all the lower case terms in section 2.1.1 indicate terms relate to the deformed configuration.

The Green-Lagrange tensor, which is a strain measurement for large deformation, is obtained as following

$$\begin{aligned} \mathbf{E} &= \frac{1}{2} (\mathbf{F}^T \cdot \mathbf{F} - \mathbf{G}) = E_{ij} \mathbf{G}^i \otimes \mathbf{G}^j \\ &= \frac{1}{2} (\nabla \mathbf{u} + \nabla \mathbf{u}^T + \nabla \mathbf{u}^T \cdot \nabla \mathbf{u}) \end{aligned} \quad (2.10)$$

$$E_{ij} = \frac{1}{2} (g_{ij} - G_{ij}). \quad (2.11)$$

Its energetically conjugated stress measurement is the second PiolaKirchhoff stress tensor \mathbf{S} . It refers to the reference configuration, so it does not directly reflect the stress state of the deformed structure. Assuming the strain energy density exists and is noted as \mathbf{W}^{int} , its relationship with strain and stress will be

$$\mathbf{W}^{int} = \frac{1}{2} \mathbf{S} : \mathbf{E}. \quad (2.12)$$

The scope of the present research is confined to the small deformation case. In this case, the reference configuration and the current configuration are approximately the same. The seconde order item of the GreenLagrange tensor in equation (2.10) with respect to \mathbf{u} is omitted. Hence, the above mentioned strain and stress measurements are simplified as linear strain tensor \mathbf{E}^L and stress tensor \mathbf{S}^L . The expressions are

$$\begin{aligned} \mathbf{E}^L &= E_{ij}^L \mathbf{G}^i \otimes \mathbf{G}^j \\ &= \frac{1}{2} (\nabla \mathbf{u} + \nabla \mathbf{u}^T) \end{aligned} \quad (2.13)$$

$$\begin{aligned} E_{ij}^L &= \frac{1}{2} (\mathbf{u}_{,i} \cdot \mathbf{G}_j + \mathbf{u}_{,j} \cdot \mathbf{G}_i) \\ &= \frac{1}{2} (\mathbf{g}_i \cdot \mathbf{G}_j + \mathbf{g}_j \cdot \mathbf{G}_i) - G_{ij}. \end{aligned} \quad (2.14)$$

The linear Saint-Venant Kirchhoff material law is used in the present research, it gives the following relation between the stress and linear strain tensor,

$$\mathbf{S} = \mathbf{C} : \mathbf{E}. \quad (2.15)$$

We only deal with isotropic material in the present work. In such a case, the material tensor components merely rely on two parameters. In engineering society, Youngs modulus E and Poissons ratio ν are normally used. The material tensor components are

$$\begin{aligned} \mathbf{C} &= C^{ijkl} \mathbf{G}_i \otimes \mathbf{G}_j \otimes \mathbf{G}_k \otimes \mathbf{G}_l \\ C^{ijkl} &= \lambda G^{ij} G^{kl} + \mu (G^{ik} G^{jl} + G^{il} G^{jk}). \end{aligned} \quad (2.16)$$

Here, λ and μ are called Lamé constants. They are expressed as

$$\lambda = \frac{\nu E}{(1 + \nu)(1 - 2\nu)}, \quad \mu = \frac{E}{2(1 + \nu)}. \quad (2.17)$$

Together with the equations (2.13) and (2.15), the control equation in PDE form for the solid body mechanics is as following,

$$\nabla \cdot (\mathbf{F} \cdot \mathbf{S}) + \rho \mathbf{b} = \mathbf{0} \quad (2.18)$$

$$\mathbf{u} = \hat{\mathbf{u}}, \text{ on } \Gamma_u \quad (2.19)$$

$$\mathbf{F} \cdot \mathbf{S} \cdot \mathbf{n} = \hat{\mathbf{t}}, \text{ on } \Gamma_\sigma. \quad (2.20)$$

Here, equation (2.18) is the equilibrium equation, equation (2.19) and (2.20) denote the Dirichlet boundary condition and the Neumann boundary condition respectively. \mathbf{u} denotes the displacement field, $\hat{\mathbf{u}}$ denotes the prescribed displacement on boundary Γ_u , $\hat{\mathbf{t}}$ is the prescribed force on the boundary Γ_σ , \mathbf{n} is the outward normal vector on the boundary, $\Gamma_u + \Gamma_\sigma = \partial\mathfrak{B}$.

According to the virtual work principle, or with the help of mathematical tools like weighted residual approach, the variational or weak form of the above PDE can be obtained as

$$\delta\Pi = \int_{\Omega} (\mathbf{S} : \delta\mathbf{E} - \rho \mathbf{b} \cdot \delta\mathbf{u}) d\Omega - \int_{\Gamma_\sigma} \mathbf{t} \cdot \delta\mathbf{u} d\Omega = \mathbf{0}. \quad (2.21)$$

$$\underbrace{\int_{\Omega} \mathbf{S} : \delta\mathbf{E} d\Omega}_{\delta\Pi_{int}} = \underbrace{\int_{\Omega} \rho \mathbf{b} \cdot \delta\mathbf{u} d\Omega + \int_{\Gamma_\sigma} \mathbf{t} \cdot \delta\mathbf{u} d\Omega}_{\delta\Pi_{ext}} \quad (2.22)$$

Here, $\delta\Pi_{int}$ and $\delta\Pi_{ext}$ denote the inner force virtual work and external force virtual work respectively. The integral equation 2.21 or 2.22 is the start point of FEM method.

2.1.3 Kirchhoff-Love shell model

The Kirchhoff-Love shell model can be obtained after imposing the Kirchhoff-Love assumptions to the shell like body. It does not take account of the shear deformation. The kinematics assumptions of Kirchhoff-Love shell model are [109]: (a). The straight lines normal to the mid-surface remain straight after deformation. (b). The straight lines normal to the mid-surface remain normal to the mid-surface after deformation. (c). The shell thickness does not change.

The shell body is obtained by specifying the third parametric direction in equation (2.1) as the normal of the shell midsurface in both undeformed and deformed shell body, they are

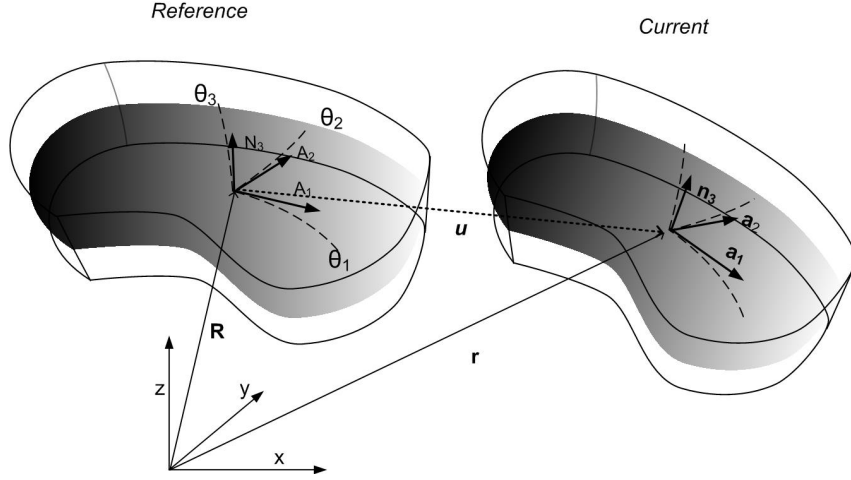


Figure 2.3: The deformation process of the Kirchhoff-Love shell body

$$\mathbf{X}(\theta^1, \theta^2, \theta^3) = \mathbf{R}_{KL}^0(\theta^1, \theta^2) + \theta^3 \mathbf{N}_3(\theta^1, \theta^2) \quad (2.23)$$

$$\mathbf{x}(\theta^1, \theta^2, \theta^3) = \mathbf{r}_{KL}^0(\theta^1, \theta^2) + \theta^3 \mathbf{n}_3(\theta^1, \theta^2). \quad (2.24)$$

Here, $()_{KL}$ is a note for the Kirchhoff-Love shell. $\theta^3 \in [-\frac{1}{2}t, \frac{1}{2}t]$, t is the thickness of the shell. \mathbf{N}_3 and \mathbf{n}_3 denote the normal of the shell surface before and after the deformation respectively. With above geometry descriptions, the three assumptions are all fulfilled. The normal vector are

$$\mathbf{N}_3 = \frac{\mathbf{A}_1 \times \mathbf{A}_2}{\|\mathbf{A}_3\|} \quad \mathbf{n}_3 = \frac{\mathbf{a}_1 \times \mathbf{a}_2}{\|\mathbf{a}_3\|}. \quad (2.25)$$

Where,

$$\mathbf{A}_3 = \mathbf{A}_1 \times \mathbf{A}_2, \quad \mathbf{a}_3 = \mathbf{a}_1 \times \mathbf{a}_2. \quad (2.26)$$

The covariant base vectors are

$$\mathbf{G}_\alpha = \mathbf{A}_\alpha + \theta^3 \mathbf{N}_{3,\alpha} \quad \mathbf{G}_3 = \mathbf{N}_3 \quad (2.27)$$

$$\mathbf{g}_\alpha = \mathbf{a}_\alpha + \theta^3 \mathbf{n}_{3,\alpha} \quad \mathbf{g}_3 = \mathbf{n}_3. \quad (2.28)$$

The deformation in the shell body is

$$\begin{aligned} \mathbf{u}_b &= \mathbf{x} - \mathbf{X} \\ &= \underbrace{(\mathbf{r} - \mathbf{R})}_\mathbf{u} + \theta^3 \underbrace{(\mathbf{n}_3 - \mathbf{N}_3)}_{\mathbf{v}(\mathbf{u})}. \end{aligned} \quad (2.29)$$

Here, \mathbf{u}_b is the displacement at a point in shell body. The aim of the reduction is to use

2. BASICS ON SHELL MODELS AND COMPUTER AIDED GEOMETRY DESIGN

the midsurface displacement \mathbf{u} to express the shell body kinematics. The strain tensor components are

$$\begin{aligned} E_{\alpha\beta} = & \frac{1}{2} (\mathbf{a}_\alpha \cdot \mathbf{a}_\beta - \mathbf{A}_\alpha \cdot \mathbf{A}_\beta) \\ & + \frac{1}{2} \theta^3 \{ (\mathbf{a}_\alpha \cdot \mathbf{n}_{3,\beta} + \mathbf{a}_\beta \cdot \mathbf{n}_{3,\alpha}) - (\mathbf{A}_\alpha \cdot \mathbf{N}_{3,\beta} + \mathbf{A}_\beta \cdot \mathbf{N}_{3,\alpha}) \} \\ & + \frac{1}{2} (\theta^3)^2 (\mathbf{n}_{3,\alpha} \cdot \mathbf{n}_{3,\beta} - \mathbf{N}_{3,\alpha} \cdot \mathbf{N}_{3,\beta}) \end{aligned} \quad (2.30)$$

$$E_{\alpha 3} = \frac{1}{2} (\mathbf{a}_\alpha \cdot \mathbf{n}_3 - \mathbf{A}_\alpha \cdot \mathbf{N}_3) + \frac{1}{2} (\theta^3) (\mathbf{n}_{3,\alpha} \cdot \mathbf{n}_3 - \mathbf{N}_{3,\alpha} \cdot \mathbf{N}_3) = 0 \quad (2.31)$$

$$E_{33} = \frac{1}{2} (\mathbf{n}_3 \cdot \mathbf{n}_3 - \mathbf{N}_3 \cdot \mathbf{N}_3) = 0 \quad (2.32)$$

The constant part in $E_{\alpha\beta}$ (2.30) reflects the membrane effect of the shell, the linear varying items denote the bending effect, the second order items are omitted, thus it can be furnished as,

$$\begin{aligned} E_{\alpha\beta} &= \varepsilon_{\alpha\beta} + \theta^3 \kappa_{\alpha\beta} \\ \varepsilon_{\alpha\beta} &= \frac{1}{2} (a_{\alpha\beta} - A_{\alpha\beta}) = \frac{1}{2} (\mathbf{a}_\alpha \cdot \mathbf{a}_\beta - \mathbf{A}_\alpha \cdot \mathbf{A}_\beta) \\ \kappa_{\alpha\beta} &= b_{\alpha\beta} - B_{\alpha\beta} = -\mathbf{a}_{\alpha,\beta} \cdot \mathbf{n}_3 + \mathbf{A}_{\alpha,\beta} \cdot \mathbf{N}_3 \end{aligned} \quad (2.33)$$

The internal virtual work in equation (2.22) can be obtained as

$$\begin{aligned} \delta \Pi_{int} &= \int_{\Omega} \mathbf{S} : \delta \mathbf{E} d\Omega \\ &= \int_{R_{KL}^0} \int_{-\frac{t}{2}}^{\frac{t}{2}} (\varepsilon_{\alpha\beta} + \theta^3 \kappa_{\alpha\beta}) C^{\alpha\beta\gamma\delta} \delta (\varepsilon_{\gamma\delta} + \theta^3 \kappa_{\gamma\delta}) Z(\theta^3) d\theta^3 d\Omega \\ &\approx t \int_{R_{KL}^0} \varepsilon_{\alpha\beta} C^{\alpha\beta\gamma\delta} \delta \varepsilon_{\gamma\delta} d\Omega + \frac{t^3}{12} \int_{R_{KL}^0} \kappa_{\alpha\beta} C^{\alpha\beta\gamma\delta} \delta \kappa_{\gamma\delta} d\Omega. \end{aligned} \quad (2.34)$$

In the above deduction, the $Z(\theta^3)$ is approximated as 1, the material tensor components also use the ones on the shell middle surface, it in fact assumes that those components do not vary along the θ^3 axis. All those approximations make this shell model only applicable for thin shell.

Writing the above items in matrix from, the following expressions can be obtained,

$$\boldsymbol{\varepsilon}^T = [\varepsilon_{11}, \varepsilon_{22}, 2\varepsilon_{12}], \boldsymbol{\kappa}^T = [\kappa_{11}, \kappa_{22}, 2\kappa_{12}]^T \quad (2.35)$$

$$\mathbf{D} = \begin{bmatrix} C^{1111} & C^{1122} & C^{1112} \\ sym & C^{2222} & C^{2212} \\ sym & sym & C^{1212} \end{bmatrix} \quad (2.36)$$

Here,

$$C^{\alpha\beta\gamma\delta} = \lambda A^{\alpha\beta} A^{\gamma\delta} + \mu (A^{\alpha\gamma} A^{\beta\delta} + A^{\alpha\delta} A^{\beta\gamma}) \quad (2.37)$$

Equation (2.38) can be expressed as

$$\delta\Pi_{int} \approx t \int_{R_{KL}^0} \boldsymbol{\varepsilon}^T \mathbf{D} \delta \boldsymbol{\varepsilon} d\Omega + \frac{t^3}{12} \int_{R_{KL}^0} \boldsymbol{\kappa}^T \mathbf{D} \delta \boldsymbol{\kappa} d\Omega \quad (2.38)$$

Here, the integral domain R_{KL}^0 is the shell midsurface, \mathbf{u} denotes the shell midsurface displacement field, t is the shell thickness. All the values here refer to the shell midsurface.

In Kirchhoff-Love shell model, the transverse strains are zero. The shear deformation has not been taken into consideration.

The PDE form control equation of shell model is not so visible, we would like to present the PDE form Kirchhoff-Love plate control equation [109] here, it has the same model assumptions with the Kirchhoff-Love shell. However, the plate is a flat area in two dimensional space, only a Cartesian coordinate system is enough to describe it. For a pure bending plate, the PDE form control can be explicitly furnished as

$$\frac{\partial^4 w}{\partial x^4} + \frac{\partial^4 w}{\partial x^2 \partial y^2} + \frac{\partial^4 w}{\partial y^4} = 0, \quad (2.39)$$

The bending load is

$$\begin{bmatrix} M_{xx} \\ M_{yy} \\ M_{xy} \end{bmatrix} = -\frac{2t^3 E}{3(1-\nu^2)} \begin{bmatrix} 1 & \nu & 0 \\ \nu & 1 & 0 \\ 0 & 0 & 1-\nu \end{bmatrix} \begin{bmatrix} w_{,xx} \\ w_{,yy} \\ w_{,xy} \end{bmatrix}. \quad (2.40)$$

It can be seen that the control equation is a forth order PDE. The shell equation is also of this type and more complicated. When FEM method is used to solve it, at least C^1 continuous shape functions should be used. However, such type of shape functions are difficult to construct. This is the motivation of development of Reissner-Mindlin shell model which is easy to be solved by FEM.

2.1.4 Reissner-Mindlin shell model

The Kirchhoff-Love shell model, due to the geometry and kinematics assumptions, the transverse shear deformation is zero. This is not the fact in the real three dimensional solid case. In this subsection, we will present another shell model Reissner-Mindlin shell which can take account of such deformation. The shell assumption of Reissner-Mindlin model

2. BASICS ON SHELL MODELS AND COMPUTER AIDED GEOMETRY DESIGN

succeeds the ones from the Kirchhoff-Love shell with a relaxation in the shell director behaviour, it no need to be the normal vector of the deformed surface, but its length should be constant. Another assumption is that the transverse normal stress equals zero.

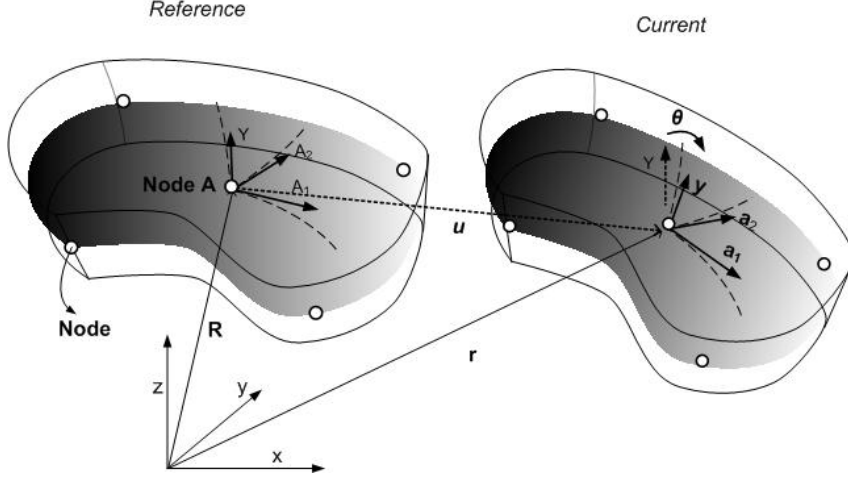


Figure 2.4: The deformation process of the Reissner-Mindlin shell body

There are also many methods to obtain the Reissner-Mindlin shell model. In this section, we will present the degenerated shell Reissner-Mindlin model, it adopts another way of deducing. It starts from the discrete model.

The shell geometry is expressed as

$$\mathbf{X} = \sum_A N_A(\varepsilon, \eta) \left(\mathbf{X}_A + \frac{t_A}{2} \varsigma \mathbf{y}_A \right). \quad (2.41)$$

The shell surface is expressed as

$$\mathbf{R}_{KL}^0 = \sum_A N_A(\varepsilon, \eta) \mathbf{X}_A. \quad (2.42)$$

The shell kinematics is directly given as

$$\mathbf{u} = \sum_A N_A(\varepsilon, \eta) \left(\mathbf{u}_A + \frac{h_A}{2} \varsigma \mathbf{y}'_A \right). \quad (2.43)$$

Here, N_A is the basis function. t_A is the shell thickness at node A, \mathbf{X} denotes the position vector of a point in the shell body. \mathbf{y}_A denotes the fiber vector at the node A in the initial shell. \mathbf{u} denotes the displacement at the point $\mathbf{X}(\varepsilon, \eta, \varsigma)$, \mathbf{u}_A denotes the displacement at node A, \mathbf{y}'_A indicates the shell fiber rotation.

The linear strain \mathbf{E}^L (2.13) is used here. Its voigt notation is

$$\hat{\boldsymbol{\varepsilon}}^T = [E_{11}^L, E_{22}^L, 2E_{12}^L, 2E_{13}^L, 2E_{23}^L]. \quad (2.44)$$

2. Basics on shell models and computer aided geometry design

The material tensor components are based on the three dimensional ones in equation (2.16), with the imposing of strain and stress assumptions. In Cartesian coordinates system, the material matrix is,

$$\bar{\mathbf{D}} = \frac{E}{(1+\nu)(1-2\nu)} \begin{bmatrix} 1-\nu & \nu & \nu & 0 & 0 & 0 \\ \nu & 1-\nu & \nu & 0 & 0 & 0 \\ \nu & \nu & 1-\nu & 0 & 0 & 0 \\ 0 & 0 & 0 & \frac{1-\nu}{2} & 0 & 0 \\ 0 & 0 & 0 & 0 & \frac{1-\nu}{2} & 0 \\ 0 & 0 & 0 & 0 & 0 & \frac{1-\nu}{2} \end{bmatrix}. \quad (2.45)$$

The zero transverse normal strain and stress assumptions bring about relation between the material tensor components as following

$$\bar{S}_{33} = \frac{E}{(1+\nu)(1-2\nu)} \{ \nu(\bar{E}_{11} + \bar{E}_{22}) + (1-\nu)\bar{E}_{33} \} = 0. \quad (2.46)$$

With this relation, a condensation of the matrix $\bar{\mathbf{D}}$ can be achieved. On the other hand, as a result of the kinematics assumption, there will be a constant transverse shear distribution along the thickness direction, this is far from the common sense, a modification of the transverse shear related material tensor components is thus needed [99, 100]. The final material matrix is

$$\hat{\mathbf{D}} = \frac{E}{1-\nu^2} \begin{bmatrix} 1 & \nu & 0 & 0 & 0 \\ \nu & 1 & 0 & 0 & 0 \\ 0 & 0 & \frac{1-\nu}{2} & 0 & 0 \\ 0 & 0 & 0 & \alpha_s \frac{1-\nu}{2} & 0 \\ 0 & 0 & 0 & 0 & \alpha_s \frac{1-\nu}{2} \end{bmatrix}. \quad (2.47)$$

Here, the zero transverse normal stress and strain have been considered. α_s is the shear correction factor, α_s is usually taken as $\frac{5}{6}$, it is included to correct the constant transverse shear strain distribution. It is noteworthy that $\hat{\mathbf{D}}$ is obtained from a Cartesian coordinates system and thus only holds in such a case.

The control equation is stated as

$$\delta \Pi_{int} = \int_{R_{RM}^0} \hat{\boldsymbol{\varepsilon}}^T \hat{\mathbf{D}} \delta \hat{\boldsymbol{\varepsilon}} d\Omega = \delta \Pi_{ext}. \quad (2.48)$$

There are other ways of obtaining the Reissner-Mindlin shell model, the further details could be obtained in book [23] and [77].

In Reissner-Mindlin shell, the transverse normal strain and stress are all zero. The PDE form shell control equation is hard to formulate, here we present a plate case as following

$$\nabla^2 \left(\frac{\partial \varphi_x}{\partial x} + \frac{\partial \varphi_y}{\partial y} \right) = -\frac{q}{D} \quad (2.49)$$

$$\nabla^2 w - \frac{\partial \varphi_x}{\partial x} - \frac{\partial \varphi_y}{\partial y} = -\frac{q}{\kappa G t} \quad (2.50)$$

$$\nabla^2 \left(\frac{\partial \varphi_x}{\partial y} - \frac{\partial \varphi_y}{\partial x} \right) = -\frac{\kappa G t}{D(1-\nu)} \left(\frac{\partial \varphi_x}{\partial y} - \frac{\partial \varphi_y}{\partial x} \right) \quad (2.51)$$

The loads are

$$\begin{bmatrix} M_{xx} \\ M_{yy} \\ M_{xy} \end{bmatrix} = -\frac{2t^3 E}{3(1-\nu^2)} \begin{bmatrix} 1 & \nu & 0 \\ \nu & 1 & 0 \\ 0 & 0 & 1-\nu \end{bmatrix} \begin{bmatrix} \varphi_{x,x} \\ \varphi_{y,y} \\ \frac{1}{2}(\varphi_{x,y} + \varphi_{y,x}) \end{bmatrix}, \quad (2.52)$$

$$\begin{bmatrix} Q_x \\ Q_y \end{bmatrix} = \kappa G t \begin{bmatrix} w_{,x} - \varphi_x \\ w_{,y} - \varphi_y \end{bmatrix}. \quad (2.53)$$

with,

$$D = \frac{Et^3}{12(1-\nu^2)}, \quad G = \frac{E}{2(1+\nu)}. \quad (2.54)$$

Here, q is the distributed force load. Q indicates the shear force. The kinematics of plate is expressed by the displacement w and the rotations φ_x and φ_y , this breaks the relation between the rotation and the midsurface displacement in Kirchhoff-Love shell. Although more equations and variables are needed in this model, the complexity of equation is reduced, when using FEM method to solve it, C^0 continuous basis functions can now be used. This made the Reissner-Mindlin shell more popular than the Kirchhoff-Love shell. Of course, directly obtaining the rotation angle is another benefit.

2.2 Computer aided geometry design

Curves are utilized by the draftsmen for centuries. They are the basic components of the design of geometries such as ship hull, architecture and mechanical parts. The simple curves, like the straight line or circles, can be easily created with rulers or compasses. However, for a more general design case, where the designer only require the curve have a reasonable shape, its exact drawing will be a little difficult. Before the invention of CAGD, they are drawn with the tools French curve and spline. Designers could construct the curves by combining different parts of a template curve of French curve or moving the ducks of the spline. The manual blueprints are hard to be reproduced exactly and also cannot meet the requirements of computer controlled manufacturing machine.

The computer aided geometry design is a topic about the description, store and exchange of geometries, e.g. curves, surfaces and bodies, in computers. The essential focus

are the mathematical descriptions of the geometries and the related geometry manipulation techniques. It was developed to meet the urgent demand for precise graphics store and display in computers. Its development also closely relates to the development of computers. The terminology computer aided geometry design (CAGD) was coined by R.Barnhill and R.Riesenfeld in 1974 when the first conference on this topic was held [12].

The development of CAGD is a long history, one can refer to paper [56]. In 1963, Ferguson proposed the concept of parametric expression of curves and surfaces. The surface and curves are expressed by the vector functions of parameters. He used a method to construct bicubic surfaces by the positions and the derivatives information of the four corner of the patch [58, 59]. The twists at the corner of the patch are set to zero. It is named F-patches. In 1964, Coons proposed a method to build a parametric surface based on the four arbitrary boundary curves of the surface. It is well known as bilinearly blended Coons patch [36]. The concept of this method is labelled as transfinite interpolation. W. Gordon and General Motors generalized his work so that the surface can be built from a rectangular network of curves [66, 67]. Coons's method did not set restrictions on the type of boundary curves, however, since the widely used curves are bicubic, when adopting them and further set the corner twists to zero, the obtained surface turns out to be F-patch. Coons patch is convenient for the single smooth surface construction, however for multiple patches, the overall smoothness requirement might be difficult to reach.

In the late 1950s, Paul de Faget de Casteljau who worked in the car company Citroen in France developed a method that can describe and manipulate the curves and surfaces in an intuitive way. In his scheme, the curve was controlled by a control polygon whose vertexes are the discrete design points, the curve lies within the convex hull of the control polygon, when moving the vertexes, the curves follows in an intuitive way. His method was kept as a commercial secrete for a long time. In 1971, another engineer Bezier in Renault, which is also a car company in France, proposed the similar method. But the initial mathematical formula was wired and lack of intuition. Forrest [60] discovered that Bezier's expression can be expressed in terms of Bernstein polynomials, which had been used in Casteljau's method. The two methods were proved to be identical. Bezier technique was a breakthrough in the CAGD research, it solved the problem elegantly. It also greatly inspired the researchers in this field, some of them played a leading role in the invention of B-spline in CAGD. However the local modification and connection problem also existed in this method.

The first paper about spline was written by Schoenberg in 1946 [119] (published in 1967), due to the tedious and unstable algorithm, it did not attract much attention until de Boor [46] and Cox [40] independently developed a simple and stable recursive algorithm for the evaluation of B-spline, the de Boor algorithm, in 1972. However, the research focus was the function approximation. Gordon and Riesenfeld [68] originally used this method into the CAGD society in 1974 based on their profound research on Bezier technique.

2. BASICS ON SHELL MODELS AND COMPUTER AIDED GEOMETRY DESIGN

They found de Boor's recursive B-spline evaluation was a natural generalization of the de Casteljau algorithm. They proposed systematically the B-spline technique. This method succeed all the advantages of the Bezier method, since Bezier became its subset. It can easily achieve the local manipulation at the same time keep the overall smoothness.

Conic curves, like circles, are indispensable ingredients in mechanical design, e.g. the drawing of the shaft and bolt. B-spline is powerful in free form curve description, however it cannot express the conic curve exactly. Using two languages in the design system led to a lot of trouble. To overcome this, Versprille [132] proposed the rational B-spline. It can express the conic curves exactly, B-spline became its special case. It finally became the Initial Graphics Exchange Specification (IGES) standard in 1983 [111]. The important techniques in NURBS are the knot insertion [25, 35] and order elevation algorithms [60, 105]. It is the dominant CAGD tool which is widely utilized in the present commercial software. The NURBS has an tensor product topology definition, more control points are needed not for describing the geometry itself but for meeting this topology restriction. As a remedy, Sederberg et al [120, 121] proposed the T-spline technique in 2003, it attracts a lot of attention in recent years and has been adopted in the commercial software Rhinoceros.

In the present work, we emphasize on the NURBS technique. Our work is focused on the NURBS based Isogeometric analysis. In the following, we will introduce it as a foundation for the IGA.

2.2.1 B-spline

B-spline Curve

The B-spline curve is defined as following

$$\mathbf{C}(\xi) = [x, y, z]^T = \sum_{i=1}^n \mathbf{P}_i N_i(\xi). \quad (2.55)$$

Here, $\mathbf{C} : \mathbb{R} \rightarrow \mathbb{R}^3$ is a single variable vector function about ξ . $\mathbf{P}_i = [P_i^x, P_i^y, P_i^z]^T$ is a spatial point, it is the control point. The basis function $N_i(\xi) : \mathbb{R} \rightarrow \mathbb{R}$ is a single variable scalar function, it is a B-spline. $\mathbf{C}(\xi)$ is a B-spline curve. A B-spline curve example is shown in figure 2.5.

The B-spline basis functions are defined recursively as

$$N_{i,0}(\xi) = \begin{cases} 1 & \text{if } \xi_i \leq \xi < \xi_{i+1} \\ 0 & \text{otherwise} \end{cases} \quad (2.56)$$

$$N_{i,p}(\xi) = \frac{\xi - \xi_i}{\xi_{i+p} - \xi_i} N_{i,p-1}(\xi) + \frac{\xi_{i+p+1} - \xi}{\xi_{i+p+1} - \xi_{i+1}} N_{i+1,p-1}(\xi) \quad (2.57)$$

It is defined over a non-decreasing set which is named as knot vector, $\Xi = \{\xi_1, \xi_2, \dots, \xi_{p+n+1}\}$.

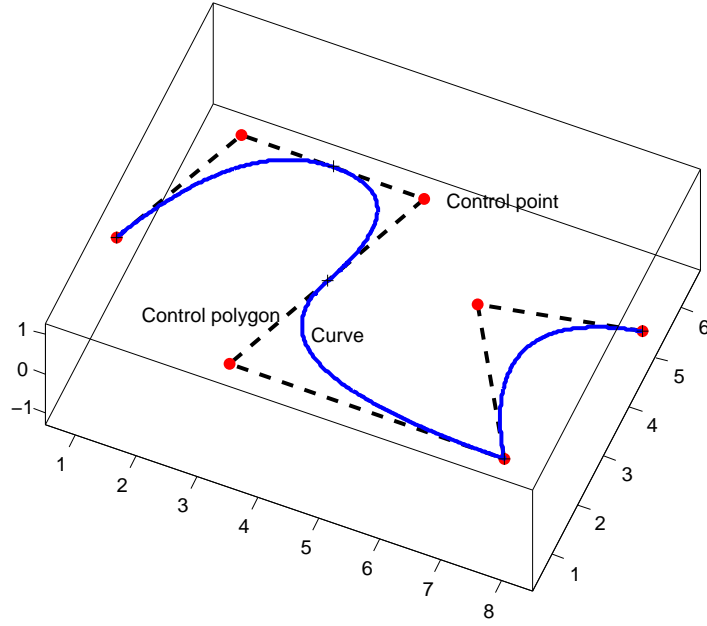


Figure 2.5: A three dimensional B-spline curve. The curve lies within the convex hull of the control polygon. The curve is composed of four quadratic polynomial curve pieces. The knot vector is $\Xi = \{0, 0, 0, 0.25, 0.5, 0.75, 0.75, 1, 1, 1\}$.

$\xi_i \in \mathbb{R}$ is the i th knot. $p + n + 1$ is the total number of knots. Each B-spline is a piecewise function. n is the the number of basis functions with order p . $[\xi_i, \xi_{i+1}]$ is a knot span. If a knot appears k times, it is said to be of a multiplicity k . If the knots are equidistant, the knot vector is uniform. If not, it is non-uniform. If the boundary knots have multiplicity $p + 1$, the spline is said to be open. The common used spline in IGA is open. Figure 2.6 shows a example of a second order basis function.

There are n basis functions defined over the knot vector, figure 2.7 shows an example of a basis function.

The properties of B-spline are

- B-spline are non-negative, i.e., $N_i(\xi) \geq 0, \forall \xi$.
- B-spline have compact support, the support of $N_i(\xi)$ is $[\xi_i, \xi_{i+p+1}]$.
- B-splines form a partition of unity, i.e., $\sum_i^n N_i = 1, \forall \xi$.
- The part of N_i in each non-zero knot span $[\xi_i, \xi_{i+1}]$ is a polynomial of order p .
- The continuity of $N_i(\xi)$ across a knot of multiplicity k is $p - k$.

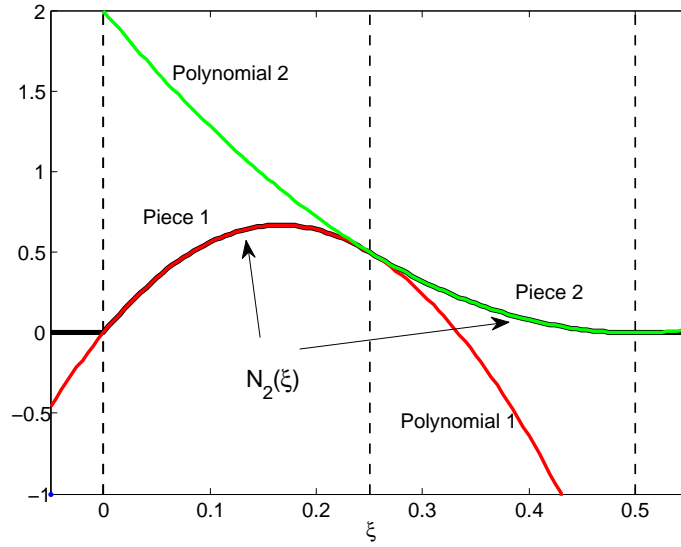


Figure 2.6: The basis function $N_2(\xi)$ curve. It is composed of two pieces of quadratic polynomial curve. The full polynomial curves are also depicted. It is defined on $\Xi = \{0, 0, 0, 0.25, 0.5, 0.75, 0.75, 1, 1, 1\}$.

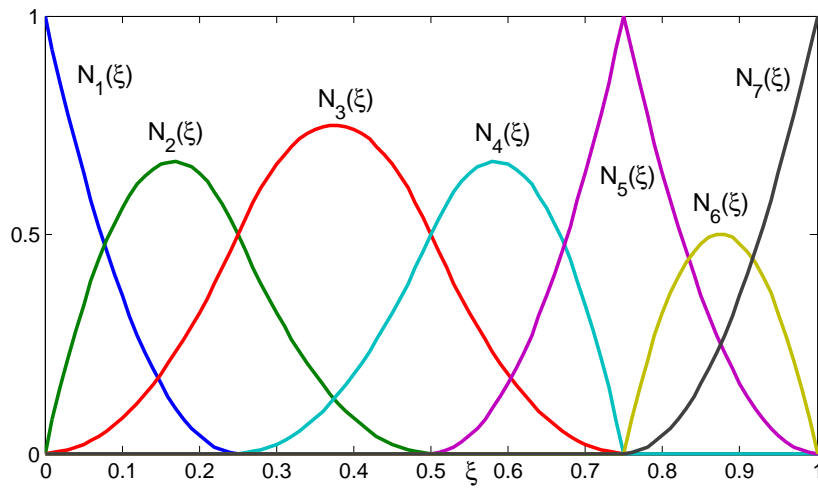


Figure 2.7: The basis functions on $\Xi = \{0, 0, 0, 0.25, 0.5, 0.75, 0.75, 1, 1, 1\}$. There are seven quadratic basis functions.

B-spline Surface

The B-spline surface is defined as following

$$\mathbf{S}(\xi, \eta) = [x, y, z]^T = \sum_{i=1}^n \sum_{j=1}^m \mathbf{P}_{i,j} N_{i,p}(\xi) N_{j,q}(\eta) \quad (2.58)$$

Here, $\mathbf{S} : \mathbb{R}^2 \rightarrow \mathbb{R}^3$ is a vector function of two variables ξ and η . $\mathbf{P}_{i,j}$ is also the control point. $N_{i,p}(\xi)$ and $N_{j,q}(\eta)$ are univariate basis functions of order p and q respectively, figure 2.8 shows a B-spline surface example.

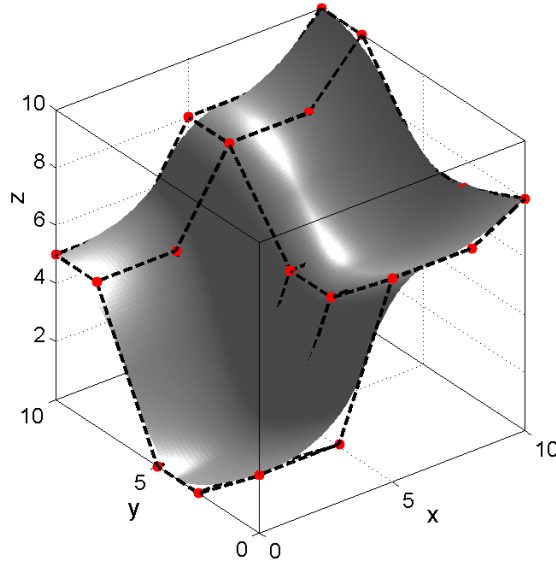


Figure 2.8: A B-spline surface example.

There are $n \times m$ basis functions, they can be viewed as tensor product of the univariate ones, figure 2.10 shows the basis functions in the previous B-spline surface.

The bivariate basis function is

$$\hat{N}_{i_j}(\xi, \eta) = N_i(\xi) N_j(\eta). \quad (2.59)$$

Here, the index $i_j \in [1, mn]$, it is arranged in the sequence $i_j = (i = 1, 2, \dots, m) + m \times (j = 1 - 1), \dots, (i = 1, 2, \dots, m) + m \times (j = n - 1)$. The control points are also arranged in such sequence, then the B-spline surface can be expressed as

$$\mathbf{S}(\xi, \eta) = \sum_{i_j=1}^{mn} \hat{\mathbf{P}}_{i_j} \hat{N}_{i_j}(\xi, \eta). \quad (2.60)$$

The basis function $\hat{N}_{i_j}(\xi, \eta)$ also have partition of unity, local support and non-negative properties. Figure 2.11 shows \hat{N}_3 . The partition of unity property makes the B-spline have the affine invariant property. It means that any affine transformation of the spline

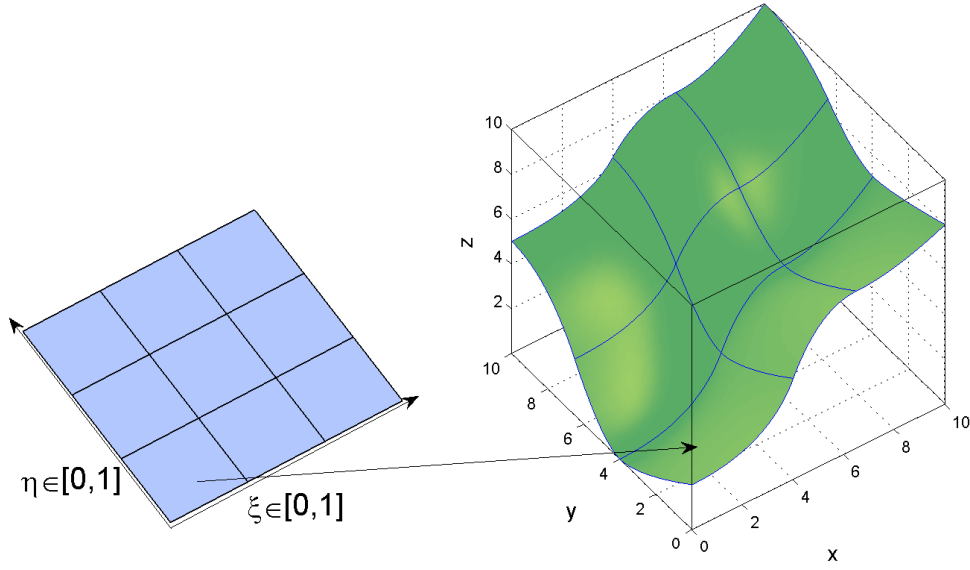


Figure 2.9: The map from the parametric space $[0, 1]^2$ to \mathbb{R}^3 in a B-spline surface.

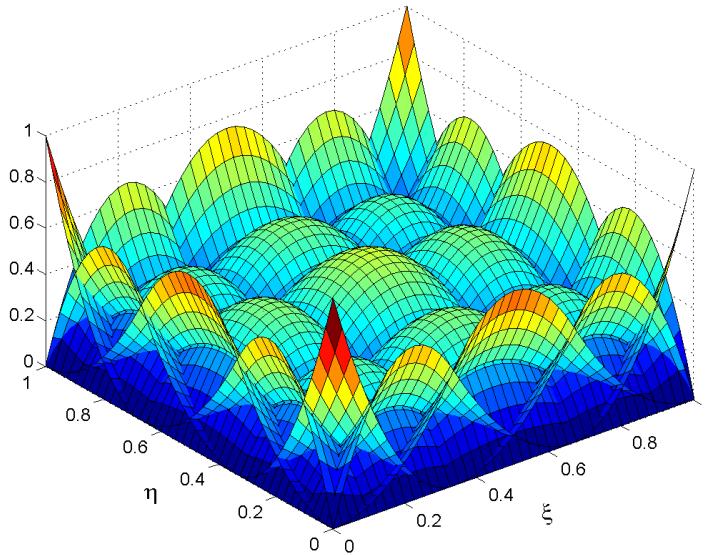


Figure 2.10: An example of bivariate B-spline, it can be viewed as an tensor product of the univariate ones. The univariate knot vectors are $\Xi_\xi = \Xi_\eta = \{0, 0, 0, \frac{1}{3}, \frac{2}{3}, 1, 1, 1\}$

can be obtained by applying it directly to the control points. This is meaningful when using such basis in mechanical analysis.

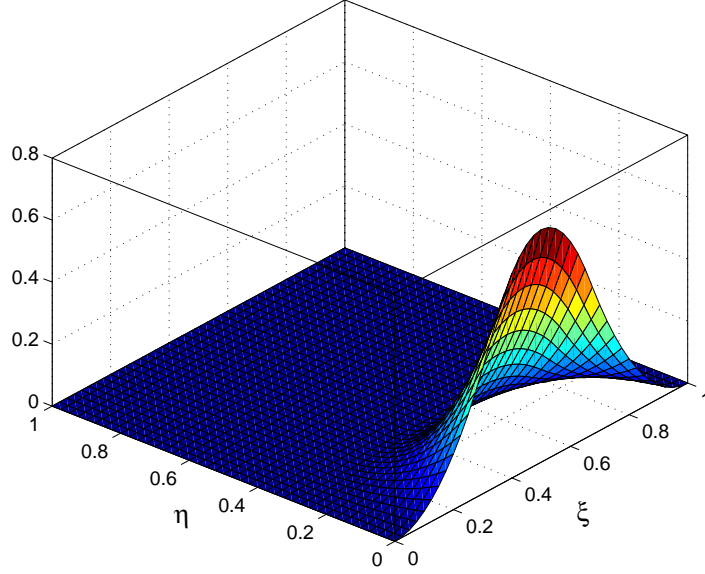


Figure 2.11: An example of bivariate B-spline \hat{N}_3 , The univariate knot vectors are $\Xi_\xi = \Xi_\eta = \{0, 0, 0, \frac{1}{3}, \frac{2}{3}, 1, 1, 1\}$

2.2.2 Non-uniform rational B-spline

Perspective map

A spatial point $\mathbf{P} = [P_x, P_y, P_z]^T$ can also be expressed with homogeneous coordinates $\mathbf{P}^w = [wP_x, wP_y, wP_z, w]^T$. The initial three dimensional coordinates can be obtained with perspective projection from the four dimensional space to the hyper plane $w = 1$, the perspective map is defined as

$$\mathbf{P} = \mathbf{H}(\mathbf{P}^w) = \begin{cases} \left[\frac{wP_x}{w}, \frac{wP_y}{w}, \frac{wP_z}{w} \right]^T, & w \neq 0 \\ [P_x, P_y, P_z]^T, & w = 0 \end{cases} \quad (2.61)$$

NURBS Curve

NURBS is a perspective projection from a one dimensional higher B-spline, a three dimensional NURBS curve is thus obtained as,

$$\mathbf{C}(\xi) = \sum_{i=1}^n \mathbf{P}_i \frac{w_i N_i(\xi)}{\sum_{j=1}^n w_j N_j(\xi)}. \quad (2.62)$$

2. BASICS ON SHELL MODELS AND COMPUTER AIDED GEOMETRY DESIGN

Here, P_i is the control point, w is called weight. Figure 2.12 shows an example of this projection procedure. The NURBS basis function can thus be obtained as

$$R_i^p(\xi) = \frac{w_i N_i(\xi)}{\sum_{j=1}^n w_j N_j(\xi)}. \quad (2.63)$$

In addition to the knot vector which had appeared in B-spline, the weight here also controls the shape. With this enrichment, all the conic curves can be expressed. Figure 2.13 shows an NURBS curve example.

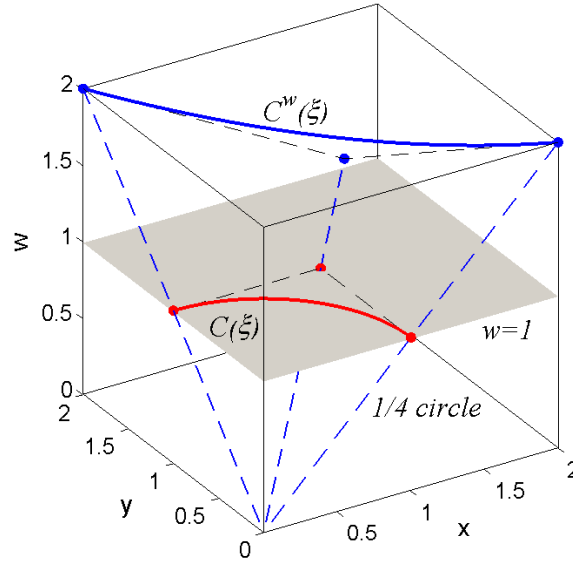


Figure 2.12: B-spline curve projected to plane $w = 1$ to obtain an NURBS expressed arc.

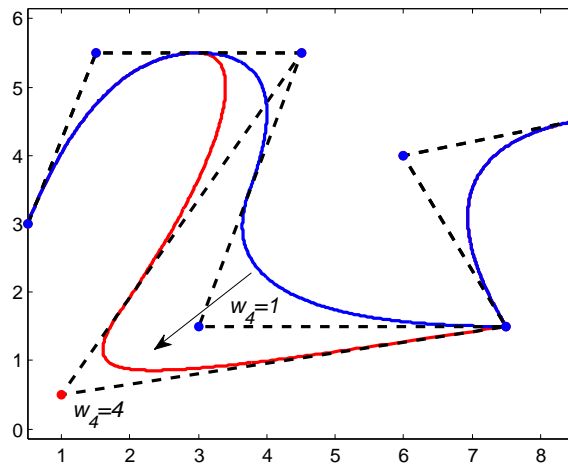


Figure 2.13: An NURBS curve example.

NURBS Surface

With the perspective projection, the NURBS surface can also be obtained from a one dimension higher B-spline surface, it is expressed as

$$\mathbf{S}(\xi, \eta) = \sum_{i=1}^n \sum_{j=1}^m \mathbf{P}_{i,j} \frac{N_{i,p}(\xi) N_{j,q}(\eta) w_{i,j}}{\sum_{k=1}^n \sum_{l=1}^m N_{k,p}(\xi) N_{l,q}(\eta) w_{k,l}} \quad (2.64)$$

The basis functions are

$$R_{i,j}^{p,q}(\xi, \eta) = \frac{N_{i,p}(\xi) N_{j,q}(\eta) w_{i,j}}{\sum_{k=1}^n \sum_{l=1}^m N_{k,p}(\xi) N_{l,q}(\eta) w_{k,l}}. \quad (2.65)$$

Here, $N(\xi)$ and $N(\eta)$ indicate the one dimensional B-spline. $w_{i,j}$ are the weight. It can be seen that the weight affects the basis function itself. This is different with the case in B-spline, where the modification is reached only by modifying the control points, the basis functions are unchanged. The three important properties of B-spline also hold for NURBS. One can also arrange the indices i, j into a single index in the way mentioned in B-spline. Figure shows a NURBS surface obtained by setting the $w_{13} = 0.7$ of the B-spline surface in figure 2.8 while keeping coefficients unchanged. The basis functions are also shown here, one can compare them with the figure 2.10.

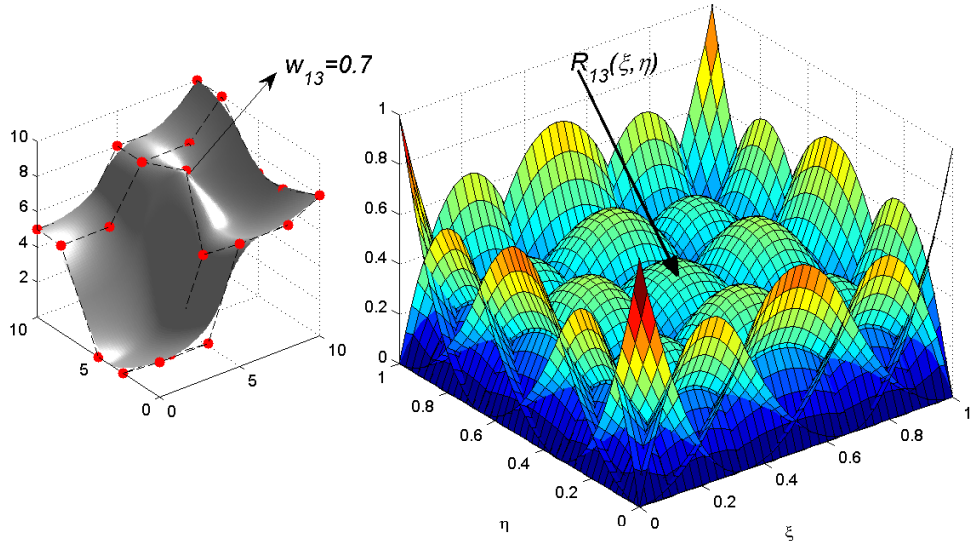


Figure 2.14: An NURBS surface and the corresponding basis functions obtained by setting $w_{13} = 0.7$ in the B-spline surface 2.8.

2.2.3 NURBS operation

There are two methods to enrich the functional space of B-spline, the knot insertion and the order elevation. They will not affect the parametrization of the B-spline curves and surfaces. After the operation, more control points are obtained, thus more flexibility are provided to the designer, one can further adjust the control points to modify the shape. The NURBS operation is the operations of the higher dimension B-spline.

Knot insertion

Knot insertion denotes an operation that adding a knot $\hat{\xi} \in [\xi_k, \xi_{k+1})$ to an existing knot vector Ξ . After the operation, there will be one more knots, consequently there will also be an increase in the number of control points. However, neither the shape nor the parametrization is changed. Here we present the algorithm that can insert a single knot each time. The control points after knot insertion is denoted as $\hat{\mathbf{P}}$, they are

$$\hat{\mathbf{P}} = \alpha_i \mathbf{P}_i + (1 - \alpha_i) \mathbf{P}_{i-1}. \quad (2.66)$$

Where,

$$\alpha_i = \begin{cases} 1 & \text{if } i \leq k - p \\ \frac{\hat{\xi} - \xi_i}{\xi_{i+p} - \xi_i} & \text{if } k - p + 1 \leq i \leq k \\ 0 & \text{if } i \geq k + 1 \end{cases} \quad (2.67)$$

The new control points are the linear combination of the original ones. Some algorithms can be found in the literatures [25, 35, 47, 63]. Figure 2.15 shows an knot insertion example.

Order elevation

Order elevation is a operation that increase the polynomial order of the spline. The order elevation does not affect the shape or its parametrization. One can expand the B-spline into Bezier, then elevate the order of the Bernstein polynomials, finally delete the redundant knots and merge the Bezier to the B-spline. This operation does not change the continuity of the basis functions. The algorithms can be found in literatures [60, 76, 103, 105]. Figure 2.16 shows an example of order elevation from the quadratic NURBS to cubic NURBS.

2.3 Isogeometric analysis

Isogeometric analysis (IGA) was introduced by Thomas [79] in 2005. The concept of isogeometric analysis is using geometrically exact model in the analysis. The comparison object is the traditional FEM. In the industrial analysis pipeline, the objects are

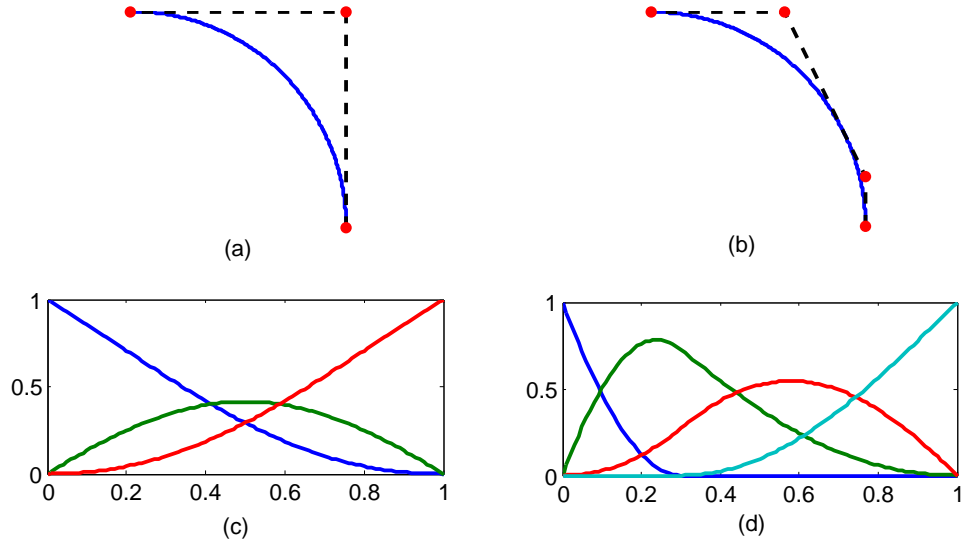


Figure 2.15: Insertion of new knot 0.3 into the knot vector $\{0,0,0,1,1,1\}$. (a) and (b) show the curve before and after insertion, (c) and (d) show the corresponding basis functions.

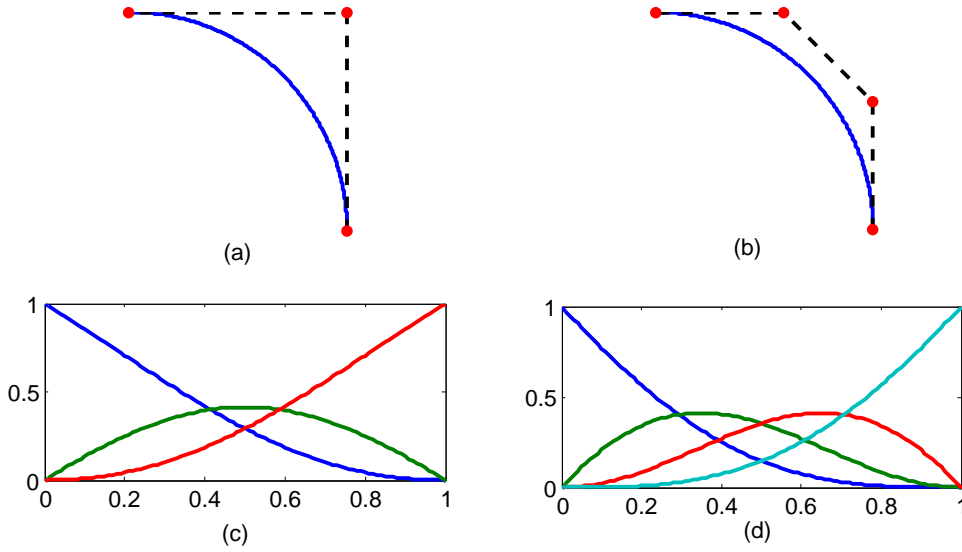


Figure 2.16: Order elevation of a NURBS curve, the original knot vector is $\{0,0,0,1,1,1\}$, the result knot vector is $\{0,0,0,0,1,1,1,1\}$, (a) and (b) show the curve before and after insertion, (c) and (d) show the corresponding basis functions.

firstly modelled with CAD software, the CAD models are later meshed for implementing FEM. The mesh creation achieves the model transformation from the CAD to the FEM. This procedure is neither exact nor seamless. The initial CAD models are approximated by piecewise quadrilateral or triangular surfaces. This is geometrically non-exact. The emerging of IGA is aiming at bridging such gap. The tool adopted is using the same functional space to express the geometry (the analysis domain) and the unknown fields in it.

2. BASICS ON SHELL MODELS AND COMPUTER AIDED GEOMETRY DESIGN

The weak form control equations of the mechanical problems are often formulated as

$$\begin{aligned} & \text{find } u \in V, \text{ such that} \\ & a(u, v) = \langle l, v \rangle \quad \forall v \in V. \end{aligned} \quad (2.68)$$

Here, u and v are unknown functions, l is a known function. $a(u, v) : V \times V \rightarrow \mathbb{R}$ is a bilinear form functional, $\langle l, v \rangle$ is a linear functional. In mechanical analysis, such equation is formed by virtual work principle, equation (2.22), or other variational principles. Let us repeat equation (2.22) here,

$$\underbrace{\int_{\Omega} \mathbf{S} : \delta \mathbf{E} d\Omega}_{a(\mathbf{u}, \delta \mathbf{u})} = \underbrace{\int_{\Omega} \rho \mathbf{b} \cdot \delta \mathbf{u} d\Omega + \int_{\Gamma_{\sigma}} \mathbf{t} \cdot \delta \mathbf{u} d\Omega}_{(l, \delta \mathbf{u})}. \quad (2.69)$$

What we referred to as analysis is to properly chose the functional space V to expand the unknown variables and then find the solution of (2.68). Such a functional space is normally expanded by a set of basis functions. In traditional FEM, Lagrange based basis are commonly used. In IGA analysis, the basis functions which are used in the geometry describing, such as NURBS [64] and T-spline [135], are usually used.

It can be seen that the innovation of the IGA method lies within the equation solving method, it can be viewed as an isoparametric FEM method which adopts a geometrically exact map. As for the forming of the equation itself, there is no difference. As a result, normally wherever FEM is used, IGA can also be used, such as in electromagnetic [29], contact [92], fluid [65] and fluid structure coupling problems [15].

Take NURBS based IGA (bivariate) as an example, the geometry of the domain (A NURBS surface) is expressed as,

$$\mathbf{S}(\xi, \eta) = \sum_{i_j=1}^{mn} \mathbf{P}_{i_j} R_{i_j}. \quad (2.70)$$

The elements of the IGA are the non-zero knot spans in the parametric domain, denoted as

$$e = [\xi_i, \xi_{i+1}) \otimes [\eta_i, \eta_{i+1}), \|e\| \neq 0. \quad (2.71)$$

The elements in the physical space are denoted as

$$e^p = \mathbf{S}(e). \quad (2.72)$$

The control points of the surface are viewed as the nodes in FEM. One can see figure 2.8 and 2.9 to have a direct impression about those concepts.

2. Basics on shell models and computer aided geometry design

The NURBS space on the parametric domain $[0, 1]^2$ is denoted as

$$V_{para} = span\{R_{i_j}\}_{i_j=1,\dots,mn}. \quad (2.73)$$

For unknown function approximation in IGA, it expands the unknown fields in the physical space, the solution space V is thus denoted as

$$V = span\{R_{i_j}(\xi, \eta) \circ \mathbf{S}^{-1}\}_{i_j=1,\dots,mn}. \quad (2.74)$$

The elements creation in IGA is achieved by knot insertion or the order elevation of the NURBS. We have mentioned before, those operations do not affect the shape itself, however it will add more basis functions. From the analysis point of view, more basis function indicates an extension of the initial function space, more accurate solution thus could be expected. This corresponds to the mesh refinement in FEM. There are three ways of mesh refinements named h , p and k refinements in IGA, they are replying on the knot insertion, order elevation and both respectively. The first two methods correspond to the similar concepts in traditional FEM, that are increasing the number of basis functions by creating more elements or elevating the order of the basis functions. However, the third one is exclusively owned by the IGA, it is induced by the fact that the sequence of knot insertion and order elevation affects the ultimate basis functions. If we elevate the order of the spline then insert the knot, it will give different functions than what we obtained from implementing them in the reverse order. Figure 2.17 shows a refinement example.

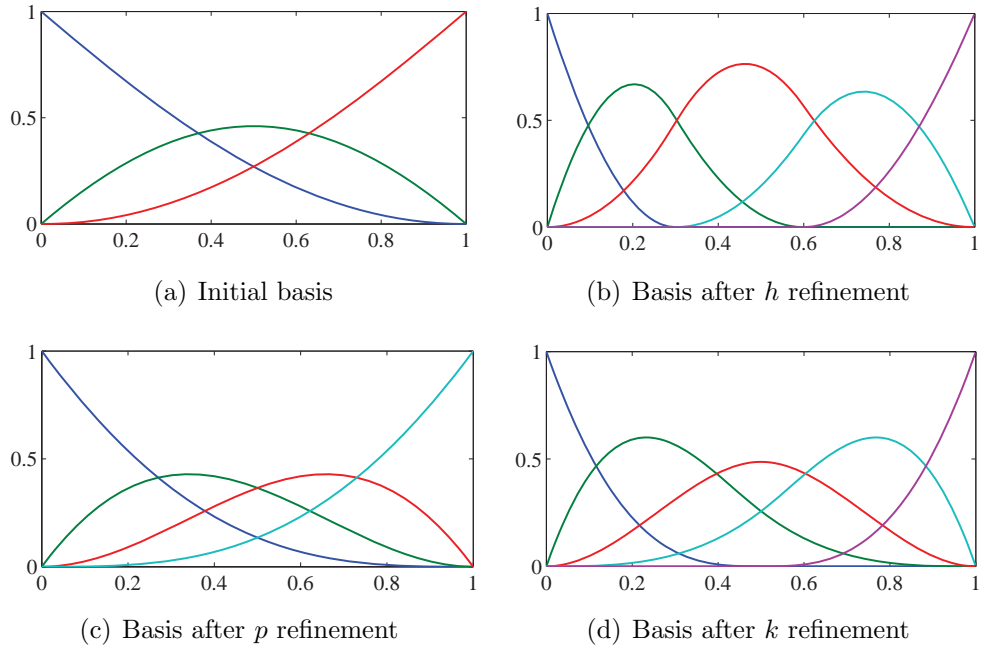


Figure 2.17: Examples of the IGA basis functions after refinements. Spline order and knot vectors : (a) $p=2$, $\Xi = \{0, 0, 0, 1, 1, 1\}$. (b) $p=2$, $\Xi = \{0, 0, 0, 0.3, 0.6, 1, 1, 1\}$. (c) $p=3$, $\Xi = \{0, 0, 0, 0, 1, 1, 1, 1\}$. (d) $p=3$, $\Xi = \{0, 0, 0, 0, 0.5, 1, 1, 1, 1\}$.

2. BASICS ON SHELL MODELS AND COMPUTER AIDED GEOMETRY DESIGN

Besides the similarities, IGA has its particularities in comparison to FEM. The advantages the FEM have over the FEM are the geometrically exact and higher order continuous basis functions. In IGA analysis, no matter how coarse the mesh is created, no geometry information is lost. The geometrically exact property makes the method suitable for the analysis of problems which are sensitive to the geometry imperfections, such as buckling analysis in thin wall structures. It also gives a better analysis for the contact problem, where the contact region can be precisely modelled and analysed with NURBS. The latter property is meaningful for the solution of high order PDE, such as cahn-hilliard equation, which can be used in structural optimization [138]. It is a fourth order PDE, its solving is a real challenge in the traditional FEM. It has been solved easily by IGA [64]. It is noteworthy that the geometrical map in IGA is from the elements in parametric space to the physical space, it is confined within a patch, unlike the case in FEM where every physical element is a map from the same mother element in parametric space.

The basis functions used in IGA are non-interpolatory, which means the control points do not pass through the domain except those lie at the corner of the domain. As a result, the unknown fields values attached at each control point does not indicate the field value in that place. It makes the imposing of non-zero Dirichlet boundary condition more complicated than FEM, normally weak enforcement method are adopted [16, 135].

A thorough comparison with FEM method is shown in Table 2.1. It is reproduced from the paper [79].

Table 2.1: Comparison of finite element analysis and isogeometric analysis based on NURBS, table reproduced from [37].

Finite element analysis		Isogeometric analysis
Nodal points		Control points
Nodal variables		Control variables
Mesh		Knots
Basis interpolates nodal points and variables		Basis does not interpolate control points and variables
Approximate geometry		Exact geometry
Polynomial basis		NURBS basis
Gibbs phenomena		Variation diminishing
Subdomains		Patches
	Compact support	
	Partition of unity	
	Isoparametric concept	
	Affine covariance	
	Patch tests satisfied	

2.4 Summary

We adopt isogeometric shell elements for modelling the surface with shell properties for optimization. The background of isogeometric shell was introduced in this chapter. The isogeometric shell is a combination of traditional shell models and the isogeometric approximation method. We emphasized on the Kirchhoff-Love shell and Reissner-Mindlin shell models. We also gave a short introduction about the isogeometric framework and its foundation, the computer aided geometry design. The implementation of isogeometric shell formulations will be further detailed in the next chapter.

Chapter 3

Isogeometric shell structure analysis

We use isogeometric shell elements in this thesis to model the surfaces with shell properties. With the foundations on the shell models and the isogeometric analysis in the previous chapter, we will detail in this chapter the implementation of isogeometric Kirchhoff-Love shell and the Reissner-Mindlin shell.

IGA shell analysis is a combination of the shell formulation and the IGA approximation method. Until now, most of the traditional shell models' IGA versions can be found in the literatures. Kiendl et al. [86] proposed the IGA Kirchhoff-Love (KL) shell. It benefits from the higher continuous basis functions in IGA. Uhm and Youn [130] developed the IGA Reissner-Mindlin shell elements formulated with degenerated solid method. Benson et al. [20] implemented the IGA Reissner-Mindlin shell in Ls-dyna. He also proposed another two shell models [21, 22]. Hosseini et al. [73] and Bouclier et al. [28] proposed the IGA solid shell element. Echter et al. [52] proposed a hierarchic family of shell models. He gave both IGA Kirchhoff-Love shell and Reissner-Mindlin shell (5 and 7 DOFs) under the same theory framework. His Reissner-Mindlin shell element possesses the KL shell's rotation expression as well as a superposition of a difference vector to express the total fiber rotation. This scheme made the model intrinsically free of shear locking. Dornisch et al. [50] developed an exactly calculated fiber vectors IGA Reissner-Mindlin shell element and its multiple patches version [49], they are formulated with the geometrically exact formulation.

In this chapter, the focus are the Kirchhoff-Love shell and the Reissner-Mindlin shell. The former is a linearisation of the version in paper Kiendl et al. [86]. We propose a mixed grid isogeometric Reissner-Mindlin shell, both NURBS basis and Lagrange/Serendipity basis are adopted in the analysis.

3.1 Linear Kirchhoff-Love shell

In Kirchhoff-Love shells, the deformation of the shell is expressed by the displacements of the control points. The rotation is expressed by the translational displacement of the

3. ISOGEOMETRIC SHELL ANALYSIS

shell midsurface. As a result, it becomes a fourth order PDE, which needs at least C^1 continuous basis functions. This requirement is hard to fulfil in the traditional FEM, where C^0 basis functions are commonly used. However, this will not be a problem in IGA analysis. As has been stated in the previous chapter, the high order continuous basis functions used in CAGD, e.g. B-spline and NURBS basis functions, are easy to construct. The use of them successfully overcomes this difficulty. Kiendl et al. [86, 87] proposed the first isogeometric thin shell elements. Their model is suitable for non-linear analysis. The element of Benson et al. [21] is based on the same ideas, but it does not fully fulfil the Kirchhoff-Love assumptions, the normal vectors used in the proposed approach only make sense in the quadrature points instead of the entire domain. The focus in this chapter is the Kirchhoff-Love shell model.

3.1.1 Isogeometric Linear Kirchhoff-Love shell implementation

The model presented in this chapter is a linearisation of this model in paper Kiendl et al. [86]. The Kirchhoff-Love model has been introduced in the previous chapter. The strain components introduced in the previous chapter are nonlinear functional of \mathbf{u} . In the present work, we only consider the linear case, a linearisation with respect \mathbf{u} at $\mathbf{u} = \mathbf{0}$ is needed. That is

$$\begin{aligned}\delta\varepsilon_{\alpha\beta}^L &= \delta\varepsilon_{\alpha\beta}|_{\mathbf{u}=\mathbf{0}} \\ &= \frac{1}{2} (\delta\mathbf{u}_{,\alpha} \cdot \mathbf{A}_\beta + \delta\mathbf{u}_{,\beta} \cdot \mathbf{A}_\alpha)\end{aligned}\tag{3.1}$$

$$\begin{aligned}\delta\kappa_{\alpha\beta}^L &= \delta\kappa_{\alpha\beta}|_{\mathbf{u}=\mathbf{0}} \\ &= -[\delta(\mathbf{a}_{\alpha,\beta}) \cdot \mathbf{n}_3 + \mathbf{a}_{\alpha,\beta} \cdot \delta(\mathbf{n}_3)]|_{\mathbf{u}=\mathbf{0}} \\ &= -\delta\mathbf{u}_{,\alpha\beta} \cdot \mathbf{N}_3 + \frac{1}{\|\mathbf{A}_1 \times \mathbf{A}_2\|} [\delta\mathbf{u}_{,1} \cdot (\mathbf{A}_{\alpha,\beta} \times \mathbf{A}_2) + \delta\mathbf{u}_{,2} \cdot (\mathbf{A}_1 \times \mathbf{A}_{\alpha,\beta})] \\ &\quad + \frac{\mathbf{N}_3 \cdot \mathbf{A}_{\alpha,\beta}}{\|\mathbf{A}_1 \times \mathbf{A}_2\|} [\delta\mathbf{u}_{,1} \cdot (\mathbf{A}_2 \times \mathbf{N}_3) + \delta\mathbf{u}_{,2} \cdot (\mathbf{N}_3 \times \mathbf{A}_1)].\end{aligned}\tag{3.2}$$

Together with the material tensor components introduced in the previous chapter, the integral form control equation for small deformation Kirchhoff-Love shell can be obtained as

$$\int_{R_{KL}^0} \boldsymbol{\varepsilon}^T \mathbf{D} \delta\boldsymbol{\varepsilon} d\Omega + \frac{t^3}{12} \int_{R_{KL}^0} \boldsymbol{\kappa}^T \mathbf{D} \delta\boldsymbol{\kappa} d\Omega = \int_{R_{KL}^0} \rho \mathbf{b} \cdot \delta\mathbf{u} d\Omega + \int_{R_{KL}^0} \mathbf{t} \cdot \delta\mathbf{u} d\Omega.\tag{3.3}$$

The meaning of the notations have been stated in the previous chapter. As for the

IGA implementation aspect, both the deformed and undeformed shell midsurfaces are expressed with the bivariate NURBS surfaces,

$$\mathbf{R}_{KL}^0(\xi, \eta) = \sum_{i_j=1}^{mn} \hat{\mathbf{P}}_{i_j} \hat{R}_{i_j}(\xi, \eta). \quad (3.4)$$

$$\mathbf{r}_{KL}^0(\xi, \eta) = \sum_{i_j=1}^{mn} \hat{\mathbf{p}}_{i_j} \hat{R}_{i_j}(\xi, \eta). \quad (3.5)$$

As a result, the displacement \mathbf{u} will also be expressed by a NURBS surface as following

$$\mathbf{u}(\xi, \eta) = \sum_{i_j=1}^{mn} \hat{\mathbf{p}}_{i_j} \hat{R}_{i_j}(\xi, \eta). \quad (3.6)$$

Uttill now, all the components in equations (3.2) and (3.1) can be calculated, for example, the covariant base vector can be calculated as following,

$$\mathbf{A}_\alpha = \mathbf{R}_{KL}^0(\xi, \eta)_{,\alpha} = \sum_{i_j=1}^{mn} \hat{\mathbf{p}}_{i_j} \hat{R}_{i_j,\alpha}(\xi, \eta). \quad (3.7)$$

$$\mathbf{A}_{\alpha,\beta} = \mathbf{R}_{KL}^0(\xi, \eta)_{,\alpha\beta} = \sum_{i_j=1}^{mn} \hat{\mathbf{p}}_{i_j} \hat{R}_{i_j,\alpha\beta}(\xi, \eta). \quad (3.8)$$

The derivatives of \mathbf{u} can be expressed as

$$\mathbf{u}_{,\alpha} = \sum_{i_j=1}^{mn} \mathbf{u}_{i_j} \hat{R}_{i_j,\alpha}(\xi, \eta). \quad (3.9)$$

$$\mathbf{u}_{,\alpha\beta} = \sum_{i_j=1}^{mn} \mathbf{u}_{i_j} \hat{R}_{i_j,\alpha\beta}(\xi, \eta). \quad (3.10)$$

It can be seen that all the ingredients can be calculated with the operations on the NURBS basis functions. Substituting them into the control equation (3.3), we can obtain the final NURBS based linear Kirchhoff-Love IGA formulation. The elements in physical space and parametric space are shown in figure 3.1. It is noteworthy that the basis functions used here are at least of C^1 continuity, the polynomial order should be higher than two.

The final discrete equation for static analysis could be obtained as following

$$\mathbf{K}\mathbf{u} = \mathbf{F}, \quad (3.11)$$

$$K_{lm} = \frac{\partial \delta \Pi_{\text{int}}}{\partial \delta u_l \partial u_m}, F_l = \frac{\partial \delta \Pi_{\text{ext}}}{\partial \delta u_l}. \quad (3.12)$$

The boundary condition in IGA kirchhoff-Love shell needs more concerns due to two

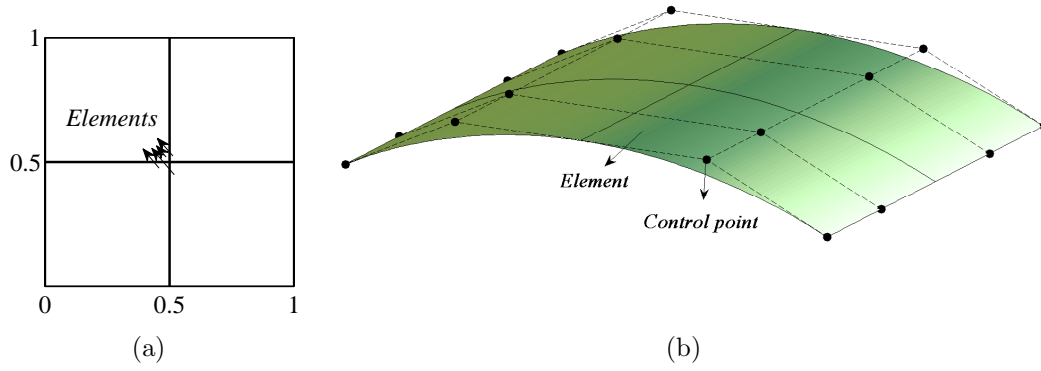


Figure 3.1: IGA Kirchhoff-Love shell elements in parametric space (a) and physical space (b).

facts. First of all, there is no rotational degrees of freedom in such shell model. Secondly, the basis functions are non-interpolatory. They all bring difficulties. The imposing of rotational boundary condition in IGA Kirchhoff-Love shell model should be approximated by the displacements of those control points near the boundaries, since there are only translational degrees of freedom for the control points of the shell midsurface. As for the translational boundary condition, it is exerted on the control points. However, lack of interpolatory property of the basis functions also makes the non-zero boundary condition hard to be exerted, as has been stated in the previous chapter, the weak imposing methods are usually used.

3.1.2 Shell benchmark problems

Shell obstacle course is frequently used in the test of various shell formulations. Nearly all the IGA shell formulations use all or one of them for the validation. We also use them here. We present their problem setup and material properties here. Those benchmark problems are all linear analysis case, Kiendl et al. [86] reported their results in their publications. We gave its linear analysis implementation. Here, we only give the result for one example. The main purpose is for the next subsection, we will use them to verify our Reissner-Mindlin shell formulation.

The shell obstacle course is composed of three problems: Scordelis-Lo roof problem, pinched cylinder problem and hemisphere problem. Their setups and material properties are shown in the figure 3.2, 3.3 and 3.4 respectively. The reference displacements at points A , B and C are 0.3024, 1.8248×10^{-5} and 0.0924 respectively [19]. Here, the reference value for point B , we adopt 1.85×10^{-5} that appeared in the IGA solid shell [28].

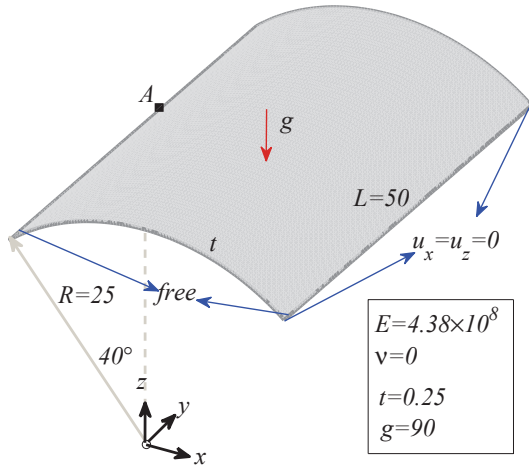


Figure 3.2: The scordelis-lo roof problem setup.

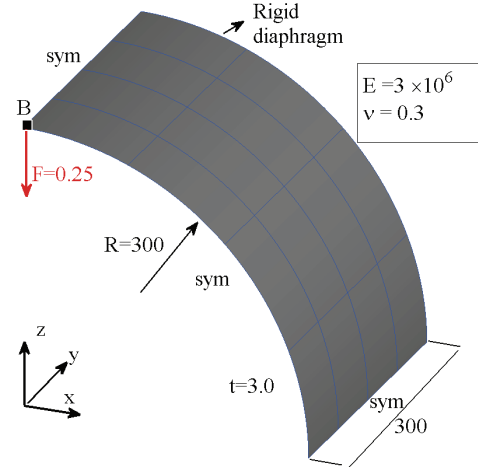


Figure 3.3: The pinched cylinder problem setup.

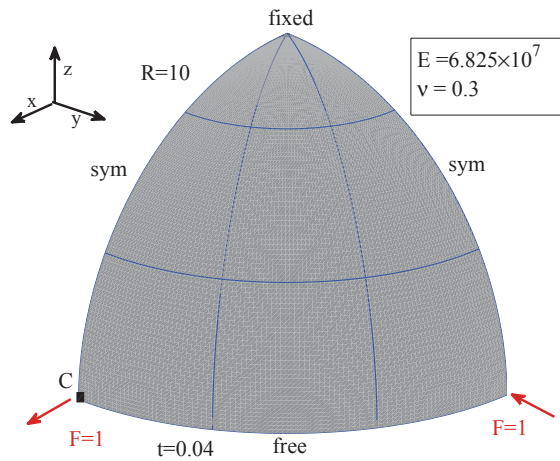


Figure 3.4: The hemisphere shell problem setup.

3. ISOGEOMETRIC SHELL ANALYSIS

The static analysis result

The Scordelis-Lo roof results are presented here, the problem setup has been presented in 3.2. The elements are uniformly created. The elements per edges are 2^i , $i = 0, 1, 2, 3, 4$. The displacement at point A is presented in figure 3.5 with different order NURBS basis functions. They all converge to the same value.

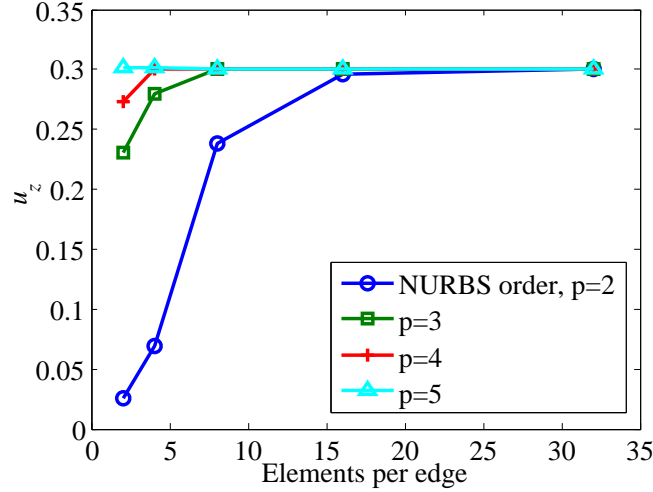


Figure 3.5: The u_z displacement at point A with different NURBS order IGA Kirchhoff-Love shell.

Figure 3.6 and 3.7 show the contour plot of u_z displacement and the deformed shape (with a scaling factor 10) respectively. They are obtained with NURBS order 3, the elements per edge are 32.

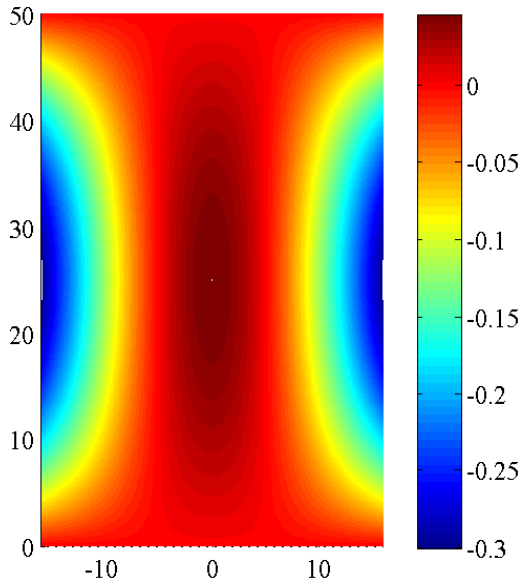


Figure 3.6: The u_z contour plot.

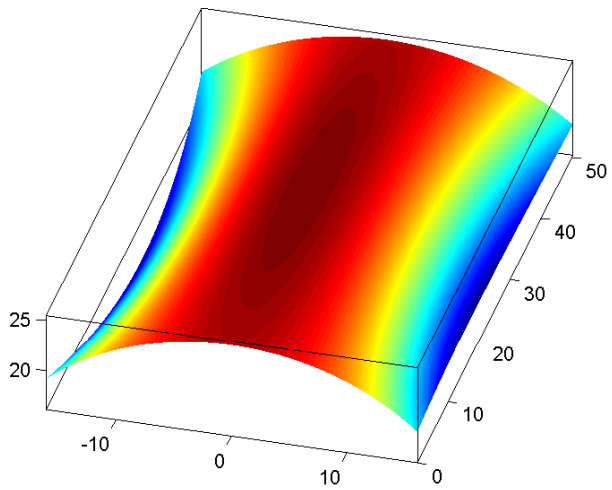


Figure 3.7: The deformed structure with a scaling factor 10.

The modal analysis result

The problem setup is the same with the Scordelis-Lo roof problem, except the boundary condition, the endings of the roof are fully constrained here. The quadratic NURBS basis functions are used, the structure is uniformly meshed with 24 elements on each edge. The results are also compared with these from the FEM method. Figure 3.8 show the result. They are comparable with each other.

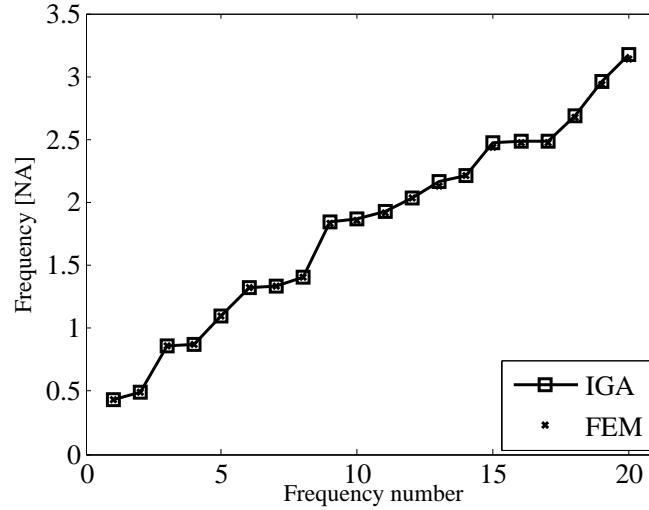


Figure 3.8: The first 20 frequencies obtained with IGA and FEM, the quadratic NURBS are used.

3.2 Linear degenerated solid Reissner-Mindlin shell

The Kirchhoff-Love shell model does not take into account the transverse shear effect, while the Reissner-Mindlin shell model does. We will formulate the Reissner-Mindlin shell model in the IGA framework. The degenerated shell approach is widely used in shell analysis for its simplicity. The idea is to discretize the shell into solid element, and then use linear shape functions in the thickness direction. After simplifications, the geometry of the shell will be expressed with a parametric mid-surface and an interpolated fiber vector which indicates the thickness direction. Correspondingly, the kinematics of the geometry will be expressed by the translations of mid-surface nodes and the rotations of the fiber vectors. The detailed procedures can be seen in Hughes [77], Zhu et al. [139]. In this section, we briefly review standard results to introduce the notations and introduce some changes that are suited for detailing our approach. The readers are encouraged to read [77, 139] for further details.

The geometry of the shell after simplification can be expressed using the following

3. ISOGEOMETRIC SHELL ANALYSIS

equation

$$\mathbf{x} = \sum_A N_A(\varepsilon, \eta) \left(\mathbf{x}_A + \frac{h_A}{2} \varsigma \mathbf{y}_A \right). \quad (3.13)$$

Here, N_A are the basis functions associated to node A, h_A is the thickness at node A, \mathbf{y}_A is the unite fiber vector at node A which indicates the thickness direction.

The kinematics of the shell is expressed as follows:

$$\mathbf{u} = \sum_A N_A(\varepsilon, \eta) \left(\mathbf{u}_A + \frac{h_A}{2} \varsigma \mathbf{y}'_A \right) \quad (3.14)$$

where \mathbf{u}_A is the translation of the mid-surface node A and \mathbf{y}'_A is the difference vector which indicates fiber rotation at node A. With the assumptions of inextensibility of the fiber vectors and small deformation, \mathbf{y}'_A can be approximated as $\mathbf{w}_A \times \mathbf{y}_A$. Equation (3.14) can be rewritten as,

$$\mathbf{u} = \sum_A N_A(\varepsilon, \eta) \left(\mathbf{u}_A + \frac{h_A}{2} \varsigma \mathbf{w}_A \times \mathbf{y}_A \right), \quad (3.15)$$

where \mathbf{w}_A is a three dimensional vector which describes the rotation angles along three global coordinate axis at node A. If we continue our deduction without any treatment, we will obtain a shell model with six degrees of freedom at each node. Further treatments will be needed to eliminate the drilling rotations along the fiber vectors itself, as there is no rotational stiffness corresponding to it. If \mathbf{w}_A is expressed in a nodal coordinate system, $\mathbf{w}_A = \theta_{A1} \mathbf{e}_{A1} + \theta_{A2} \mathbf{e}_{A2} + \theta_{A3} \mathbf{e}_{A3}$, \mathbf{e}_{A3} is equal to \mathbf{y}_A , \mathbf{e}_{A1} and \mathbf{e}_{A2} are orthogonal to \mathbf{y}_A , the following expression is finally obtained,

$$\mathbf{u} = \sum_A N_A(\varepsilon, \eta) \left(\mathbf{u}_A + \frac{h_A}{2} \varsigma (-\theta_{A1} \mathbf{e}_{A2} + \theta_{A2} \mathbf{e}_{A1}) \right). \quad (3.16)$$

The number of nodal rotation parameters is reduced to two and the commonly used five degrees of freedom Reissner-Mindlin shell formulation is obtained. This paper discusses the linear small deformation circumstances, therefore the linear strain tensor is used:

$$\varepsilon = \frac{1}{2} (\nabla \mathbf{u} + \nabla \mathbf{u}^T). \quad (3.17)$$

The strain energy is classically obtained using the following expression:

$$W_{\text{int}} = \frac{1}{2} \int_{\Omega} \varepsilon : \mathbf{C} : \varepsilon \, d\Omega. \quad (3.18)$$

The stiffness matrix is finally obtained thank to the following expression,

$$K_{rs} = \frac{\partial W_{\text{int}}}{\partial u_r \partial u_s}. \quad (3.19)$$

In order to modify the material tensor to reach the zero normal stress condition and calculate the integrant in equation (3.18), the material tensor will be expanded in a so-called lamina coordinate system, so as the strain tensor. One way to do so is to follow Hughes [77]:

$$\mathbf{e}_\varepsilon = \frac{\mathbf{x}_{,\varepsilon}}{|\mathbf{x}_{,\eta}|}, \quad (3.20)$$

$$\mathbf{e}_\eta = \frac{\mathbf{x}_{,\eta}}{|\mathbf{x}_{,\eta}|}, \quad (3.21)$$

$$\mathbf{e}_3^l = \frac{\mathbf{e}_\varepsilon \times \mathbf{e}_\eta}{|\mathbf{e}_\varepsilon \times \mathbf{e}_\eta|}, \quad (3.22)$$

$$\mathbf{e}_a = \frac{\mathbf{e}_\varepsilon + \mathbf{e}_\eta}{|\mathbf{e}_\varepsilon + \mathbf{e}_\eta|}, \quad (3.23)$$

$$\mathbf{e}_\beta = \frac{\mathbf{e}_3^l \times \mathbf{e}_a}{|\mathbf{e}_3^l \times \mathbf{e}_a|}. \quad (3.24)$$

The lamina coordinate axis will therefore be

$$\mathbf{e}_1^l = \frac{\sqrt{2}}{2} (\mathbf{e}_a - \mathbf{e}_\beta), \quad (3.25)$$

$$\mathbf{e}_2^l = \frac{\sqrt{2}}{2} (\mathbf{e}_a + \mathbf{e}_\beta). \quad (3.26)$$

And the transformation matrix from the global coordinate system to the local one will be

$$\mathbf{q} = \begin{bmatrix} \mathbf{e}_1^l & \mathbf{e}_2^l & \mathbf{e}_3^l \end{bmatrix}. \quad (3.27)$$

The strain tensor $\boldsymbol{\varepsilon}$ will be expressed at each quadrature point lamina coordinate system. Adopting Voigt notation, the strain vector $\tilde{\boldsymbol{\varepsilon}}$ is introduced and allows us to obtain the strain-displacement matrix \mathbf{B} as following:

$$\tilde{\boldsymbol{\varepsilon}} = [\varepsilon_{11} \quad \varepsilon_{22} \quad 2\varepsilon_{12} \quad 2\varepsilon_{23} \quad 2\varepsilon_{13}]^T, \quad (3.28)$$

$$\tilde{\boldsymbol{\varepsilon}} = [\mathbf{B}^u \quad \mathbf{B}^r] \begin{bmatrix} \mathbf{u} & \theta \end{bmatrix}^T, \quad (3.29)$$

$$\mathbf{B}^u = [\mathbf{B}_1^u \quad \mathbf{B}_2^u \quad \mathbf{B}_3^u], \quad (3.30)$$

$$\mathbf{B}^r = [\mathbf{B}_1^r \quad \mathbf{B}_2^r], \quad (3.31)$$

3. ISOGEOMETRIC SHELL ANALYSIS

$$\mathbf{B}_m^u = \begin{bmatrix} q_{m1} \frac{\partial N_1}{\partial x} & \cdots & q_{m1} \frac{\partial N_n}{\partial x} \\ q_{m2} \frac{\partial N_1}{\partial y} & \cdots & q_{m2} \frac{\partial N_n}{\partial y} \\ q_{m1} \frac{\partial N_1}{\partial y} + q_{m2} \frac{\partial N_1}{\partial x} & \cdots & q_{m1} \frac{\partial N_n}{\partial y} + q_{m2} \frac{\partial N_n}{\partial x} \\ q_{m3} \frac{\partial N_1}{\partial y} + q_{m2} \frac{\partial N_1}{\partial z} & \cdots & q_{m3} \frac{\partial N_n}{\partial y} + q_{m2} \frac{\partial N_n}{\partial z} \\ q_{m3} \frac{\partial N_1}{\partial x} + q_{m1} \frac{\partial N_1}{\partial z} & \cdots & q_{m3} \frac{\partial N_n}{\partial x} + q_{m1} \frac{\partial N_n}{\partial z} \end{bmatrix}, \quad (3.32)$$

$$\mathbf{B}_1^r = \frac{h}{2} \varsigma \begin{bmatrix} [-\mathbf{q}\mathbf{e}_{12}]_1 \frac{\partial N_1}{\partial x} & \cdots & [-\mathbf{q}\mathbf{e}_{n2}]_1 \frac{\partial N_n}{\partial x} \\ [-\mathbf{q}\mathbf{e}_{12}]_2 \frac{\partial N_1}{\partial y} & \cdots & [-\mathbf{q}\mathbf{e}_{n2}]_2 \frac{\partial N_n}{\partial y} \\ [-\mathbf{q}\mathbf{e}_{12}]_2 \frac{\partial N_1}{\partial x} + [-\mathbf{q}\mathbf{e}_{12}]_1 \frac{\partial N_1}{\partial y} & \cdots & [-\mathbf{q}\mathbf{e}_{n2}]_2 \frac{\partial N_n}{\partial x} + [-\mathbf{q}\mathbf{e}_{n2}]_1 \frac{\partial N_n}{\partial y} \\ [-\mathbf{q}\mathbf{e}_{12}]_3 \frac{\partial N_1}{\partial y} + [-\mathbf{q}\mathbf{e}_{12}]_2 \frac{\partial N_1}{\partial z} & \cdots & [-\mathbf{q}\mathbf{e}_{n2}]_3 \frac{\partial N_n}{\partial y} + [-\mathbf{q}\mathbf{e}_{n2}]_2 \frac{\partial N_n}{\partial z} \\ [-\mathbf{q}\mathbf{e}_{12}]_3 \frac{\partial N_1}{\partial x} + [-\mathbf{q}\mathbf{e}_{12}]_1 \frac{\partial N_1}{\partial z} & \cdots & [-\mathbf{q}\mathbf{e}_{n2}]_3 \frac{\partial N_n}{\partial x} + [-\mathbf{q}\mathbf{e}_{n2}]_1 \frac{\partial N_n}{\partial z} \end{bmatrix}, \quad (3.33)$$

$$\mathbf{B}_2^r = \frac{h}{2} \varsigma \begin{bmatrix} [\mathbf{q}\mathbf{e}_{11}]_1 \frac{\partial N_1}{\partial x} & \cdots & [\mathbf{q}\mathbf{e}_{n1}]_1 \frac{\partial N_n}{\partial x} \\ [\mathbf{q}\mathbf{e}_{11}]_2 \frac{\partial N_1}{\partial y} & \cdots & [\mathbf{q}\mathbf{e}_{n1}]_2 \frac{\partial N_n}{\partial y} \\ [\mathbf{q}\mathbf{e}_{11}]_2 \frac{\partial N_1}{\partial x} + [\mathbf{q}\mathbf{e}_{11}]_1 \frac{\partial N_1}{\partial y} & \cdots & [\mathbf{q}\mathbf{e}_{n1}]_2 \frac{\partial N_n}{\partial x} + [\mathbf{q}\mathbf{e}_{n1}]_1 \frac{\partial N_n}{\partial y} \\ [\mathbf{q}\mathbf{e}_{11}]_3 \frac{\partial N_1}{\partial y} + [\mathbf{q}\mathbf{e}_{11}]_2 \frac{\partial N_1}{\partial z} & \cdots & [\mathbf{q}\mathbf{e}_{n1}]_3 \frac{\partial N_n}{\partial y} + [\mathbf{q}\mathbf{e}_{n1}]_2 \frac{\partial N_n}{\partial z} \\ [\mathbf{q}\mathbf{e}_{11}]_3 \frac{\partial N_1}{\partial x} + [\mathbf{q}\mathbf{e}_{11}]_1 \frac{\partial N_1}{\partial z} & \cdots & [\mathbf{q}\mathbf{e}_{n1}]_3 \frac{\partial N_n}{\partial x} + [\mathbf{q}\mathbf{e}_{n1}]_1 \frac{\partial N_n}{\partial z} \end{bmatrix}. \quad (3.34)$$

Here, h is the thickness of the shell. If the shell thickness is varying, it should appear as $h_A N_A$ in the content of the matrix in equation (3.33) and (3.34). \mathbf{q} is the transformation matrix at a given quadrature point. \mathbf{e}_{Ai} is the i th local coordinate axis at the A th node. n is the number of basis functions whose value are non-zero at a given quadrature point. The calculation of the basis functions derivatives with respect to global coordinate can be obtained as in Hughes [77], Zhu et al. [139].

Finally, the contribution of a given quadrature point to the stiffness matrix is

$$\mathbf{K}_q = \mathbf{B}_q^T \mathbf{D} \mathbf{B}_q, \quad (3.35)$$

where \mathbf{D} is the modified material matrix, the definition was detailed the previous chapter. Multiplying the above contribution with its corresponding quadrature weight and then sum up on all quadrature points, we finally obtain the element stiffness matrix. The Reissner-Mindlin shell model enables the use of C^0 continuous basis functions, which are easy to be obtained in the traditional FEM framework.

3.3 Mixed grid Reissner-Mindlin formulation: NURBS and Lagrange basis functions

We propose a new isogeometric Reissner-Mindlin degenerated shell element for linear analysis. It is based on the mixed use of NURBS and Lagrange basis functions in the same domain. The mid-surface of the shell is represented and discretized using NURBS and the directors of the shell are discretized using Lagrange polynomials. The interpolatory property of Lagrange polynomials gives a natural choice of fiber vectors thus removes the difficulties in the definition of directors that is seen in most isogeometric Reissner-Mindlin shell elements. The NURBS representation of the mid-surface allows us to maintain the exact geometry representation characteristic of the isogeometric approach. The independent expressions of displacements and rotations also give users the possibility to use different numbers of degrees of freedom in an element for both kinematic variables. Several numerical examples show that our method is simple, robust and efficient.

The definition of fiber vectors (directors) is an important problem specific in IGA Reissner-Mindlin shell analysis. Due to the non-interpolatory nature of the NURBS basis functions, there is no natural way to define “nodal” fiber vectors in IGA. Uhm and Youn [130] obtained fiber vectors using the nearest projection of the control points onto the NURBS surface. The procedure consists in finding the control points nearest corresponding points on the surface and then define the corresponding control point director as the normal vector at those projected points. Dornisch et al. [50] obtained fiber vectors by solving a linear equation in order to make the axis of local coordinate systems in the quadrature points exactly equal with those obtained by a NURBS interpolation. It should be noted that either the nearest point projection or forming/solving the equation in the latter method will cost additional computer resources. There are also requirements about the number of quadrature points in the method of Dornisch et al. [50].

From our point of view, the fiber vectors can be viewed as another interpolated field whose reference points are fiber vector nodes. The difficulty encountered in the above shell formulations may be due to the use of NURBS in the expression of the director field, that makes the users spend additional computational effort to find these director points which can give better surface normal interpolation accuracy. We circumvent this problem by replacing NURBS with Lagrange or Serendipity basis functions for the expression of the director field. The NURBS representation of the shell mid-surface is kept unchanged. As a result, the movements of the mid-surface will be expressed with NURBS basis functions and the rotations of the fibers will be expressed with Lagrange basis functions. This also enables the users to use different numbers of degrees of freedoms for displacements and rotations in a single element. Another advantage is that the rotational boundary conditions can be easily applied.

3. ISOGEOMETRIC SHELL ANALYSIS

3.3.1 Formulations

IGA uses the basis functions which are used in computer graphics and animation for analysis. Let's repeat the bivariate NURBS basis function here:

$$R_{i,j}^{p,q} = \frac{N_i^p(\xi) N_j^q(\eta) w_{ij}}{\sum_{k=1}^n \sum_{l=1}^m N_k^p(\xi) N_l^q(\eta) w_{kl}}, \quad (3.36)$$

Introducing the basis functions of equation (3.36) into the shell model of the previous section, the isogeometric degenerated shell model can be devised. The starting point we consider here, as compared to what is done in FEM degenerated shells, is the definition of fiber vectors. Going back to the geometric description of the shell in equation (3.13) and considering a uniform shell, equation (3.13) can be rewritten as equation (3.37) and divided into two parts: the first one given in equation (3.38) is for the description of the mid-surface and the second one given in equation (3.39) is for the description of the director vectors:

$$\mathbf{x} = \mathbf{s} + \mathbf{v}, \quad (3.37)$$

$$\mathbf{s} = \sum_A N_A(\varepsilon, \eta) \mathbf{x}_A, \quad (3.38)$$

$$\mathbf{v} = \frac{h}{2} \zeta \sum_A N_A(\varepsilon, \eta) \mathbf{y}_A. \quad (3.39)$$

The entire geometry can be viewed as the superposition of the mid-surface and the director field, see figure 3.9.

In traditional FEM, the fiber vectors \mathbf{y}_A at each node can be naturally chosen as the normal of the shell at this node. The directors within the element can be found using equation (3.39). However, the control points in IGA do not belong to the represented geometry (except for piecewise linear NURBS which are identical to piecewise linear finite elements). As a consequence, there is no natural normal attached to the control points. Many methods have been proposed to fix this and define fiber vector at the node, as presented in the introduction. These methods need additional computational resources and programming effort. Another problem that appears using these approaches is that the approximation of the director vectors becomes worse when the polynomial order of the NURBS basis functions increases, see Figure 2 of Dornisch et al. [50]. Our approach to circumvent this is to use different representation for the thickness vectors \mathbf{v} and the shell mid-surface \mathbf{s} . Figure 3.9 shows the Lagrange interpolation of the shell directors and its superposition with the NURBS representation of the mid-surface to form the shape of the 3D shell. Equation (3.38) is used to discretize \mathbf{s} , while equation (3.40) is used to discretize \mathbf{v} :

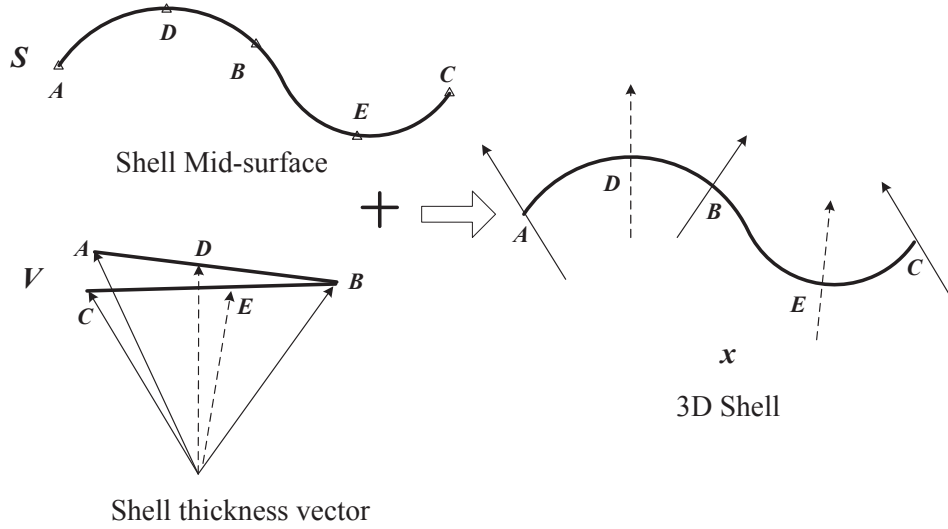


Figure 3.9: An example of 3D shell shape description with NURBS basis and Lagrange basis. \mathbf{s} is expressed with NURBS basis. shell director \mathbf{v} with Linear Lagrange interpolation, basis points are the normal at points A , B and C . Normals of points D and E are obtained by interpolation.

$$\mathbf{v} = \frac{h}{2} \sum_B \hat{N}_B(\varepsilon, \eta) \mathbf{y}_B, \quad (3.40)$$

where \hat{N}_B is the Lagrange basis. The “nodal” coordinates in parameter space are uniformly distributed in each element interval. There will exist $p_l + 1$ basis points for p_l order Lagrange basis functions, the first and end points will be located in the element interval’s endpoints. Their corresponding normal vectors in the NURBS mid-surface will be the basis \mathbf{y}_B of equation (3.40). Their lamina coordinate systems will be used as nodal coordinate systems. An illustration of the mixed use of quadratic NURBS and quadratic Lagrange basis functions is depicted in figure 3.10.

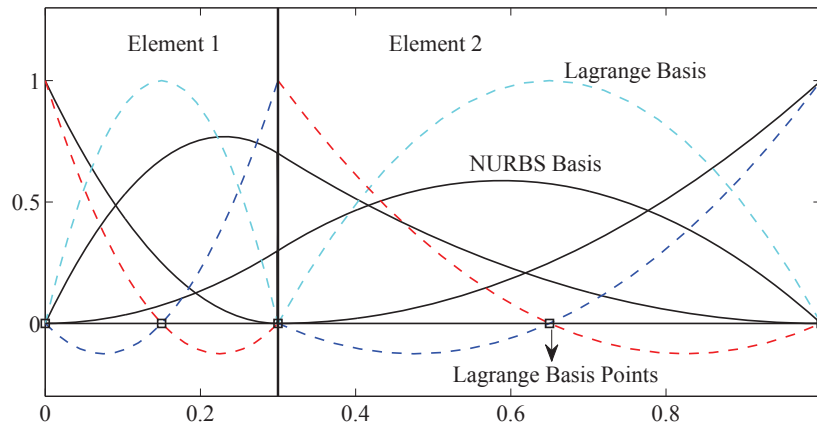


Figure 3.10: An example of 2 order Lagrange (slash lines), 2 order NURBS basis functions and the Lagrange basis points positions (squares) in IGA elements $[0; 0.3]$ and $[0.3; 1]$.

3. ISOGEOMETRIC SHELL ANALYSIS

It should be noted that the Lagrange basis points are uniformly distributed in each IGA interval. Consequently, the value of the Lagrange basis function and their derivatives only need to be evaluated once in the isoparametric interval $[-1; 1]$. Then, to obtain the derivatives in an IGA interval of length l , multiplying them by $2/l$ allows us to obtain the correct value. The value of the Lagrange basis functions is kept unchanged in every interval. A similar approach can be used when implementing Gauss quadrature. From the above procedures, it can be seen that although we introduce additional Lagrange basis functions in our method, nearly no time and computational effort is spent on their evaluation. This is quite different with using a fully isogeometric approach, as the basis functions are very different when comparing all the elements of the considered mesh.

Deriving the previous equations, the approximation of the deformation is also obtained using a combination of NURBS and Lagrange basis functions. The displacement of the shell given in equation (3.14) can be rewritten as:

$$\mathbf{u} = \sum_A N_A(\varepsilon, \eta) \mathbf{u}_A + \frac{h}{2} \sum_B \hat{N}_B(\varepsilon, \eta) \mathbf{y}_B. \quad (3.41)$$

Following the derivation of the equation given in section 2.1, one can easily see that the expressions given in equations (3.32) to (3.34) are unchanged as long as the appropriate basis functions are used. That is the NURBS basis functions N are used in equation (3.32) and the Lagrange basis functions \hat{N} are used in equations (3.33) and (3.34). One can notice in the proposed approach that the concept of nodal degrees of freedom is not relevant as translational and rotational degrees of freedom are not associated to the same geometric points. In an isogeometric element, if we use degree p_l Lagrange basis functions and degree $p \times q$ NURBS basis functions, there will be $3(p+1)(q+1)$ translationnal degrees of freedom and $2(p_l+1)^2$ rotational degrees of freedom. K Gauss quadrature points will be used with $K = \text{maximum}(p, q, p_l) + 1$ in each parametric direction.

3.3.2 Numerical examples

Three benchmark problems from shell obstacle courses of Belytschko et al. [19] and one double curved free form surface example taken from Dornisch et al. [50] are used here to validate our method and compare it with other isogeometric shell elements. In all the examples, we considered NURBS basis functions of degree 2 to 5 and Lagrange basis functions of degree 2 and 3. Increasing the degree of the Lagange basis function does not improve the results when considering NUBRS up to degree 5 as we will see in the sequel. In all cases, we use regular meshes with $\{2, 4, 8, 16, 32\}$ elements per edges.

Scordelis-Lo roof problem

The problem setup and its material properties can be seen in figure 3.2. A gravity load $g = 90$ is applied to the model. The quantity of interest here is the vertical displacement u_z at point A. The converged value is -0.301969 and is attained with with 70×70 elements mesh quartic NURBS ($P_N = 4$) and cubic Lagrange ($P_L = 3$). It is comparable with the reference value -0.3020247 obtained by Dornisch et al. [50] using isogeometric Reissner-Mindlin shells with exactly calculated directors.

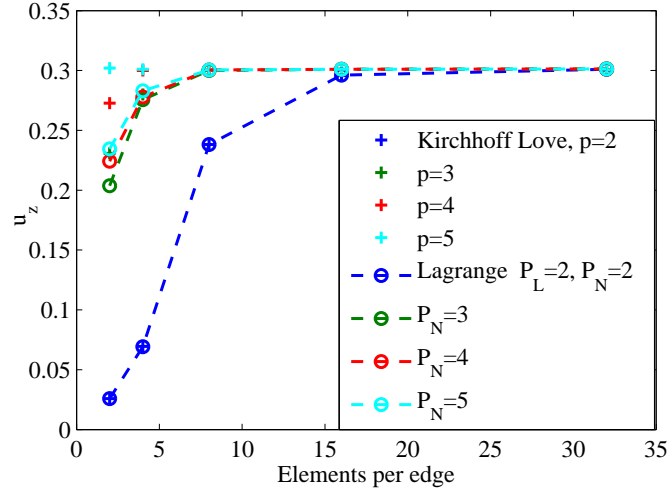


Figure 3.11: Scordelis-Lo roof, u_z vs number of elements per edges with quadratic Lagrange basis ($P_L = 2$) and various NURBS order.

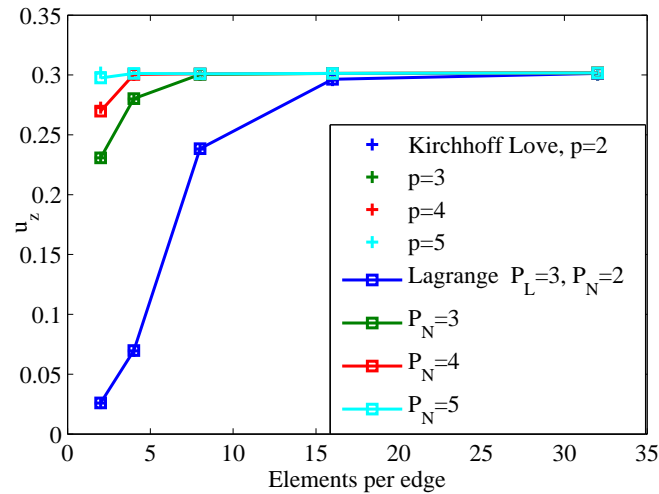


Figure 3.12: Scordelis-Lo roof, u_z vs number of elements per edges with cubic Lagrange basis ($P_L = 3$) and various NURBS order.

Figure 3.11 and 3.12 show the results with h refinement with various NURBS orders. Figure 3.11 show the results obtained using quadratic Lagrange basis functions. For quadratic NURBS $P_N=2$ the curves coincide with the results obtained with quadratic

3. ISOGEOMETRIC SHELL ANALYSIS

NURBS Kirchhoff-Love (KL) shells (developed by Kiendl et al. [86]). For cubic NURBS $P_N=3$ the curve approaches the results obtained with cubic NURBS KL shells. For higher order NURBS ($P_N = 4, 5$) the results are not comparable with their corresponding KL shell results, but they are better than the ones obtained with $P_N=2, 3$. Figure 3.12 shows the results with the same NURBS polynomial order but using cubic Lagrange basis functions. All the curves coincides with those obtained using KL shells.

Pinched cylinder problem

Figure 3.3 depicts the pinched cylinder problem setup and its material properties. Due to symmetry only one eighth of the system is modeled and sketched. This example has been used by Dornisch et al. [50] to compare their exactly calculated director IGA shell with the Kirchhoff-Love shell of Kiendl et al. [86] and the isogeometric Reissner-Mindlin shell of Benson et al. [20]. The converged solution for the vertical displacement at point B is 1.85371×10^{-5} with 32×32 elements $P_N = 5$ and $P_L = 3$. It is slightly different with the converged value 1.8248×10^{-5} obtained by Dornisch et al. [50], but it is similar to the one obtained by Bouclier et al. [28] using a mesh of 32×32 IGA solid shell elements (1.85×10^{-5}).

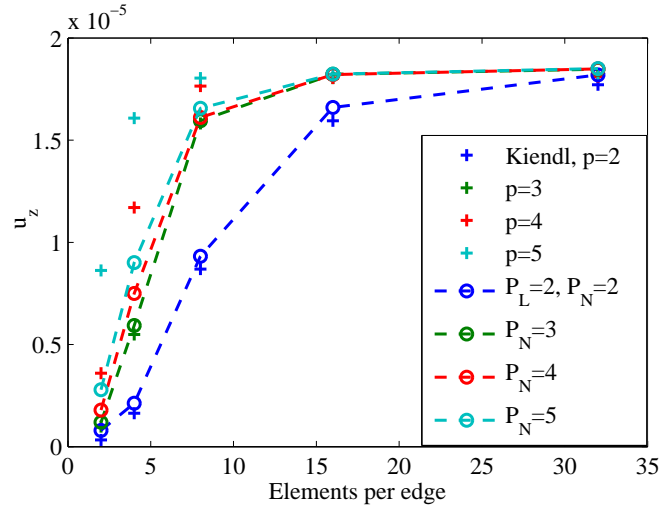


Figure 3.13: Pinched Cylinder, u_z vs number of elements per edges with quadratic Lagrange basis ($P_L = 2$) and various NURBS order.

Figure 3.13 and 3.14 depict the results obtained with h refinement with various NURBS orders. A similar behavior as for the previous example is observed. Figure 3.13 depicts the results obtained with quadratic Lagrange basis functions. The results of $P_N=2$ and 3 are comparable with these from KL shell. The results of $P_N=4$ and 5 are not comparable with these from KL shell, but they are better than $P_N=2$ and 3. Figure 3.14 shows the results obtained with cubic Lagrange basis functions. The results of $P_N=2 - 4$ are closer to the converged line than these obtained by KL shell at the same mesh size. The result

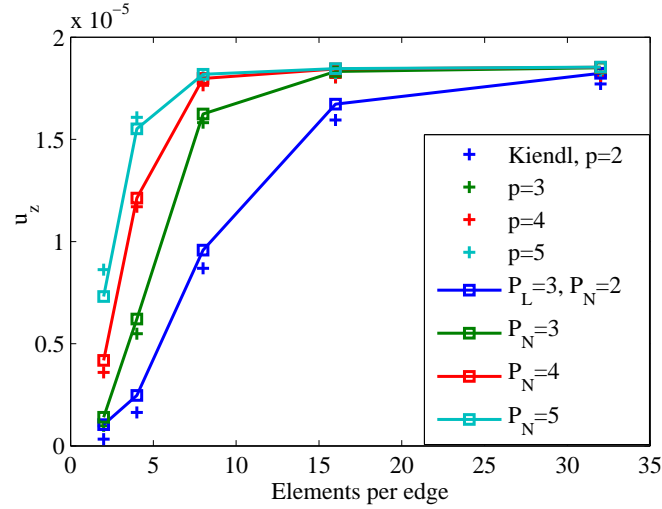


Figure 3.14: Pinched Cylinder, u_z vs number of elements per edges with cubic Lagrange basis ($P_L = 3$) and various NURBS order.

of $P_N=5$ approaches the one obtained with KL shell. A similar behavior when comparing the thick shell elements of Benson et al. [20], Dornisch et al. [50] with KL shells results can be seen. Consequently, it can be observed that our approach leads to comparable results with these two alternative Reissner-Mindlin isogeometric shells. Figure 3.15 shows a direct comparison between our results and those from Benson et al. [20], Dornisch et al. [50]. All the results are normalized with 1.83×10^{-5} . It can be seen clearly that for order 2 to 4, at the same mesh size, our results are closer to the reference line than the results obtained with two methods for this particular example.

Hemisphere shell problem

Figure 3.4 shows the hemisphere problem setup and its material properties. The quantity of interest is the horizontal displacement u_x at point C. The converged solution is 0.0925 with 32×32 elements, $P_N = 5$ and $P_L = 3$ which is identical to the one found in the literature. Figure 3.16 and 3.17 show the convergence of the horizontal displacement at point C versus number of elements per edges using h refinement. The general behavior of our approach that was seen in the previous examples is again observed here.

Double curved free form surface problem

This last example was designed by Dornisch et al. [50] to test their exactly calculated director IGA Reissner-Mindlin shell. Figure 3.18 shows the problem setup and material properties. The initial geometry description contains 3×3 uniformly divided cubic elements. The quantity of interest is the horizontal displacement u_y at point D, and the reference value u_s is 1.02786 with 180×180 NURBS elements with $p = 6$ as reported in Dornisch et al. [50]. We obtain 1.02529 as a converged value with 48×48 elements

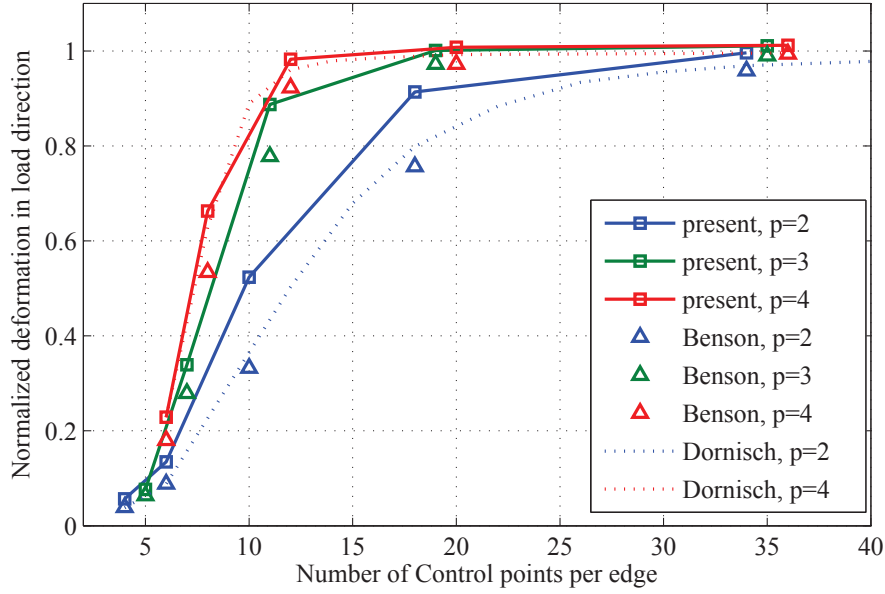


Figure 3.15: Pinched Cylinder, comparison of our approach with the one of Benson et al. [20] and [50]. Present approach: $p = 2$ indicates ($P_N = 2$, $P_L = 2$) and $p = 3$ ($P_N = 3$, $P_L = 3$), $p = 4$ ($P_N = 4$, $P_L = 3$)

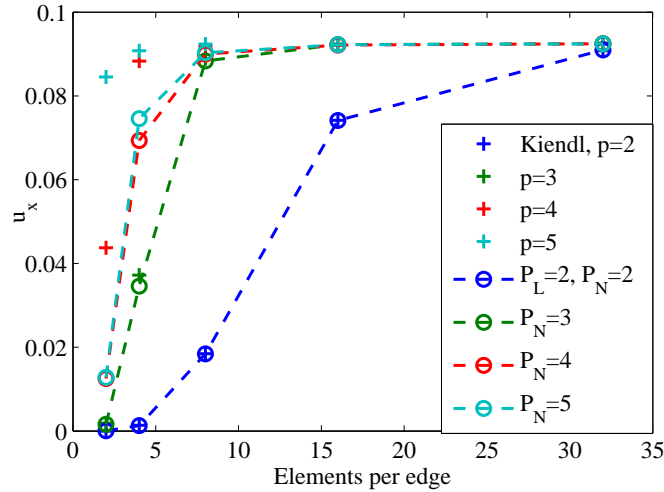


Figure 3.16: Hemisphere shell, u_x vs number of elements per edges with quadratic Lagrange basis ($P_L = 2$) and various NURBS order.

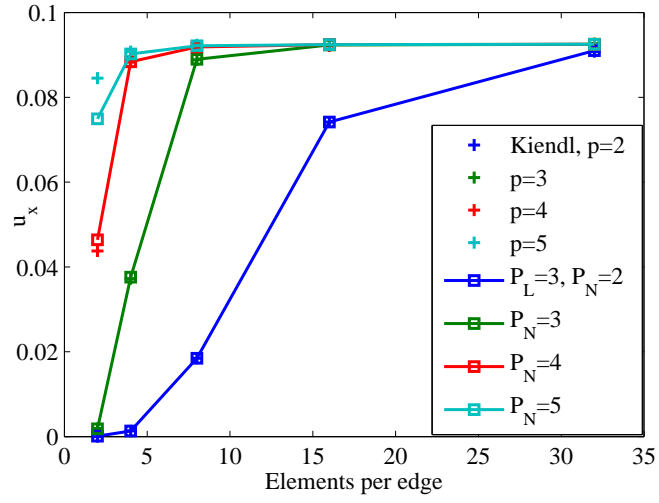


Figure 3.17: Hemisphere shell, u_x vs number of elements per edges with cubic Lagrange basis ($P_L = 3$) and various NURBS order.

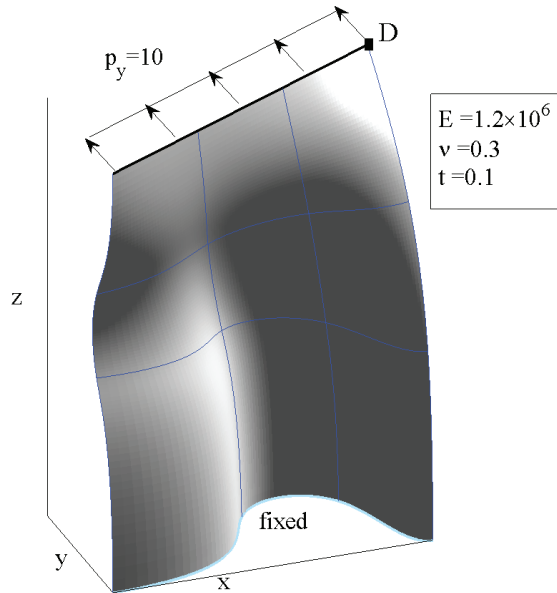


Figure 3.18: Double curved free form surface problem setup. Geometry data obtained from Dornisch et al. [50].

3. ISOGEOMETRIC SHELL ANALYSIS

$P_N = 5$ and $P_L = 3$.

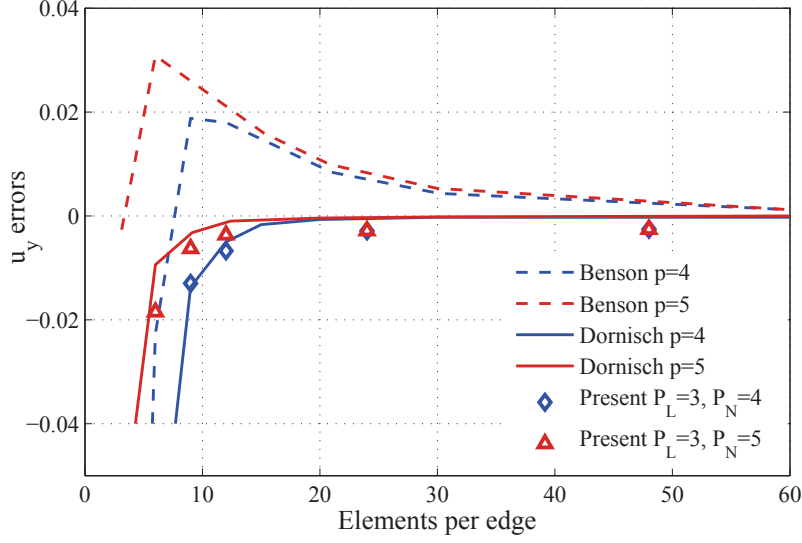


Figure 3.19: Double curved free surface, u_y variation with respect to the reference value ($u_y = 1.02786$) versus number of elements per edges. Results with alternative methods are taken from Dornisch et al. [50].

Figure 3.19 shows the u_y error variation around the reference value vs number of elements per edges with refined meshes obtained with h refinement. Our results are compared with the elements of Benson et al. [20], Dornisch et al. [50]. It can be seen that our results are not comparable with the ones obtained by Dornisch et al. [50], but they both approach the solution from the stiff side whereas the results obtained by Benson et al. [20] approach it from the soft side. It should be noticed that we used cubic Lagrange basis functions to express the rotations for $P_N = 4$ and 5. This implies at the element level that there will be 32 rotational degrees of freedom in our method versus 50 ($p = 4$) and 72 ($p = 5$) with the standard methods.

3.3.3 Discussions

The results of different combinations of NURBS order and Lagrange order basis functions formulations all converge correctly. The differences lie in their convergence rates. This indicates the applicability of the independent formulation of the displacements and rotations in IGA shell elements. There can be different numbers of rotational and translational degrees of freedom in an element.

Figure 3.20 depicts an empirical estimation of the convergence rate performances of P_N & P_L combinations. $P_L > P_N$, the results will be the same with these of the same order P_N . $P_L = 1$ and $P_N > 3$, the results nearly the same with $P_L = 1$ and $P_N = 3$, thus inefficient. The red line we marked as “Good Performance” means that their results nearly the same with the P_N order NURBS Kirchhoff-Love shell. Thus, we suggest users

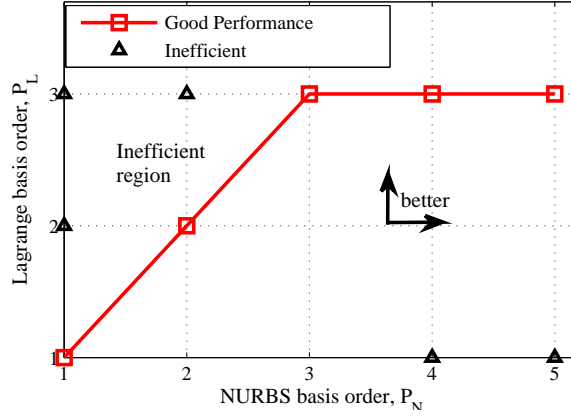


Figure 3.20: Combination of NURBS basis orders and Lagrange basis orders.

to use these combinations. In other region, when increase the P_N or P_L , the results (with the same numbers of elements) will become better. For instance, $P_L = 2$ $P_N = 3$ will better than $P_L = 2$ $P_N = 2$ and $P_L = 3$ $P_N = 3$ will better than $P_L = 2$ $P_N = 3$. Our discussion confines in $P_L = [1, 2, 3]$ and $P_N = [1, 2, 3, 4, 5]$. We did not discuss the higher order NURBS and Lagrange basis, since we think that low order elements might be privileged in engineering applications.

As for the calculation efficiency, although we simultaneously use NURBS basis and Lagrange basis in our formulation, as has been stated in section 2.2, nearly no calculation cost is added for calculating the items about Lagrange basis. In contrast, when use $P_L < P_N$ elements, there will be smaller numbers of basis comparing with P_N order full NURBS element, thus reduces the calculation cost. No additional cost is needed for the definition of fiber vectors in our method.

In another aspect, the method we proposed is a natural extension of the standard degenerated shell model. Less modifications are needed, thus it is easy to implement. No additional requisites on the numbers of quadrature points are needed, reduced quadrature or others [10, 80] can also be used.

3.4 Mixed grid Reissner-Mindlin formulation: NURBS and Serendipity basis functions

In this section, with the similar idea, we use the Serendipity basis to express the fiber vector rotation.

3.4.1 Formulations

The Serendipity basis [141] is widely used in the traditional FEM analysis. In the commercial FEM software, it is the prevalent basis function. Compared with the same order

3. ISOGEOMETRIC SHELL ANALYSIS

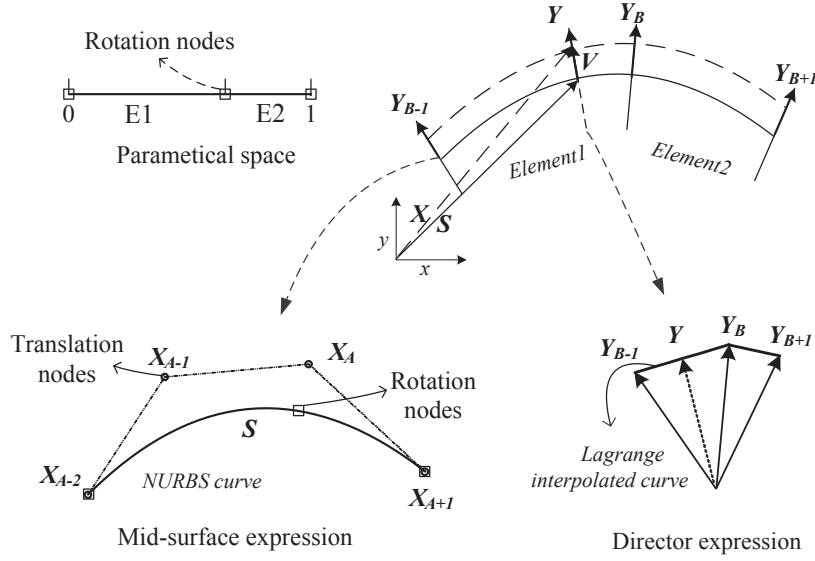


Figure 3.21: A schematic of the mixed grid expression of the shell geometry and its nodes.

Lagrange basis, the Serendipity basis is based on it but has less basis functions. The number of basis functions indicates the number of element DOFs. Its reduction will not only reduce the element level calculation cost but also reduce the cost in the solving of the structure balance equation, since the dimensions of the stiffness matrix will be reduced.

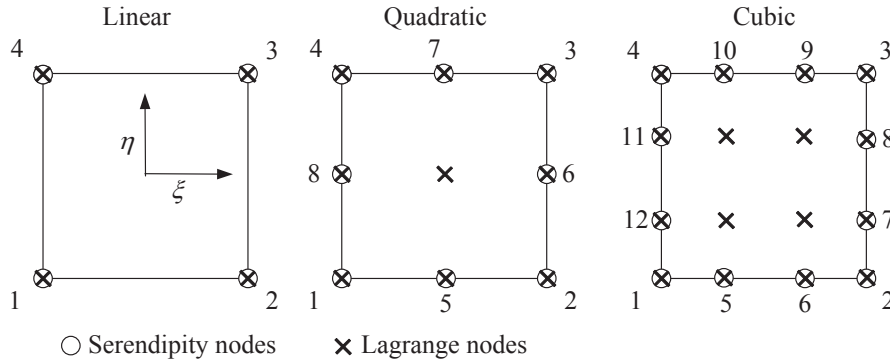


Figure 3.22: The Serendipity and Lagrange nodes in an element in the parametrical space $[-1, 1]^2$.

Figure 3.22 shows the nodes distribution of the Serendipity and Lagrange basis in a 2D quadrilateral element. In linear case, the Serendipity basis is the same with the Lagrange basis. For polynomial order up to three, the Serendipity element does not possess inner nodes while the Lagrange basis does. The generation rule of the Serendipity basis can be found in paper [141]. The linear and quadratic Serendipity basis functions are presented as following:

Linear basis:

$$N_i = \frac{1}{4} (1 + \xi_0) (1 + \eta_0), i = 1, 2, 3, 4 \quad (3.42)$$

$$\xi_0 = \xi_i \xi, \eta_0 = \eta_i \eta$$

Quadratic basis:

$$\begin{aligned} N_5 &= \frac{1}{2} (1 - \xi^2) (1 - \eta), N_6 = \frac{1}{2} (1 - \eta^2) (1 + \xi) \\ N_7 &= \frac{1}{2} (1 - \xi^2) (1 + \eta), N_8 = \frac{1}{2} (1 - \eta^2) (1 - \xi) \\ N_1 &= \hat{N}_1 - \frac{1}{2} N_5 - \frac{1}{2} N_8, N_2 = \hat{N}_2 - \frac{1}{2} N_5 - \frac{1}{2} N_6 \\ N_3 &= \hat{N}_3 - \frac{1}{2} N_6 - \frac{1}{2} N_7, N_4 = \hat{N}_4 - \frac{1}{2} N_7 - \frac{1}{2} N_8 \end{aligned} \quad (3.43)$$

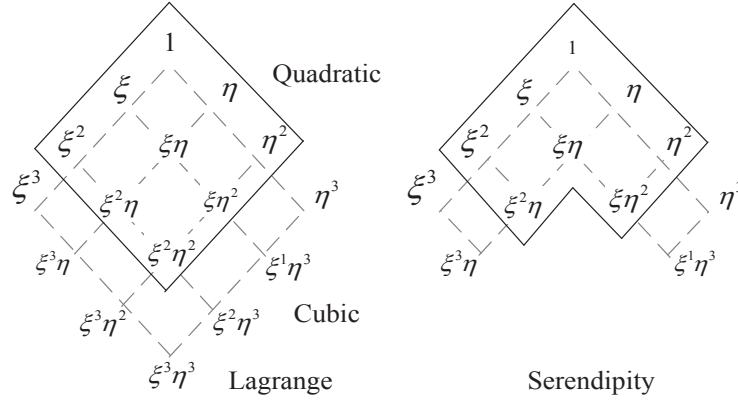


Figure 3.23: The quadratic and cubic polynomial terms in Lagrange and Serendipity basis.

Figure 3.23 shows the polynomial terms in quadratic, cubic Lagrange and Serendipity basis. It can be seen that the Serendipity basis discards some high order terms. It is believed that this treatment hardly affects the approximation accuracy [141].

Using the Serendipity basis in the expression (3.41) where the basis function is noted with N_B , we can get the mixed NURBS/Serendipity IGA Reissner-Mindlin shell formulation. It inherits the characteristics of the NURBS/Lagrange formulation, but with fewer rotational DOFs. Each NURBS basis is related to three translational DOFs, and each Lagrange or Serendipity basis is related to two rotational DOFs. The rotational DOFs savings for Serendipity basis is 2/18 for the quadratic case and 8/32 for the cubic case. However, it is noteworthy that the nodes removed were all inner nodes. It implies that if we evaluate the savings in terms of the dimensions of the total stiffness or mass matrices, the savings will be greater.

We use different order polynomials within the same element. In our study, we confine the polynomial orders to be lower than four. The previously introduced shell obstacle

3. ISOGEOMETRIC SHELL ANALYSIS

course is used here. Various NURBS regularities, from zero to the basis's highest regularity, are used. The abbreviations “N”, “L”, “S”, “C” denote the order of NURBS basis, the order of Lagrange basis, the order of Serendipity basis and the NURBS regularity respectively. Their combinations indicate the case studied. For example, “ $N3L3C0$ ” indicates cubic C^0 NURBS basis and cubic Lagrange basis are used.

The formulations with the same order NURBS/Serendipity (or Lagrange) are named the “same order”. We also study the case that the Serendipity (Lagrange) basis used is one order lower than the NURBS, it is named the “lower order”. Table 3.1 shows the number of element DOFs in various formulations. It should be mentioned that the element DOFs is not relevant to the regularity of the NURBS basis. So we did not note the regularities in the table.

Table 3.1: The Various formulations' element level DOFs.

NURBS order	Lagrange order			Serendipity order	
	linear	quadratic	cubic	quadratic	cubic
quadratic	35	45		43	
cubic		66	80	64	72

3.4.2 Numerical examples

We test our formulations with the shell benchmark problems. The problem setups and other information have been introduced in previous section. Figure 3.24 and 3.25 illustrate the results from the NURBS/Lagrange and the NURBS/Serendipity formulations respectively. The full gauss quadrature is used here. The number of quadrature points is determined by the highest polynomial order used. We can observe the following facts:

(a). There is little difference between the results from the “same order” formulations and those from the “lower order” formulations.

(b). The NURBS/Serendipity formulations perform nearly the same as their counterpart NURBS/Lagrange formulations.

(c). For the same order NURBS, the structure will become stiffer with the increase of the regularity. For example, the “ $N3S3C2$ ” (Cubic NURBS/Serendipity, C^2 regularity) is stiffer than “ $N3S3C1$ ”, and the “ $N3S3C1$ ” is stiffer than “ $N3S3C0$ ”. This phenomenon has also been reported in full NURBS formulated Reissner-Mindlin shell [3].

3.4.3 Discussions

From the numerical results, we can see that the NURBS basis function can also work together with the Serendipity basis functions, the results obtained are also reasonable.

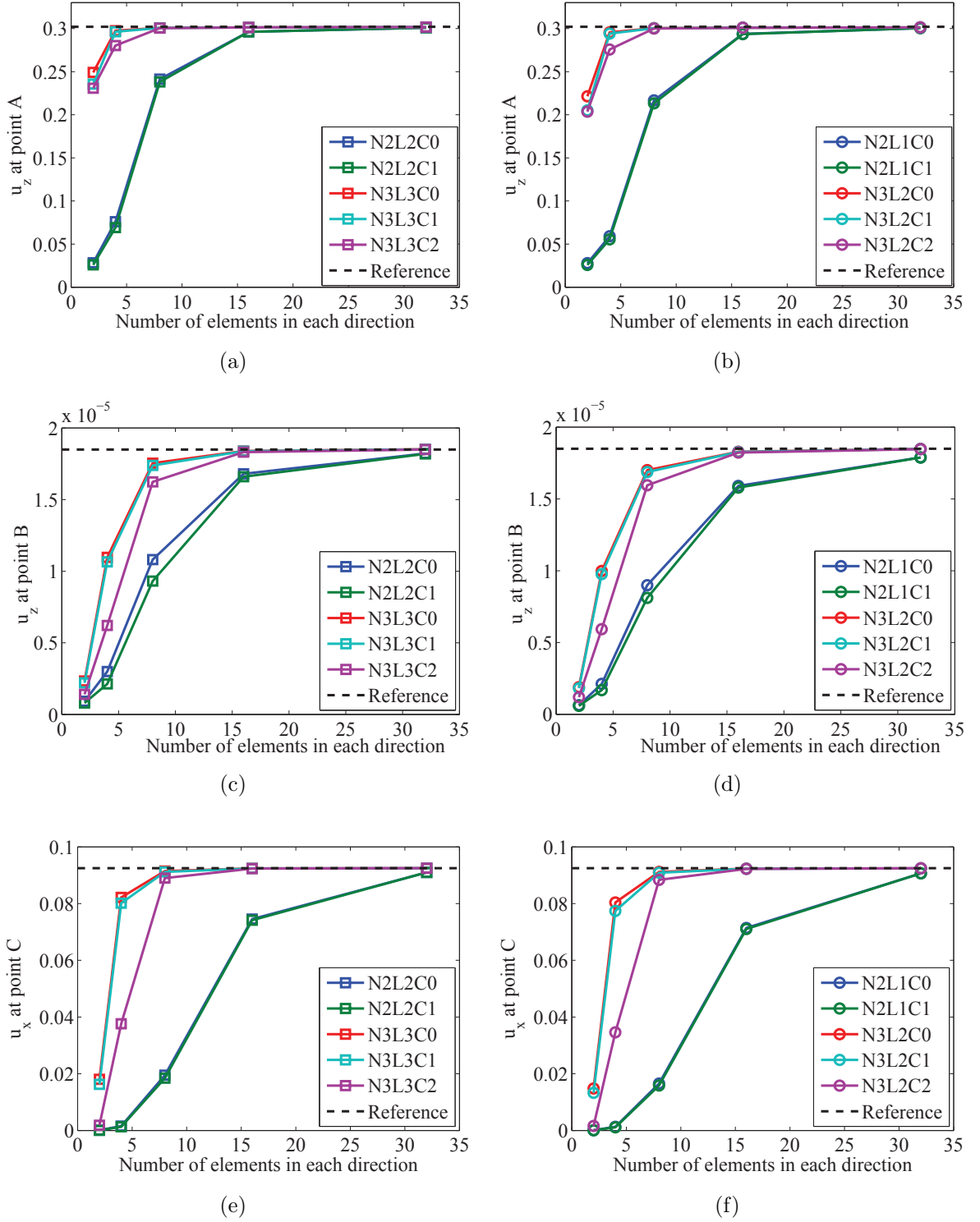


Figure 3.24: The shell obstacle course results from the NURBS/Lagrange formulation. First row: Scordelis-Lo roof problem. Second row: Pinched cylinder problem. Third row: Hemisphere problem. Left column: The “same order” formulations. Right column: The “lower order” formulations. The abbreviations “N”, “L”, “C” denote the order of NURBS basis, the order of Lagrange basis and the NURBS regularity respectively.

3. ISOGEOMETRIC SHELL ANALYSIS

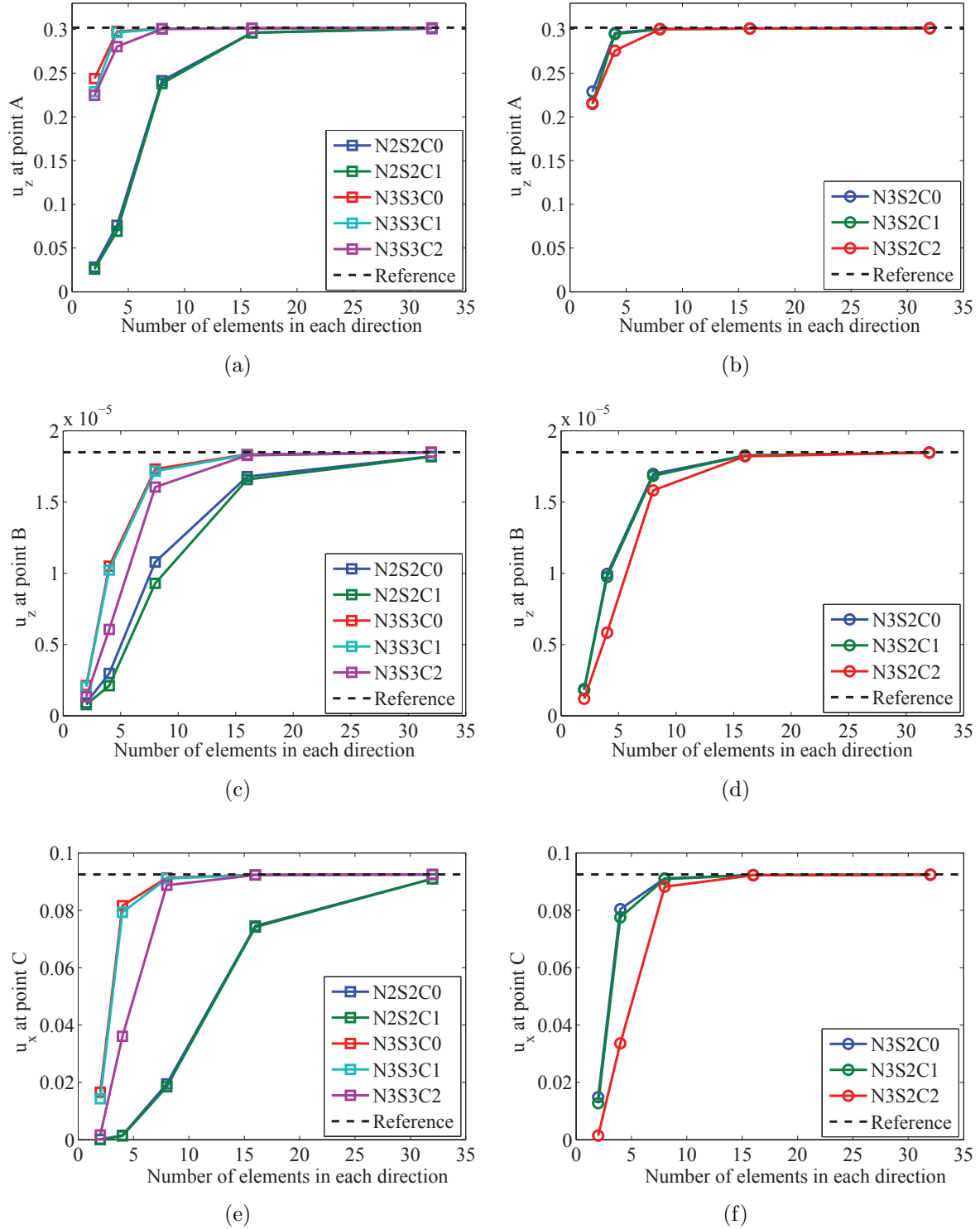


Figure 3.25: The shell obstacle results from the NURBS/Serendipity formulations. First row: Scordelis-Lo roof problem. Second row: Pinched cylinder problem. Third row: Hemisphere problem. Left column: The “Same order” formulations. Right column: The “Lower order” formulations. The abbreviations “N”, “S”, “C” denote the order of NURBS basis, the order of Serendipity basis and the NURBS regularity respectively.

3.5 Transverse shear locking test

Locking is a frequently mentioned terminology in shell analysis. It describes a phenomenon that the solution converges slower, even cannot converge in the extreme cases, when the shell becomes thinner (shear locking) or the curvature becomes larger (membrane locking), etc. The unbalance of the functional spaces is the root of this phenomenon [23]. Various locking relief methods in FEM exist, see [24, 102, 140]. Their essential ideas can also be used in the IGA method with some modifications or even intact [2, 3, 26, 27, 31, 53, 54]. Locking treatment normally will increase the computational expense and need more programming effort. However, this is not the case with the reduced quadrature method [77, 140], it can relieve the locking and at the same time improve the efficiency.

Various types of locking exist in the current Reissner-Mindlin shell formulation. In this article, we only investigate shear locking effect. It is a phenomenon that the numerical solution deteriorates with the plate becomes thinner. The root of this problem is that the formulation cannot express shearless and inextensional bending deformation.

The shear deformation in Reissner-mindlin plate formulation is [3, 77]

$$\boldsymbol{\gamma} = \{w_{,y} - \theta_x, w_{,x} - \theta_y\}. \quad (3.44)$$

Here, w is the normal deformation of the plate. θ_x and θ_y are the fiber rotation angles. When the plate becomes very thin, it should behave as Kirchhoff-Love shell, that is $\boldsymbol{\gamma} = \mathbf{0}$. However, in the Reissner-Mindlin shell formulation, the w and $\boldsymbol{\theta}$ are expressed by different polynomials, so it is not guaranteed that w , can express $\boldsymbol{\theta}$ exactly. Even when a one order higher polynomial is used to express w , it is still not guaranteed, since the node location also affects the equivalence of the functional spaces. However, we still investigate this case in our article.

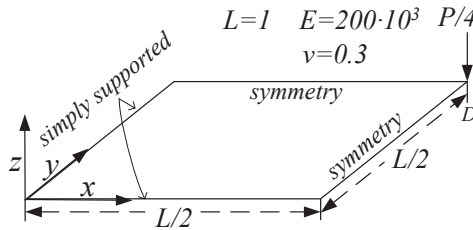


Figure 3.26: The simply supported square plate problem setup.

We use simply supported square plate problem to investigate the locking in our formulation. Figure 3.26 shows the problem setup. Due to the symmetry of the structure, only one quarter of the structure is modeled. It has been used in paper [3] and [52] to test their models. Here we use the same problem setup and coefficients with the paper [3]. The theoretical solution of the normal displacement at point D is given by Timoshenko et al. [129] as

3. ISOGEOMETRIC SHELL ANALYSIS

$$w = \frac{4P}{\pi^4 DL^2} \sum_{m=0}^{\infty} \sum_{n=0}^{\infty} \frac{1}{\left(\left(\frac{2m+1}{L}\right)^2 + \left(\frac{2n+1}{L}\right)^2\right)}. \quad (3.45)$$

$$D = \frac{Eh^3}{12(1-\nu^2)} \quad (3.46)$$

With the shell thickness $h_0 = 10^{-2}$, and the load $P_0 = 10$, the analytical solution will be $w_{ref} = 6.3341 \times 10^{-6}$.

If we change the thickness but keep the term $\frac{4P}{\pi^4 DL^2}$ constant, the result will not change. We will test the cases that $h = 10^{-3}$ and 10^{-5} , their corresponding loads can be obtained by $P = P_0(h/h_0)^3$. The polynomial used will be cubic and quadratic. The rotation part basis will be the Lagrange and the Serendipity. Both the “same order” model and the “lower order” model are studied. In short, all the cases will be the same as what appeared in the former section.

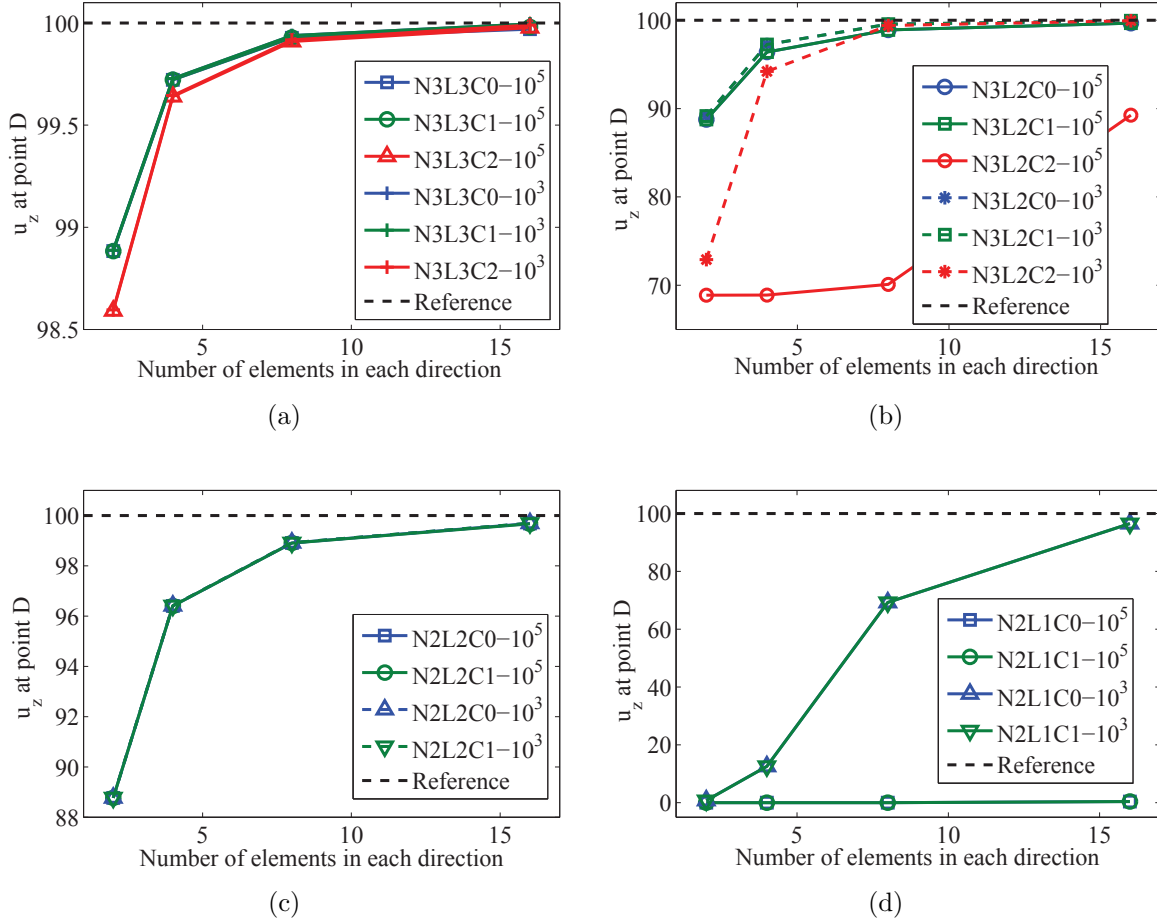


Figure 3.27: The square plate problem results from the NURBS/Lagrange formulation. Left column: The “Same order” formulations. Right column: The “Lower order” formulations. The abbreviations “N”, “L”, “C” denote the order of NURBS basis, the order of Lagrange basis and the NURBS regularity respectively. The number 10^3 and 10^5 refer to the plate slenderness.

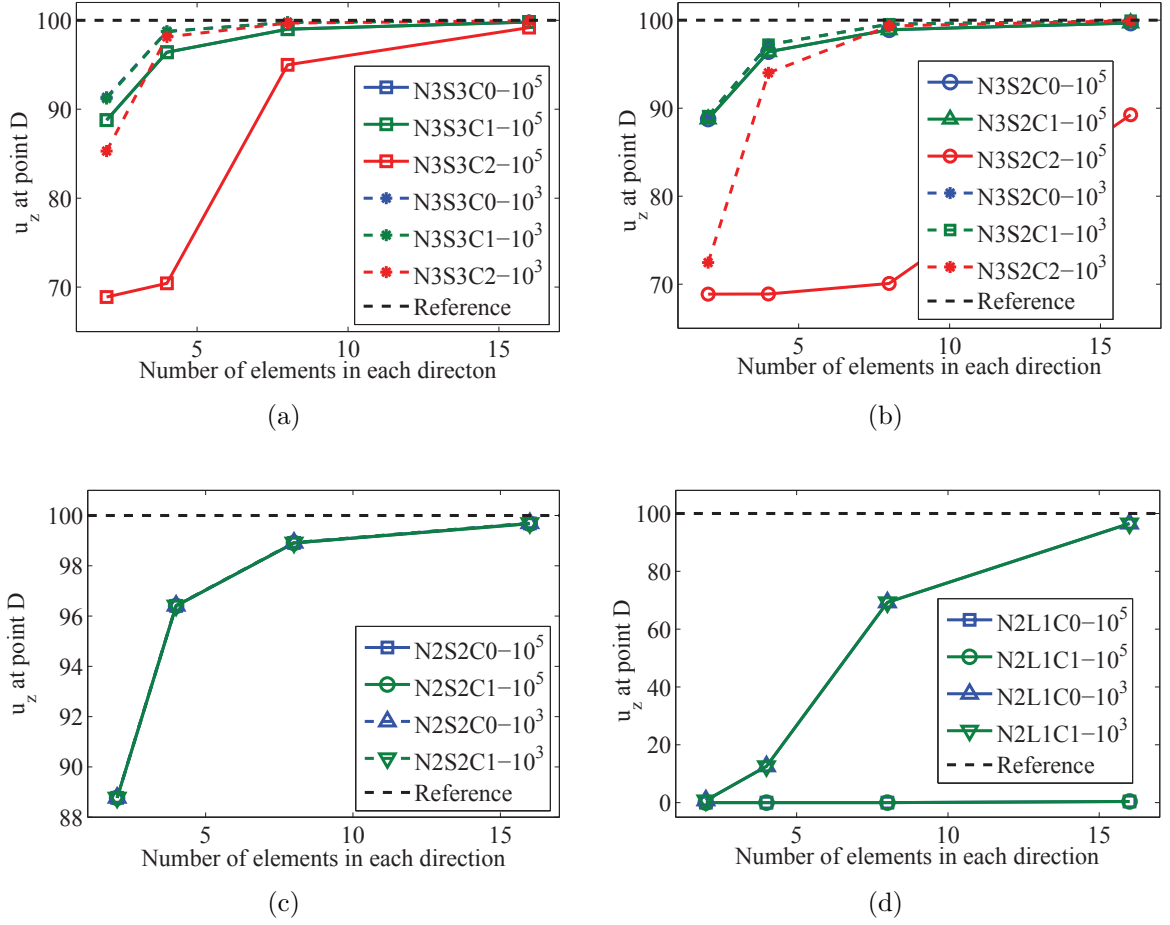


Figure 3.28: The square plate problem results from the NURBS/Serendipity formulation. Left column: The “Same order” formulations. Right column: The “Lower order” formulations. The abbreviations “N”, “S”, “C” denote the order of NURBS basis, the order of Serendipity basis and the NURBS regularity respectively. The note “L1” is identical with “S1”. The number 10^3 and 10^5 refer to the plate slenderness.

Figure 3.27 and 3.28 show the results from the NURBS / Lagrange and NURBS / Serendipity formulations respectively, they are normalized with the analytical solution like in the paper [3]. It can be observed that:

(a). All the formulations can work, no matter which basis is used (Lagrange or Serendipity), and no matter whether the same order basis or the one order lower (than NURBS) basis is used.

(b). The shear locking only slows the convergence rate in most cases, the high order elements behave better than the low order elements. In the very thin shell case ($L/h = 10^5$), only “N2L1C0” and “N2L1C1” (The quadratic “lower order” formulation) are totally locked. The formulation “N3S(L)2C2” is deteriorated more severely than other cubic formulations (“N3S(L)2C0” and “N3S(L)2C1”).

(c). When the shell changes from moderate thin ($L/h = 10^3$) to very thin ($L/h = 10^5$), the results from the “same order” Lagrange formulations do not change (Compare

3. ISOGEOMETRIC SHELL ANALYSIS

“ $NqLqC*$ ” with different slenderness, $q = 2, 3$). The formulations with the quadratic Serendipity basis behave similarly (Compare “ $N2S2C*$ ” with different slenderness). But the cubic formulations with the Serendipity basis behave in another way that $L/h = 10^3$ gives better results than $L/h = 10^5$.

(d). The “same order” formulations give better results than the “lower order” formulations (Compare “ $NqS(L)qC*$ ” with “ $NqS(L)(q-1)C*$ ”, $q = 2, 3$).

(e). The “same order” cubic formulations with Lagrange basis give better results than their Serendipity basis based counterpart (Compare “ $N3L3C*$ ” with “ $N3S3C*$ ”). But there is a small difference between formulations “S2” and “L2”. The rotational DOFs for “S2” and “L2” are almost equal (16 and 18). However, there is a large difference between “S3” and “L3” (24, 32). We think the above phenomenon might be due to the number of DOFs. It implies that the inner nodes of the Lagrange basis might be not useless in our formulations. It should be noted that this is a little conflict with what happened in the former section, changing the Lagrange basis to its Serendipity counterpart there did not affect the results a lot. Those test cases are not as harsh as here.

3.6 Modified reduced quadrature scheme

In IGA analysis, the full gauss quadrature is the prevalent quadrature method. It is directly inherited from the FEM method and does not consider the particularities of IGA. There are other explorations in IGA quadrature aiming to reduce the quadrature points, such as [10, 80, 116]. In this section, we will investigate the characteristics of the NURBS basis and the structure stiffness matrix assembly procedures. Based on them, we give our experimental/intrinsic modified reduced quadrature scheme. We will test it with our shell formulations.

3.6.1 Formulations

We use a one dimensional example to show some characteristics of the NURBS basis. Figure 3.29 shows the cubic NURBS basis functions in a patch with different inter-element regularities. Some properties of NURBS basis are observed as following:

1. One basis function is not a whole polynomial curve, but a piecewise curve composed by t curves, t is positive correlated with the regularity.
2. The boundary basis functions have fewer support intervals. The first basis only has one support interval, see figure 3.29.
3. A basis function owns fewer number of support intervals when the regularity increases, see figure 3.29.

Point 1 inspires us that the IGA basis cannot be fully integrated in its support interval if we use the same method with those used in the FEM, since the basis function in FEM

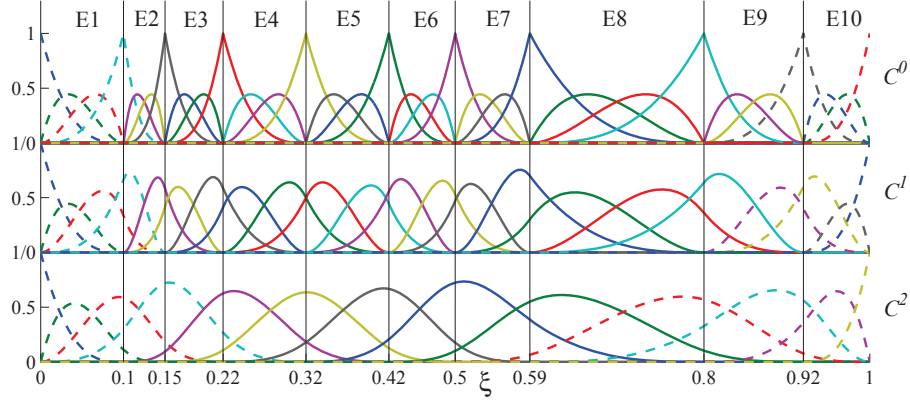


Figure 3.29: The cubic NURBS basis functions within a patch with different regularities.

is a single curve in its support interval, but in IGA not.

Point 2 inspires us that the contributions to a DOF in IGA is given by multiple elements, and the number of elements has a positive correlation with the regularity, see figure 3.30. It is different with FEM. Only IGA C^0 elements behave in the same way with the FEM elements. This might be the reason why IGA can afford less quadrature points. Suppose that we use less quadrature points in the IGA, the stiffness matrix in every element will not be fully integrated, but after assembling them into total stiffness matrix, multiple elements contribute to a single DOF, and the DOFs stiffness are then being strengthened.

Point 3 inspired us that boundary DOFs are weak, since they have fewer support intervals. Take cubic elements for an example, in figure 3.29, it can be seen that the number of intervals (IGA elements) the boundary basis (dot lines in figure 3.29) have are,

C^0 case : 1, 1, 1, 2, ..., 2, 1, 1, 1.

C^1 case : 1, 1, 2, 2, ..., 2, 2, 1, 1.

C^2 case : 1, 2, 3, 4, ..., 4, 3, 2, 1.

The regularity affects the total number of basis in a patch. Figure 3.30 shows the matrix assembly schematic for the one dimensional cubic elements. It can be seen that the total DOFs decrease with the rise of the regularity. The contributions to a DOF are provided by numbers of elements. The numbers are

C^0 case : 1, 1, 1, 2, 1, 1, 2, ..., 2, 1, 1, 1.

C^1 case : 1, 1, 2, 2, 2, ..., 2, 2, 2, 1, 1.

C^2 case : 1, 2, 3, 4, 4, ..., 4, 4, 3, 2, 1.

The boundary DOFs are contributed by fewer elements. The extreme case is the first DOF (and the last), it is only calculated in a single element, and only contributed by one element. If this element is too insufficiently integrated, it will affect a lot the total stiffness matrix. When decreasing the continuity, the number of support intervals will decrease. When C^0 continuous elements are used, it will be the same will C^0 FEM. Some related phenomena already appeared in many papers, like the using of reduced quadrature in

3. ISOGEOMETRIC SHELL ANALYSIS

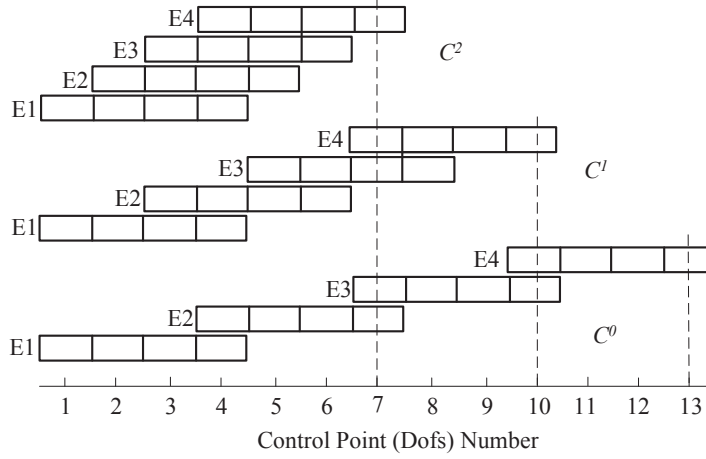


Figure 3.30: A schematic about total stiffness matrix assembly procedure with different inter-element regularities for cubic element in IGA.

IGA brought “hourglass” mode [3], there are more quadrature points in the patch border than in the inner region in optimal quadrature [2, 3, 10], and there exist more quadrature points in the boundary elements in the reduced quadrature scheme proposed in paper [2, 3, 116].

Based on the above analysis, we propose our modified reduced quadrature method. We consider both inter-element regularity and the particularity of the boundary elements. For the one dimension case, the quadrature number is as following:

$$\begin{aligned} \text{Boundary elements} : n_{Gq} &= p - k + 2, \quad k \leq p + 1 - r \\ \text{Inner elements} : n_{Gq} &= p - r, \quad k > p + 1 - r \end{aligned} \quad (3.47)$$

Here, p is the NURBS order, k is the element number counted from the beginning or the ending of the patch. If the mesh does not have a uniform regularity, when an internal knot multiplicity increases, the quadrature point number near this knot should change in the similar way as the boundary elements (details shown in figure 3.31).

Figure 3.31 shows the schematic of the quadrature rule in a patch with 13 elements. The number of quadrature points decrease with the element away from the endpoints. It decreases linearly until the $p + 1$ element. The ending elements are fully integrated with $p + 1$ points. The quadrature point number for inner elements also depends on the regularity. For the highest continuity $r = p - 1$, $n_{Gq} = 1$. When r decreases one, n_{Gq} increases one. For the lowest continuity $r = 0$, $n_{Gq} = p$. For the elements with non-uniform regularity, when knot multiplicity increases by one, the n_{Gq} of elements on both sides of this knot increase by one, the n_{Gq} of the elements with this knot in the center also increase tower-likely depends on their distance to this knot. If there is an overlap between them, the larger one will be chosen. Figure 3.31 shows the n_{Gp} distributions in the cases that $p = 4$, $r = 3$ and 1, and a case that element 6’s right knot is repeated two

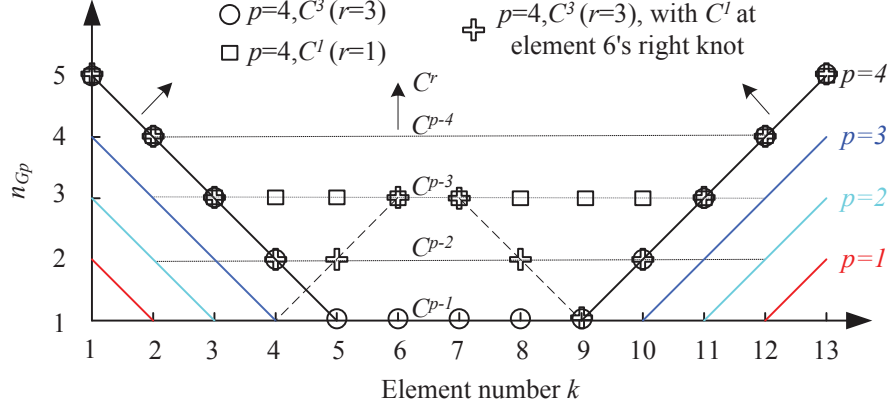


Figure 3.31: A schematic of the proposed modified reduced quadrature rule with 13 elements in a patch.

more times (from $p = 4, r = 3$). It can be seen the tower-like rising of the quadrature point number with the repeated knot in center, and the peak numbers (in element 6 and 7) increase to those of $p = 4, r = 1$. In the overlap elements (in element 4, 5) the larger numbers are chosen.

This reduced quadrature scheme takes into account both the basis support interval number and the regularities. The decrease of the quadrature point number in the patch boundaries is to compensate for the increase in the number of support intervals. Our reduced quadrature scheme is obtained by analysis rather than mathematical deduction. So we call it “heuristic”. However, we think our analysis does reflect the characteristic of the NURBS basis.

The number of quadrature points per DOF is

$$G_m = \frac{2 \left(\frac{1+p+p-r}{2} \right) (p+1-r) + (n-2(p+1-r))(p-r)}{n(p+1) - (r+1)(n-1)}. \quad (3.48)$$

When n is very large, $G_m \approx 1$. It can be seen that after our modification, the number of quadrature points per DOF no longer changes with the regularity. This is the same in the collocation method [115] and similar with that in FEM.

Above is the one dimensional modified reduced quadrature scheme only considering the IGA basis. In the higher dimension case, the quadrature number in an element is the larger one of those determined by each direction. For $p = 2$ and 3, it will be similar but more conservative than those proposed in paper [2, 3], our boundary elements have more quadrature points. We use a Scordelis-Lo roof problem with Kirchhoff-Love shell to test it. Figure 3.32 shows the results. It can be seen the result shows it is applicable in this case.

In our shell formulations, we also use the Lagrange basis functions, so we should also consider their particularities. The map of Lagrange basis is confined within each element, all the advantages of NURBS basis analyzed above no longer exist. We should use more

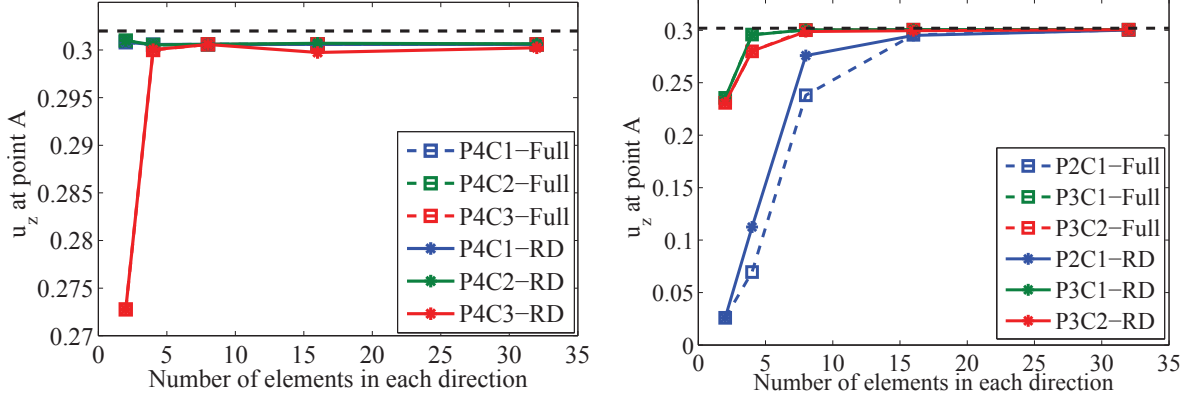


Figure 3.32: The results from Scordelis-Lo roof problem with the Kirchhoff-Love shell, integrated by the full quadrature and the modified reduced quadrature schemes.

quadrature points than in the pure NURBS case. The changed part of the scheme is the inner elements quadrature point number. The Lagrange basis cannot afford to reduce the quadrature points too much, we gave a scheme that for the cubic/quadratic case, the minimum quadrature points number is two, for linear case, it is one. The final quadrature points number in an element is the largest one of those determined by pure IGA rules and the rules above. In an element, the quadrature numbers in the two directions are the same.

3.6.2 Numerical examples

In this section, we apply our quadrature scheme to those examples in the previous section. Their problem setup and other information has been introduced before. All the test cases with Serendipity basis that appeared before will also be tested here. Both the “same order” and the “lower order” formulations are investigated. The “same order” means the Serendipity basis and the NURBS basis used are in the same order, The “lower order” means the Serendipity basis are one order lower than the NURBS basis. Other cases are the same with what has appeared before. The conventions of the legends of the curves are also the same.

Figure 3.33 shows the results from NURBS/Serendipity formulations with our quadrature scheme. It can be seen that the locking in low order elements ($N2S1C*$) are relieved (Compare with figure 3.28). For high order elements, there is no apparent distinction.

Figure 3.34 shows the results from the shell obstacle course. It can be seen that they nearly give the same results with the full quadrature scheme (Compare with figure 3.25). The results obtained from coarse meshes (meshes 2×2 and 4×4) are in fact nearly fully integrated, since they don not have many inner elements. This prevents the phenomenon where the solutions oscillate with an increase in mesh density, which appeared in some locking relief schemes. We think the purpose of locking relief is to make the formulations

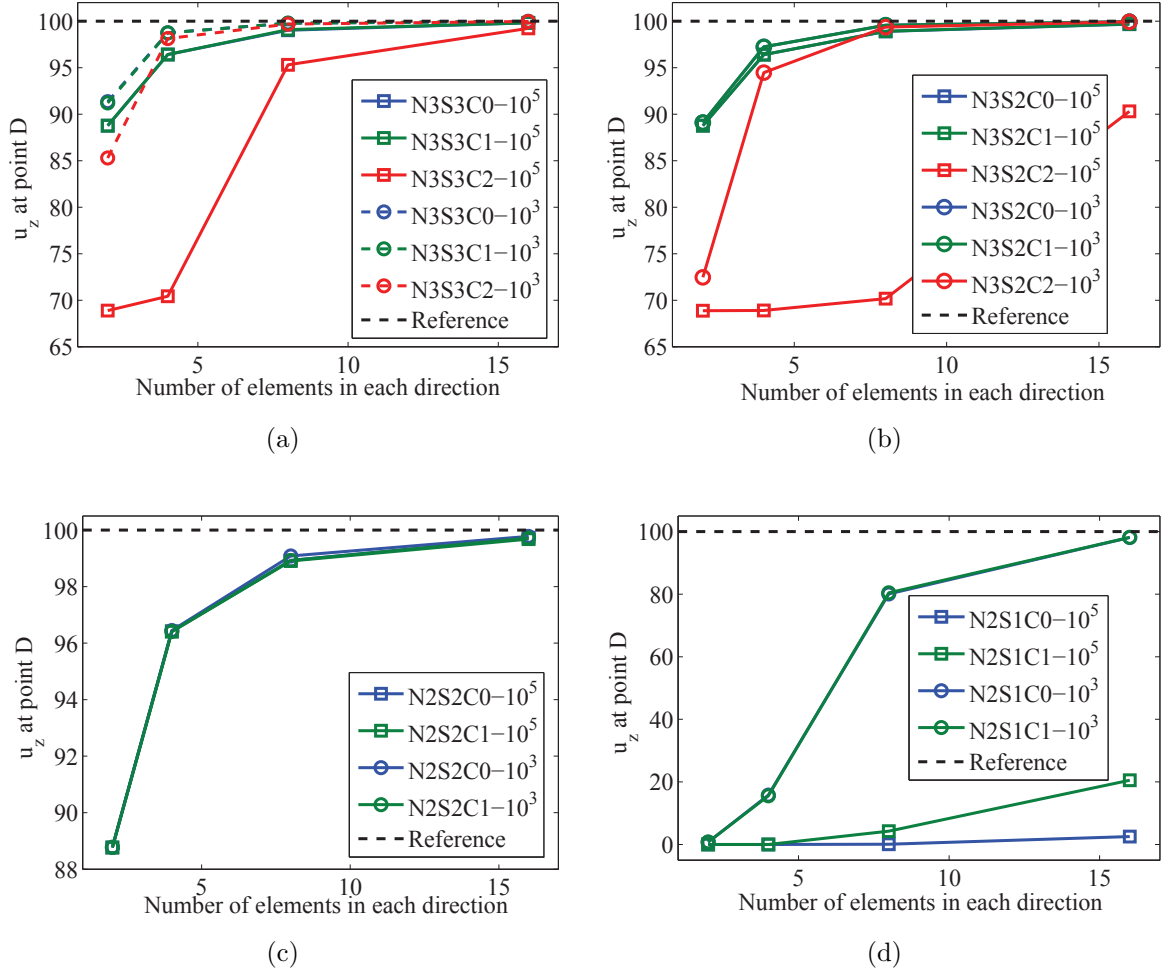


Figure 3.33: The square plate problem results from the NURBS/Serendipity formulations with modified reduced quadrature scheme. Left column: The “Same order” formulations. Right column: The “Lower order” formulations. The abbreviations “N”, “S”, “C” denote the order of NURBS basis, the order of Serendipity basis and the NURBS regularity respectively. The number 10^3 and 10^5 refer to the plate slenderness.

3. ISOGEOMETRIC SHELL ANALYSIS

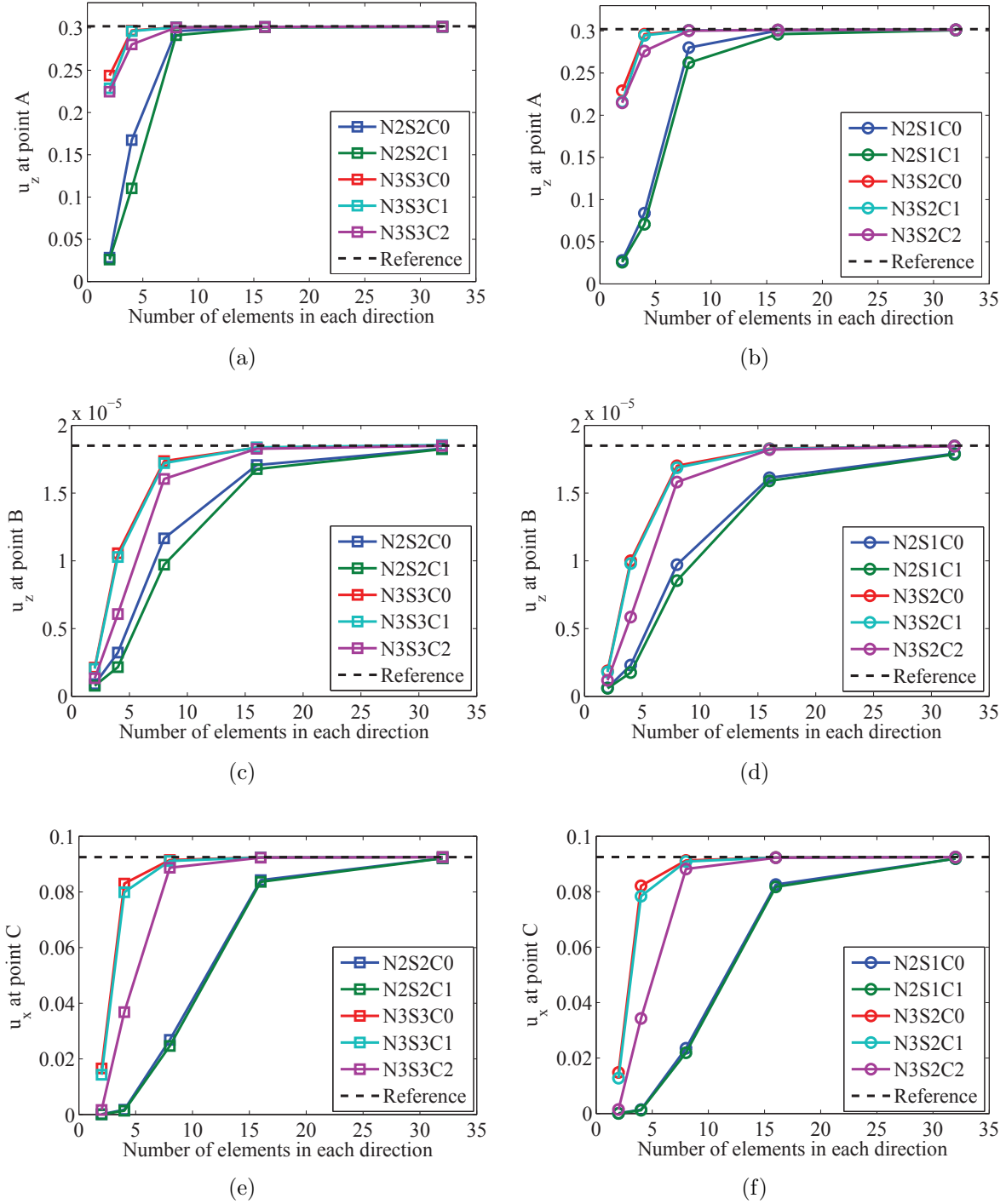


Figure 3.34: The shell obstacle results from the NURBS/Serendipity formulations with modified reduced quadrature scheme. First row: Scordelis-lo roof problem. Second row: Pinched cylinder problem. Third row: Hemisphere problem. Left column: The “same order” formulations. Right column: The “lower order” formulations. The abbreviations “N”, “S”, “C” denote the order of NURBS basis, the order of Serendipity basis and the NURBS regularity respectively.

can give reasonable results at an acceptable mesh density. A reasonable mesh is definitely no lower than $p + 1 \times p + 1$ elements, and might have much more inner elements than

boundary elements.

From the results we can see that our reduced quadrature scheme can reduce the calculation costs and to some extent relieve the shear locking.

3.7 Summary

We use isogeometric shell elements to model the parts with shell properties. The isogeometric shell elements were detailed in this chapter. We presented the linear Kirchhoff-Love shell formulation. We also presented a new IGA Reissner-Mindlin shell formulation which adopts both NURBS basis and Lagrange / Serendipity basis. For such shell elements, we also studied the effect of different order NURBS and Serendipity or Lagrange basis combinations, the results show the effectiveness of our shell elements.

For optimization problem, the efficiency of the structural analysis matters a lot, since a lot of iterations are needed in the optimization. We propose a modified reduced quadrature scheme to relieve the locking at the same time reduce the computational costs for our formulations. It is inspired by the characteristics of the NURBS basis functions and the element stiffness matrices assembly procedures in the IGA analysis. The results show its effectiveness.

Chapter 4

Structural analysis with IGA on multiple domains

The industrial structures are normally composed of many patches when modelled with NURBS. Multiple patch coupling in IGA analysis is thus needed to analyse such structures. In this chapter, we will present a new patch coupling method. Meanwhile, our concern is the structural dynamics aspects, the traditional modal synthesis method is incorporated into the IGA framework, the patch coupling is also needed. This work lays a foundation for the optimization of built-up structures with local parameters concerning structural dynamics criteria, it can reduce the computational costs.

4.1 Isogeometric multiple patches analysis

The domain for analysis in industry is always composed of many patches. These patches should be connected to implement the IGA analysis. We propose a method based on linear constraints to find a connection between the patches. A matrix is designed to denote the patch layout. The C^0/G^1 continuity conditions along the adjacent edges are obtained by patches virtual mutual insertion. They are treated as constraints of the structure balance equation and enforced by the static condensation method and the penalty method. Some examples based on Kirchhoff-Love shell and plane stress elements are inspected.

4.1.1 Isogeometric analysis on multiple patches

There are some difficulties in IGA analysis. One is the creation of an analysis suitable model. IGA uses the same basis functions with these used in CAD. The initial geometry description provides the roughest mesh in analysis, so the basis functions in analysis will be largely predominated by the geometries. It is a little difficult to create a proper model simultaneously considering the shape and analysis requirements, especially for complex structures. This topic has been studied by Schmidt et al. [117], but it is still open. An-

4. STRUCTURAL ANALYSIS WITH IGA ON MULTIPLE DOMAINS

other problem is the difficulty in local refinement. The topology of NURBS (Non-Uniform Rational B-Spline) restricts the meshes in parametric space to be rectangular. Any knot insertion will propagate across the whole domain, thus making the local refinement impossible. To overcome this, T-spline [17] and its simplified version PHT spline (Spline on Hierarchical T-mesh) [98, 136] are introduced, then the Hierarchical B-spline (HB) [133], Truncate Hierarchical B-spline (THB) [62] and Local Refined B-spline (LRB) [48], Hierarchically superimposing local refinement [70]. They are somewhat complicated in implementation or less compatible with the existing NURBS based IGA. Considering above facts, IGA with multiple patches seems to be a good choice. Another potential benefit is that it will not affect the current procedures in NURBS based IGA, only an additional connecting operation is needed later. It also enables an easy implementation of parallel calculation. All these are the motivations of our work.

The commonly used methods for multiple patches connection are proposed by Cottrell et al. [39] and Kiendl et al. [87]. The first works in C^0 connected matching and hierarchical meshes cases. The author gave the continuity condition and then incorporated it into the balance equation by the static condensation method. The second works in G^1 connected matching meshes case. With some modifications, it is also applicable in hierarchical meshes case. The author used two different ideas: static condensation method for C^0 connection (same with the first paper) as well as virtual material method for G^1 connection. The key step in the latter is to create a virtual material layer which will only have bending stiffness across the adjacent regions. The bending stiffness will transfer the moment between patches thus approximately reinforce the G^1 continuity. This method can maintain the angles between patches. The disadvantage is that it cannot work with non-matching meshes, for hierarchical meshes, it also needs adjustments. The calculation of virtual elements will also increase the computation cost. These two methods work well for C^0 and G^1 connection (Matching and Hierarchical meshes) respectively and have been used in some papers [38, 75, 88, 118, 122]. Other connection methods exist like the non-matching Galerkin method based on the modified virtual form for C^0 connection in hierarchical meshes [91] or methods based on the T-mesh [18] and collocation method [9]. The former will bring redundant degrees of freedom and only works for C^0 connection, the latter two are incompatible with existing NURBS IGA.

In general, there are two steps for reinforcing the continuity in FEM: finding the continuity conditions and incorporating them into balance equations. Two types of conditions exist in the first step: constraints with additional parameters and constraints only within the field unknowns. In traditional FEM, fields are approximated with Lagrange basis functions. It is impossible to find a relation among nodes to precisely assure C^0 continuity in non-matching meshes, so the latter method is used. As for the second step, there are two types of methods distinguished by continuity conditions that are fulfilled exactly or approximately. The former requires a linear relation among the field unknowns. The

latter treats the continuity conditions as constraints of the main variational equation, and uses Lagrange multiplier method or penalty method to incorporate them. Typical methods in this category are perturbed Lagrange multiplier method, penalty method [139] and Nitsche's method [55, 139]. Paper [8, 113] give a thorough study about their use in IGA with C^0 continuity case. They all have their own characteristics. One can read the papers above for a better insight.

We will give the C^0 and G^1 continuity conditions based on NURBS patches virtual mutual insertion. Similar idea can be found in [39]. We will further give the G^1 connection condition and extend it into non-matching meshes case. Then, we will use the static condensation method and the penalty method to incorporate the constraints. The systematic procedures which are capable of connecting large numbers of patches will be given.

4.1.2 Multiple patches coupling problem

Due to the non-interpolative characteristic of the basis functions, the IGA elements do not pass through the control points except those in the corner of the patch. The parametric map in IGA is confined to the whole patch not just a single element. From this point of view, a patch works as a macro element in FEM.

There are three mesh refinement methods in IGA: h , p and k methods. They are based on knot insertion, order elevation and both respectively. The refinements will enrich the function space without affecting the physical domain or its parameterization. A deep knowledge of this can be obtained from [39]. In multiple patches case, each patch is meshed separately. There will be different control points and elements on their common edges, but the patches in physical space are always fully matching.

Our idea for patch connection is as follows. Step 1: Design a matrix to note the patch connection information. Step 2: Establish the C^0 or G^1 continuity conditions for each adjacent edge. Step 3: Collect all constraints among the relevant control points into a linear homogeneous equation set. Step 4: Incorporate the constraints into the main equation by penalty method or static condensation method.

Multiple patch connection

Only the conforming connected patches case is studied. "Conforming connected" means the common edges should be identically parametrized. We design a matrix to note the patches connectivity. The patches and their common edges are numbered with $1 \sim d_n$ and $1 \sim b_n$ respectively. Each patch's edges: $\partial\Omega = \{\mathbf{S}(\xi, \eta) \in R^3 | \xi, \eta \in \{0, 1\}\}$ are numbered with $1 \sim 4$. The matrix's row indices are the common edge numbers, its non-zero column indices are the two connected patches' index numbers. The integer in that position is corresponding patch's edge number. Figure 4.1(a) shows an example, the first

4. STRUCTURAL ANALYSIS WITH IGA ON MULTIPLE DOMAINS

row $[4, 4, 0, 0]$ indicates that the first patch's 4th edge is connected with the second patch's 4th edge. The whole matrix describes a connection situation shown in figure 4.1(b).

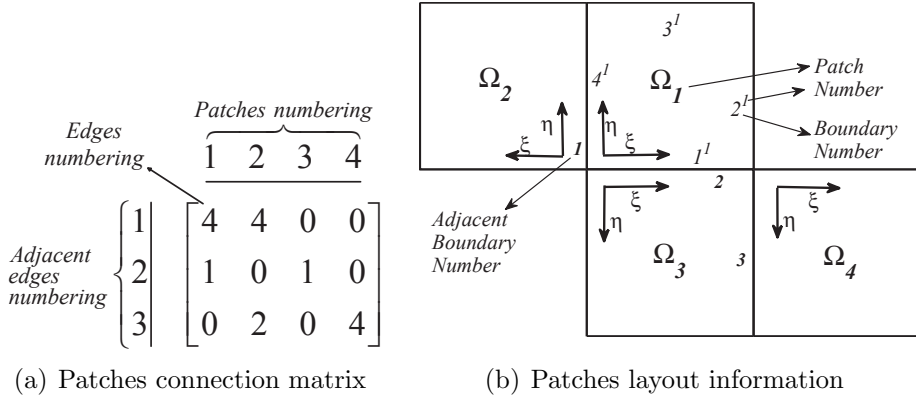


Figure 4.1: Four connected patches' layout (b) and the record in a matrix (a).

The indices of all control points in all patches are rearranged to get a non-overlapping index set. The indices of the two column control points near the adjacent edges are stored sequentially in order to be used in the following procedures, depicted in figure 4.2.

Figure 4.2 shows the 3 types of meshes in multiple patches analysis. They are matching meshes, hierarchical meshes and non-matching meshes. The aim of patches connections is to retain the continuity in the unknown fields.

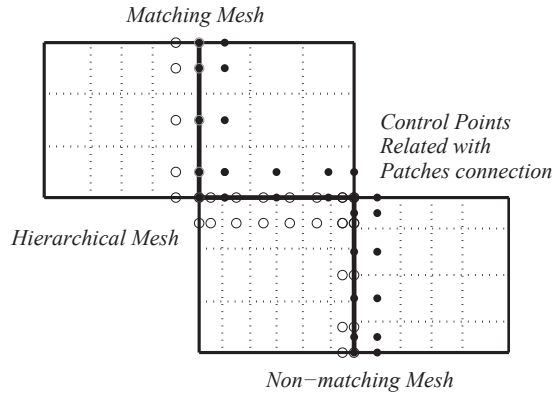


Figure 4.2: Four connected patches with various types of meshes.

Figure 4.3 shows the case that two patches meet at a common edge with C^0 continuity. In patch 3, the common edge is expressed with the knot vector $t^1 = \{t_1^1, t_2^1, \dots, t_{p+m+1}^1\}$ and control points (homogeneous) $P^{w,1} = \{P_1^{w,1}, P_2^{w,1}, \dots, P_m^{w,1}\}$. In patch 4, it can also be expressed with $t^2 = \{t_1^2, t_2^2, \dots, t_{p+n+1}^2\}$ and $P^{w,2} = \{P_1^{w,2}, P_2^{w,2}, \dots, P_n^{w,2}\}$. Given a knot vector $t^{1,2} = t^1 \cup t^2$ and its corresponding control points $Q^w = \{Q_1^w, Q_2^w, \dots, Q_r^w\}$, with Oslo algorithm [35], the relation between $P^{w,1}$ and Q^w will be

$$Q_j^w = \sum_{i=0}^n a_{i,j}^p P_i^{w,1}. \quad (4.1)$$

$$a_{i,j}^0 = \begin{cases} 1 & t_i \leq t_j^* < t_{i+1} \\ 0 & \text{others} \end{cases}, i = 1, 2 \dots m, j = 1, 2, \dots r, \quad (4.2)$$

$$a_{i,j}^p = \frac{t_{j+p}^* - t_i}{t_{i+p} - t_i} a_{i,j}^{p-1} + \frac{t_{i+p+1} - t_{j+p}^*}{t_{i+p+1} - t_{i+1}} a_{i+1,j}^{p-1}, \quad (4.3)$$

with $t^* = t^{1,2}$ and $t = t^1$. The relation between homogenous and non-homogenous control points are

$$\mathbf{Q}_j^w = \begin{bmatrix} w_j \mathbf{Q}_j \\ w_j \end{bmatrix}, \quad (4.4)$$

$$\mathbf{P}_i^{w,1} = \begin{bmatrix} \bar{w}_i \mathbf{P}_i^1 \\ \bar{w}_i \end{bmatrix}. \quad (4.5)$$

Then the C^0 continuity condition for non-homogenous control points will be obtained as

$$\mathbf{Q}_j = \sum_{i=0}^m \frac{a_{i,j}^p \bar{w}_i}{w_j} \mathbf{P}_i^1. \quad (4.6)$$

Rearranging all control points' coordinates into a vector sequentially, the following formulation can be obtained:

$$\mathbf{Q} = \mathbf{A} \mathbf{P}^1, \quad (4.7)$$

where $\mathbf{Q} = [\mathbf{Q}_1^T, \dots, \mathbf{Q}_r^T]^T$ and $\mathbf{P}^1 = [\mathbf{P}_1^T, \dots, \mathbf{P}_n^T]^T$. They indicate the control points' spatial coordinates. $\mathbf{A} = [a_{i,j}]_{vr \times vn}$. $a_{vk-t, vl-t} = \frac{a_{l,k}^p \bar{w}_l}{w_k}, l = 1 \sim m, k = 1 \sim r$. For the 3D problem, $v = 3$ and $t = 0 \sim 2$. For 2D case, $v = 2$ and $t = 0 \sim 1$.

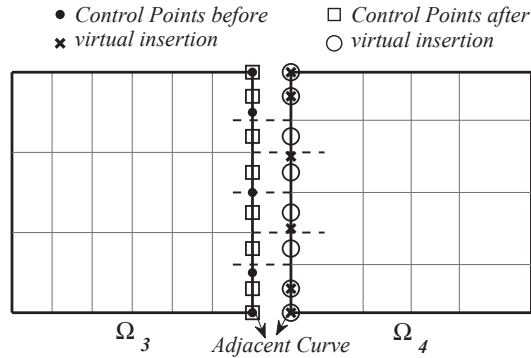


Figure 4.3: Two C^0 connected patches and their virtual mutual insertion.

4. STRUCTURAL ANALYSIS WITH IGA ON MULTIPLE DOMAINS

Case 1. C^0 condition

Applying the above map with knot vectors t^1 and t^2 , since they both express the same curve, the new control points obtained from both sides should be the same and the C^0 continuity condition can be obtained as following:

$$\mathbf{A}_{vr \times vm}^{1,1} \mathbf{P}_{vm \times 1}^{1,1} = \mathbf{B}_{vr \times vn}^{2,1} \mathbf{P}_{vn \times 1}^{2,1} \quad (4.8)$$

The matrix form is

$$\begin{bmatrix} \mathbf{A}_{vr \times vm}^{1,1} & -\mathbf{B}_{vr \times vn}^{2,1} \end{bmatrix} \begin{bmatrix} \mathbf{P}_{vm \times 1}^{1,1} \\ \mathbf{P}_{vn \times 1}^{2,1} \end{bmatrix} = \mathbf{0}, \quad (4.9)$$

$\mathbf{P}_{vm \times 1}^{1,1}$ and $\mathbf{P}_{vn \times 1}^{2,1}$ indicate the coordinates of patch 1 and 2's 1th column of control points near the common edge respectively. $\mathbf{A}_{k \times l}^{i,j}$ and $\mathbf{B}_{k \times l}^{i,j}$ are the map matrices, i, j indicate the patch number and the column number near the common edge, $k \times l$ denotes the matrix size.

Case 2. G^1 condition

Figure 4.4 shows a case that two patches meet with G^1 continuity. G^1 is a type of geometrical continuity, for NURBS surfaces, the adjacent patches should have the same tangent plane at the intersection points. An approximated G^1 condition for matching NURBS patches can be found in [104]. Here, we also adopt this approximated condition: the collinearity of the control points. It is exact only when the G^1 connected patches are created by using the collinearity of the control points, this might be case when people model geometries in CAD softwares, or the patches are created by subdivision of a larger patch. For non-matching and hierarchial meshes, the second columns control points near the common edges should also be virtually inserted, depicted in figure 4.4. Then, we apply matching patches' continuity condition to these virtual patches, an additional condition for G^1 continuity for the two virtual patches will be

$$\mathbf{A}_{vr \times vm}^{1,1} \mathbf{P}_{vm \times 1}^{1,1} - \mathbf{A}_{vr \times vm}^{1,2} \mathbf{P}_{vm \times 1}^{1,2} = \mathbf{c}_{vr \times 1} (\mathbf{B}_{vr \times vn}^{2,1} \mathbf{P}_{vn \times 1}^{1,1} - \mathbf{B}_{vr \times vn}^{2,2} \mathbf{P}_{vn \times 1}^{2,2}). \quad (4.10)$$

Together with the C^0 condition, the G^1 condition in matrix form is as following:

$$\begin{bmatrix} \mathbf{A}_{vr \times vm}^{1,1} & \mathbf{0} & -\mathbf{B}_{vr \times vn}^{2,1} & \mathbf{0} \\ \mathbf{A}_{vr \times vm}^{1,1} & -\mathbf{A}_{vr \times vm}^{1,2} & -\mathbf{c}_{vr \times 1} \mathbf{B}_{vr \times vn}^{2,1} & \mathbf{c}_{vr \times 1} \mathbf{B}_{vr \times vn}^{2,2} \end{bmatrix} \begin{bmatrix} \mathbf{P}_{m \times 1}^{1,1} \\ \mathbf{P}_{m \times 1}^{1,2} \\ \mathbf{P}_{n \times 1}^{1,1} \\ \mathbf{P}_{n \times 1}^{2,2} \end{bmatrix} = \mathbf{0} \quad (4.11)$$

The meanings of the notations have been stated before. The parameter \mathbf{c} can be obtained from the geometric relation between the adjacent patches.

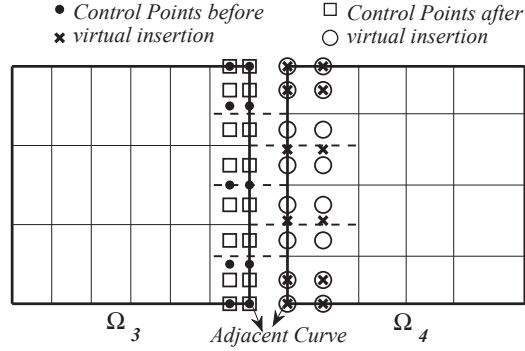


Figure 4.4: Two G^1 connected patches and their virtual mutual insertion.

Until now, both C^0 and G^1 continuity condition for each common edge can be expressed by the following equation:

$$\mathbf{L}_e \mathbf{P}_e^c = 0 \quad (4.12)$$

Here, e indicates the common edge numbers and c indicates the affected control points' indices. The content of \mathbf{L}_e and \mathbf{P}_e^c depends on C^0 or G^1 connection situation.

In the cases with multiple common edges, with the recorded common edges index numbers, all condition matrices will be collected into a single matrix like the way in the formation of total stiffness matrix in FEM:

Step 1 : Generate a matrix

$$\mathbf{L} = \begin{bmatrix} \mathbf{L}_1 & 0 & \cdots & 0 \\ 0 & \mathbf{L}_2 & \cdots & 0 \\ \vdots & \vdots & \ddots & \vdots \\ 0 & 0 & \cdots & \mathbf{L}_{b_n} \end{bmatrix}. \quad (4.13)$$

Step 2 : Add \mathbf{L} 's columns related to the repeated control points to a single column. The redundant repeated index numbers and their corresponding columns will be deleted. Then, the continuity condition for multiple patches can be obtained as

$$\mathbf{L} \mathbf{P}^c = \mathbf{0}. \quad (4.14)$$

This condition will be kept in field unknowns and then introduced to the balance equation by penalty method or static condensation method.

4. STRUCTURAL ANALYSIS WITH IGA ON MULTIPLE DOMAINS

Incorporation of continuity condition-Static condensation Method

Static condensation method [57] is commonly used in FEM to achieve model reduction. Some unknown variables can be expressed by others, so their contributions to the stiffness matrix can be accounted by modifying other nodes' stiffness, thus the dimensions of the matrix are reduced.

The linear independent solutions (the null space) of constraints equation (4.14) can be viewed as a map for recombining existing basis functions, their coefficients work as new control points. It gives the relation between the initial and new control points, and also between their attached unknown variables. In structure analysis, the unknown can be displacement \mathbf{U} . Its expression in d_n domains is

$$\mathbf{U} = [\mathbf{U}_1^T, \dots, \mathbf{U}_{d_n}^T]^T. \quad (4.15)$$

The map between condensed $\bar{\mathbf{U}}$ and \mathbf{U} is

$$\bar{\mathbf{U}} = \mathbf{T}\mathbf{U}. \quad (4.16)$$

$$\mathbf{T} = \begin{bmatrix} \mathbf{I}_r & \mathbf{0} \\ \mathbf{0} & \mathbf{T}_c \end{bmatrix}, \quad (4.17)$$

$\mathbf{T}_c = \text{null}(\mathbf{L})$, $\text{null}(\mathbf{L}) = \{\mathbf{v} \in \mathbb{R}^3 : \mathbf{L}\mathbf{v} = \mathbf{0}\}$. This can be obtained by directly solving the above linear equation or by singular value decomposition (SVD). \mathbf{I}_r is $r \times r$ dimensional identity matrix. It should be noted that here \mathbf{U} should be arranged in the sequence that the affected control points' components appear in the end of the vector, so do the stiffness matrix and force vector.

The structure balance equation in the whole domain is

$$\mathbf{K}\mathbf{U} = \mathbf{F}. \quad (4.18)$$

\mathbf{K} denotes the structure stiffness matrix

$$\mathbf{K} = \begin{bmatrix} \mathbf{K}_1 & & \mathbf{0} \\ & \ddots & \\ \mathbf{0} & & \mathbf{K}_{d_n} \end{bmatrix}. \quad (4.19)$$

\mathbf{F} denotes structure load

$$\mathbf{F} = [\mathbf{F}_1^T, \dots, \mathbf{F}_{d_n}^T]^T. \quad (4.20)$$

Substituting \mathbf{U} in equation (4.18) with equation (4.16) and left multiplying \mathbf{T}^T with

both sides, we can get the condensed form balance equation

$$\mathbf{T}^T \mathbf{K} \mathbf{T} \bar{\mathbf{U}} = \mathbf{T}^T \mathbf{F}. \quad (4.21)$$

The initial unknown variables are retrieved by the equation (4.16).

Incorporation of continuity condition-Penalty Method

In FEM analysis, the penalty method [139] is another choice to incorporate constraints. The solution of the physical analysis is the minimum point of a variational function (energy function), when adding a large enough quadratic form, the optimum point will be reached only when this quadratic form equals zero, thus the constraints will be satisfied. With the stationary condition of the extended formulation, the following equation can be obtained:

$$\delta W + \delta W_{\text{penalty}} = 0 \quad (4.22)$$

The penalty term is

$$\delta W_{\text{penalty}} = \sum_{i=1}^m \frac{1}{2} a_i \delta \langle g_i, g_i \rangle_{L^2}, \quad (4.23)$$

where g_i is the i^{th} constraint and a_i its penalty coefficient. $\langle \cdot, \cdot \rangle_{L^2}$ denotes the inner product in square integrable function space. The constraints here are linear equations, so $\langle g_i, g_i \rangle_{L^2}$ will be $\mathbf{g}_i^T \mathbf{g}_i$.

An additional contribution to the tangent stiffness matrix will be

$$\mathbf{K}_{rs}^{\text{penalty}} = a \sum_{i=1}^m \left(\frac{\partial g_i^T}{\partial u_s} \frac{\partial g_i}{\partial u_r} + g_i^T \frac{\partial^2 g_i}{\partial u_r \partial u_s} \right) = a \sum_{i=1}^m (L_{is} L_{ir}). \quad (4.24)$$

The matrix form is

$$\mathbf{K}^{\text{penalty}} = a \mathbf{L}^T \mathbf{L}. \quad (4.25)$$

Adding each element in $\mathbf{K}^{\text{penalty}}$ to the total stiffness matrix (4.19) according to the related control points' indices, the patches will be connected. The initial force vector (4.20) is unaffected.

4.1.3 Numerical examples

In this section, we will present 3 examples: a 2D cantilever beam problem modeled by plane stress elements, Scordelis-Lo roof and pinched cylinder problems modeled by Kirchhoff-Love shell elements [85, 86]. They will be analyzed with matching, hierarchical and non-matching meshes. The constraints will be introduced with the two methods stated above. The results will be compared with each other and with those from bending

strip method [87].

Cantilever beam

Figure 4.5 shows the problem setup. The Young's modulus is 2.1×10^4 and the Poisson's ratio is 0.49. It is subjected to a parabolic traction $p_y = -0.75P(1 - (y - 1)^2)$ with $P = 300$. It is modeled with 2 patches and analyzed with plane stress elements. The common boundary is $x = 4$, C^0 continuity should be reinforced along this line.

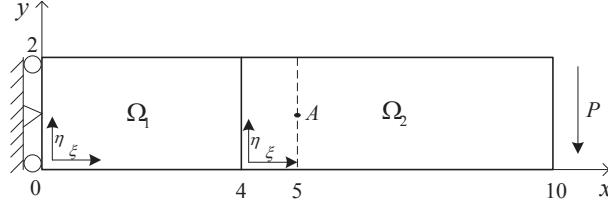


Figure 4.5: The cantilever beam problem setup. Beam length $L = 10$ and height $h = 2$.

In the matching mesh case: Ω_1 and Ω_2 are uniformly meshed with 10×10 ($\xi \times \eta$) and 20×10 ($\xi \times \eta$) elements respectively. In the hierarchical case: Ω_1 , 10×20 and Ω_2 , 20×10 . In the non-matching case: Ω_2 is meshed the same with that in the matching mesh case. For Ω_1 , the ξ direction is meshed the same with that in the matching mesh case. The knot vector in the η direction is $\Xi_\eta^1 = \{0, 0, 0, t, 1, 1, 1\}$ with $t = 1.0001 \times \{1/N, \dots, i/N\}$, $i = 1 \sim N - 1$ and $N = 10$. Figure 4.6 shows the non-matching mesh. It is slightly different to the matching meshes, see the center of the picture. Our purpose is to test whether or not it can give the same results with the matching meshes. Since we think this slight deviation in knot vector will not affect a lot the basis functions, if they give different results, problems must lie within the patch connection.

The analytical results of this problem are given in [126] as following:

$$u_x = -\frac{Py}{6EI} \left[(6L - 3x)x + (2 + \mu) \left((y - 1)^2 - \frac{h^2}{4} \right) \right] \quad (4.26)$$

$$u_y = -\frac{P}{6EI} \left[3\mu(y - 1)^2(L - x) + (4 + 5\mu) \frac{h^2x}{4} + (3L - x)x^2 \right] \quad (4.27)$$

$$\sigma_x = \frac{P}{I} (L - x)(y - 1), \sigma_y = 0, \tau_{xy} = -\frac{P}{2I} \left[\left(\frac{h}{2} \right)^2 - (y - 1)^2 \right] \quad (4.28)$$

Figure 4.7 shows the results from matching meshes and hierarchical meshes. It can be seen that all the results coincide with the analytical solution. When a very large penalty coefficient was used in the penalty method, the results did not change.

Figure 4.8 shows the results from non-matching meshes. The result from penalty method with the penalty coefficient 10^7 coincides with reference value. The results from the static condensation method and the penalty method with a penalty coefficient of 10^{16}

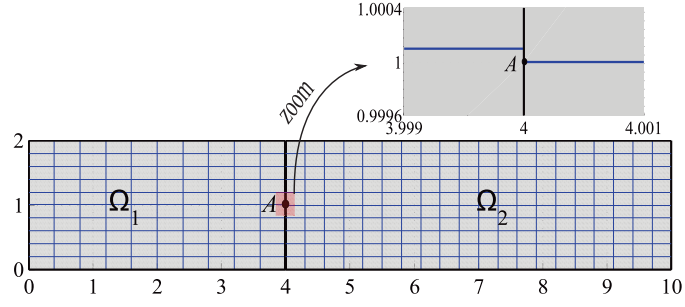


Figure 4.6: The non-matching mesh of the cantilever beam.

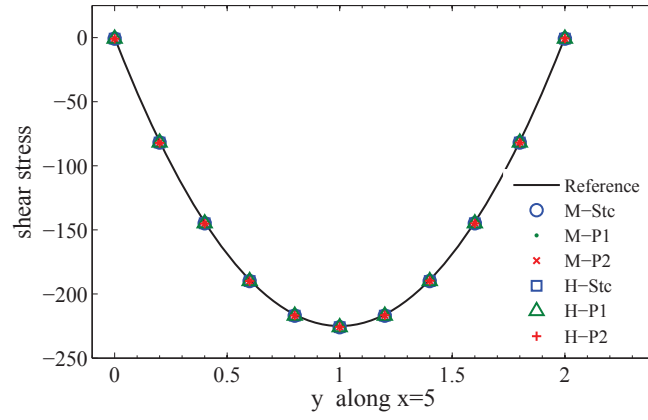


Figure 4.7: Cantilever problem results: The shear stress results along $x = 5$ from different methods with matching meshes and hierarchical meshes. “M”, “H” indicate matching meshes and hierarchical meshes respectively. “Stc”, “P1” and “P2” indicate static condensation method, penalty method with the penalty coefficient 10^7 and 10^{16} .

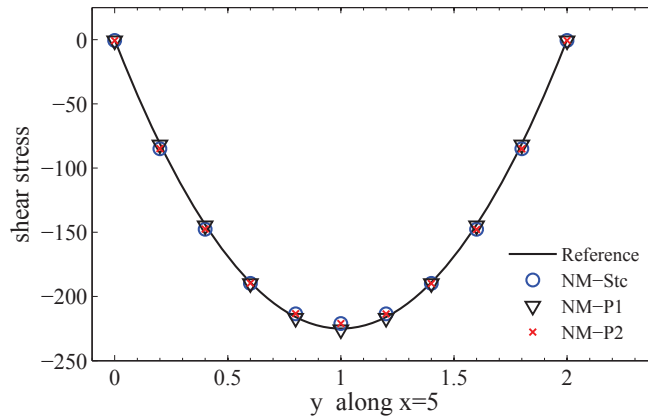


Figure 4.8: Cantilever problem results: The shear stress results along $x = 5$ from non-matching meshes. “NM” indicates non-matching meshes. Other notations are the same with these in figure 4.7.

4. STRUCTURAL ANALYSIS WITH IGA ON MULTIPLE DOMAINS

vary a lot with the reference value, however they coincide with each other. An explanation should be given on this phenomenon.

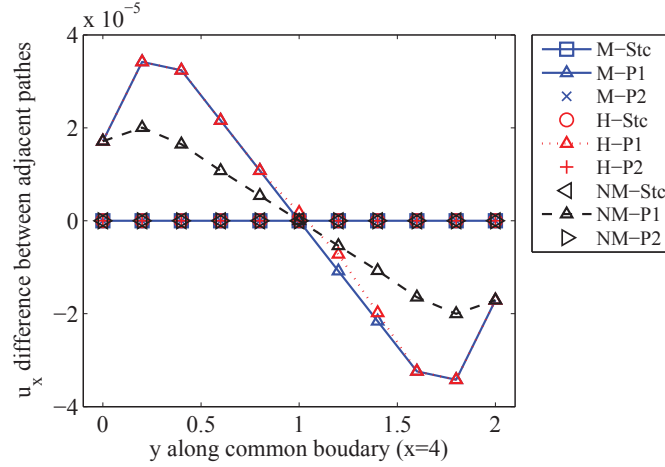


Figure 4.9: Cantilever problem results: u_x differences along the common boundary from different mesh cases and continuity enforcement methods. The meanings of notations are the same with those shown in this example.

Figure 4.9 shows the u_x difference along the common edge from various mesh cases and continuity enforcement methods. It can be seen that the u_x errors from the static condensation method are always zero. In other cases, the larger the penalty coefficient is, the smaller the error is, which also means that the stronger constraints are enforced. When using penalty method with a very large penalty coefficient, the constraints will be imposed as strongly as that with static condensation method, so they gave nearly the same results.

Another question that should be answered is that why the static condensation method gave bad result in non-matching mesh case? Table 4.1 shows the shear stress in point A from some meshes. Ω_2 is always meshed with 20×10 ($\xi \times \eta$) elements. Ω_1 is meshed with $10 \times N$ ($\xi \times \eta$) elements, $N = \{5, 8, 9, 10, 19\}$. Table 4.1 also gives the numbers of basis functions in both patches on their common edge, the number of effective basis functions, the solutions and their errors in different meshes cases. Here, the number of effective basis functions indicates the dimension of the null space of equation (4.14), the larger it is, the more basis functions are involved to approximate the field unknowns on the common edges and vice versa.

We can observe from the table that: (a) In matching meshes ($N=10$), the number of effective basis functions is equal with the number of basis functions in both patches. (b) In hierarchical meshes ($N=5$), it is equal with the smaller one. (c) In non-matching meshes, it is smaller than any of these in both sides. (d) The larger it is, the smaller the error is. (e) In the non-matching case, an increase in the mesh density does not always increase the number of effective basis.

The reasons for these phenomena are that: On the common edge, the field is approx-

Table 4.1: The stress results at point A obtained from static condensation method with non-matching meshes. “Elem Num” indicates the number of elements on Ω_1 ’s η direction. “Num-1” and “Num-2” denote the number of basis functions on the common edge in Ω_1 and Ω_2 respectively. “Num-e” indicates the number of effective basis functions, it is the dimension of the space $Null(\mathbf{L})$, \mathbf{L} refers to equation (4.14).

Elem Num	Stress at point A	Error	Num-e	Num-1	Num-2
5	-225.8828	-0.8828	7	7	12
8	-226.3393	-1.3393	4	10	12
9	-221.0067	3.9933	3	11	12
10	-225.8765	-0.8765	12	12	12
19	-221.0012	3.9988	3	21	12

imated by the common space of these in both patches. The larger it is, the better the approximation. Matching meshes and hierarchical meshes can give embedded spaces: the common space is the same with one of these in two sides. When the meshes are refined, the common space will be enlarged. In the non-matching case, the common space is the intersection of those on both sides. The expansion of each space will not assure that of common space. However, it is natural to think that if we release the criteria of common space, this “common space” must be enlarged with the meshes refinements. It is achieved by weakly imposing the continuity condition. That is the reason why in figure 4.8 penalty method with a relatively low penalty coefficient (line $P1$) gave the same results with reference solution.

The conclusion we drive from this example is that: In matching mesh and hierarchical mesh cases, both static condensation method and penalty can work. In the non-matching mesh case, only the penalty method with a reasonable penalty coefficient is applicable. We will verify it in the following examples.

Scordelis-Lo roof problem

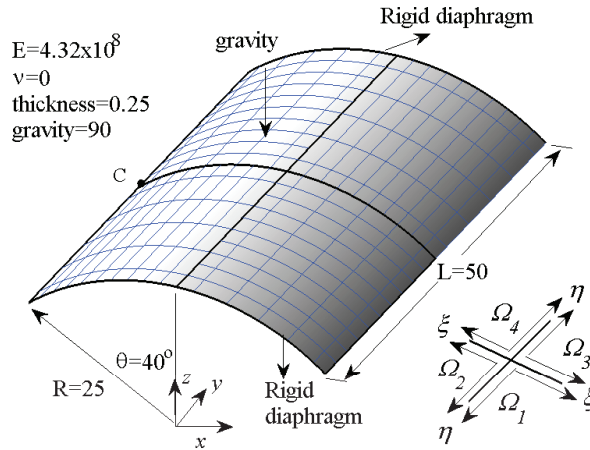


Figure 4.10: Scordelis-Lo roof problem setup. It also shows a case of hierarchical meshes.

4. STRUCTURAL ANALYSIS WITH IGA ON MULTIPLE DOMAINS

Figure 4.10 shows the Scordelis-Lo roof problem setup and the material properties. It composes four patches. It is analyzed with quadratic Kirchhoff-Love shell elements. In matching meshes, every patch is uniformly meshed with $N \times N$ ($\xi \times \eta$) elements, $N = \{4, 8, 12, 16, 20\}$. In hierarchical meshes, Ω_1, Ω_4 's η direction and Ω_2, Ω_3 's ξ direction are uniformly meshed with the same knot vector Ξ . The knot vector is $\Xi_\eta^1 = \Xi_\eta^4 = \Xi_\xi^2 = \Xi_\xi^3 = \Xi$, $\Xi = \{0, 0, 0, t_1, 1, 1, 1\}$ with $t_1 = \{1/N, \dots, i/N\}$, $i = 1 \sim N-1$. $N = \{4, 10, 16, 22, 28\}$. The remaining parametric directions of all the patches are meshed with another knot vector $H = \{0, 0, 0, t_2, 1, 1, 1\}$ with $t_2 = \{t_1(1), t_1(3), \dots, t_1(2i-1), \dots\}$. In the non-matching case, $\Xi_\eta^1 = \Xi_\eta^4 = \Xi_\xi^2 = \Xi_\xi^3 = \Xi$, The remaining parametric directions are based on it but perturbed as $\Xi' = \{0, 0, 0, t_3, 1, 1, 1\}$ with $t_3(k) = 1.0001 \times t_1(k)$, $k = 2 \sim N-2$. N is the same with that in the matching mesh case.

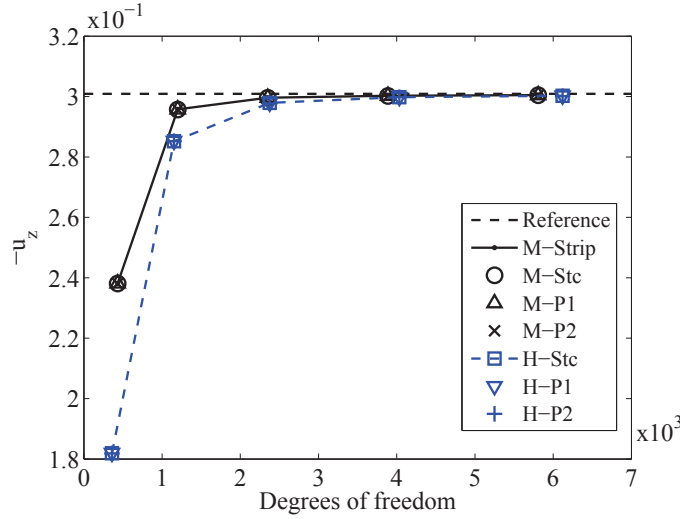


Figure 4.11: Scordelis-Lo roof problem: u_z at point C varies with h refinements. “M”, “H” and “NM” indicate matching, hierarchical and non-matching meshes. “Stc” indicates static condensation method. “P1” indicates penalty method with the penalty coefficient 10^{10} and “P2” with 10^{16} . “Strip” denotes results from bending strip method [87].

Figure 4.11 shows the u_z at point C from matching meshes and hierarchical meshes. The reference value is set as -0.3006 got from [86]. In matching meshes case, all the results coincide with these from bending strip method. In hierarchical meshes, all the results coincide with each other. The trend is the same with what appeared in the former example.

Figure 4.12 shows the results from non-matching meshes. It can be seen that results with static condensation method and penalty method with a large penalty coefficient (line P2) give wrong results. Penalty method with a relative low penalty coefficient (line P1) gives the same results with matched meshes. This is a reasonable phenomenon and verifies the conclusion we gave in the first example.

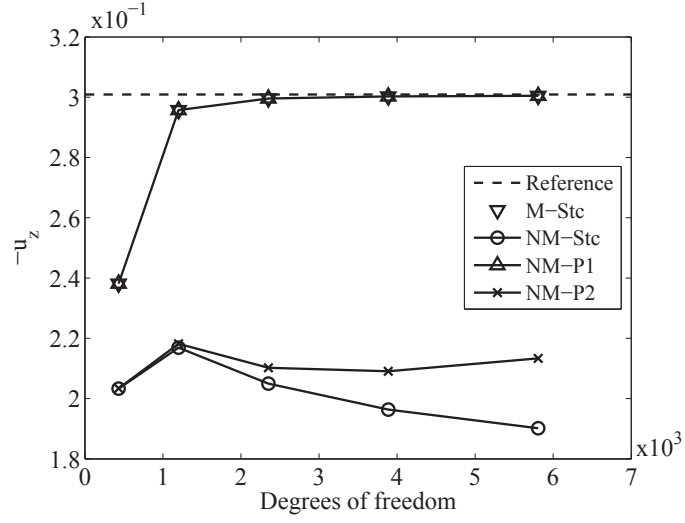


Figure 4.12: Scordelis-Lo roof problem: u_z at point C varies with h refinements. “NM” indicates non-matching meshes. Other notations’ meanings are the same with those in figure 4.11.

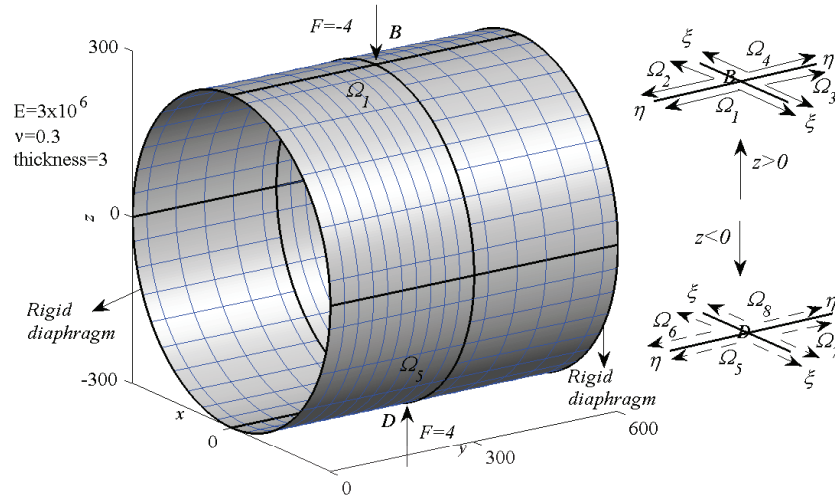


Figure 4.13: Pinched cylinder problem setup. It also shows a hierarchical meshes case.

Pinched cylinder problem

Figure 4.13 shows the pinched cylinder problem setup. It composes 8 patches and is analyzed with the cubic KL elements. The patch layout of the upper part of the structure ($\Omega_i, i = 1 \sim 4$) is the same to the Scordelis-Lo roof, and so is the mesh creation rule. Here, considering the calculation cost, we use $N = \{4, 8, 12, 16\}$ in the matching case and non-matching case, and $N = \{4, 10, 16, 22\}$ in the hierarchical case. The lower part of the structure ($\Omega_i, i = 5 \sim 8$) is symmetric with the upper part with the plane $z = 0$.

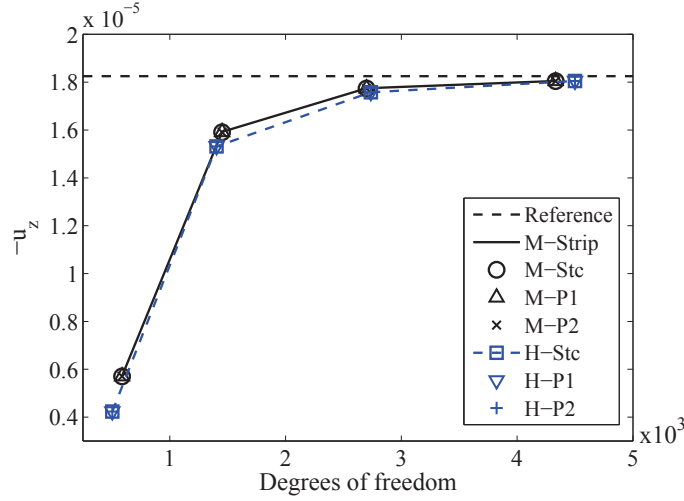


Figure 4.14: Pinched cylinder problem: u_z at point B varies with h refinement. “P1” and “P2” indicate penalty method with penalty coefficients 10^9 and 10^{14} . Other notations’ meanings are the same with these in the former example.

Figure 4.14 shows the u_z at point B from matching meshes and hierarchical meshes. The reference is set as 1.8248×10^{-5} got from [19, 86]. In matching meshes, all the results coincide with each other and with those from bending strip method [87]. In the hierarchical case, all results coincide with each other.

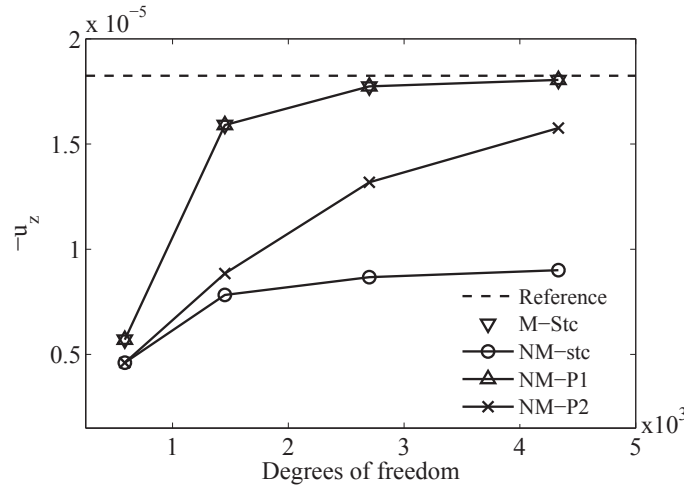


Figure 4.15: Pinched cylinder problem: u_z at point B varies with h refinement.

Figure 4.15 shows the u_z from non-matching meshes. The penalty method with a relative smaller penalty coefficient (line P1) gives the same results with these from matching meshes case. Static condensation method and penalty method with a relative larger penalty coefficient (line P2) give wrong results. This is the same with that in the former example.

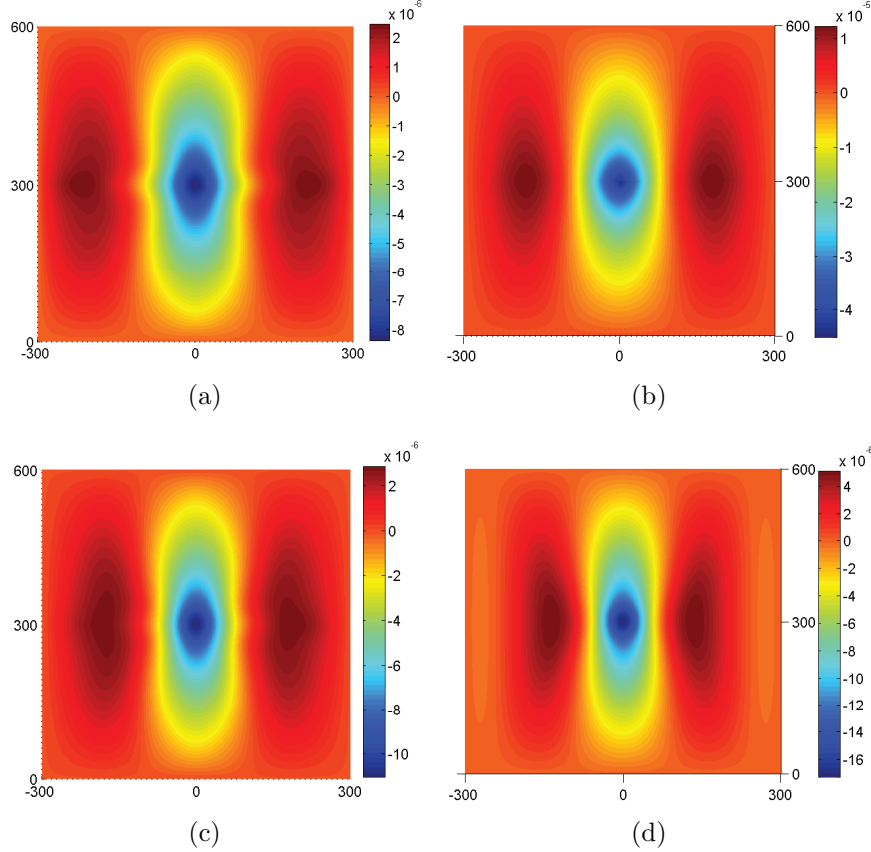


Figure 4.16: Pinched cylinder problem: u_z contour plots (only upper part) from non-matching meshes ($N = 10$). Results from static condensation method (a) and penalty method with various penalty coefficients: (b) 10^6 , (c) 10^{16} , (d) 10^9 .

Figure 4.16 shows the u_z from the upper part of the cylinder with non-matching meshes. The mesh creation rule has been mentioned in the second example with $N = 10$ here. The results are from static condensation method and penalty method with different penalty coefficients: 10^6 , 10^9 and 10^{16} . It can be seen that when using penalty method with a low penalty coefficient, the continuity condition may be too weakly imposed, discontinuity might appear, see the center of figure 4.16(b). When using a too large penalty coefficient, the continuity condition will be too strongly imposed; the common function space will shrink, the result approaches that from the static condensation method and is not acceptable, see figure 4.16(c) and 4.16(a). When a proper penalty coefficient is chosen, it will enlarge the common space and give reasonable result, see figure 4.16(d).

4.1.4 Discussion

We give a method that is capable of connecting multiple patches with C^0/G^1 continuity in the IGA analysis. The patches to be connected should initially possess the required continuity. The continuity condition given here can maintain the required continuity between deformed patches. In matching or hierarchical meshes, incorporating the continuity condition with static condensation method or penalty method will work. In the non-matching meshes, only penalty method with a proper penalty coefficient is applicable.

We also study the cause of the above phenomena. The solution of the equation on the common boundaries is approximated by the intersection of the related function spaces. The larger it is, the better the solution is. In IGA analysis, matching or hierarchical meshes give embedded spaces on the edge in related patches, that is, one space is the subspace of the other. Their intersection will be the smaller one. When the function space increases (mesh refinement), the common space will become larger, and the solution will become better. But in the non-matching meshes case, there is no embedded space structure. The size of the intersect space is unguaranteed. When we enrich each related space, there is a possibility that the common space will not increase. Incorporating the constraints with the weakly imposing method can solve this problem. It will give a proper tolerance to common space, so the functions that are “near” can be included and the common space is enlarged, so that the approximation accuracy will be improved. Briefly speaking, the unbalance of the function spaces is the root of this problem.

Some suggestions for mesh creation in IGA multiple patch analysis can be obtained from the examples. It is better to create the meshes in matching or hierarchical form, since they will give embedded function space structure and the solutions will be well approximated. If you use non-matching meshes, the common space should be enlarged by using weak enforcement methods.

4.2 Isogeometric modal synthesis

The modal synthesis method is frequently used for the analysis of large structures composed of multiple parts concerning dynamic aspects. In this section, we extended the modal synthesis method under the isogeometric analysis framework. The isogeometric Kirchhoff-Love shell elements are used for the analysis of the substructures, the Craig-Bampton method is used for the modal synthesis. The patches coupling is key problem in IGA based modal synthesis, those methods introduced in the previous section could be used here. We give examples on the modal analysis and the harmonic response analysis.

The modal synthesis method is a method used for the analysis of built-up structures concerning dynamic aspects. It is also mentioned as component modal analysis or branch mode analysis. The full structure is partitioned into some substructures, the substructures

control equations are simplified by transforming the physical degrees of freedom into mode coordinates and then coupling with each other according to the interface compatibility. Compared with the static condensation method (Guyan method) [69] which is frequently used in the model reduction for static analysis, the modal synthesis method can give more exact results for the analysis concerning dynamic aspects due to the incorporation of inner node dynamics [72]. The decentralization property of the modal synthesis method enables a distributed computing, a cheap local parameter study and a proper allocation of tasks between different teams, which makes it attractive for the industry.

The modal synthesis method can be divided into three categories by the boundary conditions on the interface: the fixed interface method [11, 81], the free interface method [41, 74] and the hybrid interface method [83, 84, 93]. Comparisons among those three types of methods can be found in Curnier [44]. We focus on a fixed interface modal synthesis method, Craig-Bampton method [11]. Hurty developed and recommended this method as the most trustful method for all vibration analyses [82]. Bampton and Craig [11] then simplified it by treating rigid-body modes as a special case of constraint modes, and our present work is based on this Craig-Bampton method. Some reviews on the modal synthesis method can be found in papers [42, 43, 89].

IGA method shows promise in bridging the gap between the CAD and the CAE. It brings a potential power in the structure optimization and the geometric parameter study. The exact geometrical map provides an explicit link between the parametric domain and the physical domain. The analytical parameter sensitivity can thus be obtained [33, 106]. The IGA refinement is achieved by the knot insertion or order elevation of the initial geometry [79]. Tracing back to the CAD model is no longer needed. It costs far less time than the FEM. This is a huge advantage for the structure optimization, where massive mesh refinements and adjustments are needed during the iterations. As for the local parameter study or optimization concerning dynamics, where the concerning parameters only relate to certain substructures, it is more economical to only remesh the corresponding substructures. The motivation of the present work is to extend the modal synthesis method under the isogeometric framework for efficient analysis concerning dynamic aspects. It will lay a foundation for the efficient local parameter study and optimization.

4.2.1 The Craig-Bampton method

The structure control equation that includes the inertial force and damping is

$$\mathbf{M}\ddot{\mathbf{u}} + \mathbf{C}\dot{\mathbf{u}} + \mathbf{K}\mathbf{u} = \mathbf{F}. \quad (4.29)$$

\mathbf{M} denotes the mass matrix, it is obtained by condensing mass to the shell middle surface, and treating them as the inertial force. \mathbf{C} denotes the damping matrix.

4. STRUCTURAL ANALYSIS WITH IGA ON MULTIPLE DOMAINS

For harmonic response analysis, equation (18) is written as

$$(-w^2 \mathbf{M} + jw \mathbf{C} + \mathbf{K}) \mathbf{u} = \mathbf{F}. \quad (4.30)$$

Here, w is the angular frequency with $w = 2\pi f$. f is the frequency of the excitation. \mathbf{C} is damping matrix. If Rayleigh damping is used, $\mathbf{C} = a\mathbf{M} + \beta\mathbf{K}$. In modal analysis, there will be no damping or loads, equation (4.30) will be a generalized eigenvalue problem as following:

$$(-w^2 \mathbf{M} + \mathbf{K}) \mathbf{u} = \mathbf{0} \quad (4.31)$$

For large structures composed of multiple parts, the control equations (4.30) (4.31) can be simplified by modal synthesis method to reduce the dimension. With a linear map \mathbf{T} , the equation (4.30) is simplified as

$$\mathbf{T}^T (-w^2 \mathbf{M} + jw \mathbf{C} + \mathbf{K}) \mathbf{T} \mathbf{u} = \mathbf{T}^T \mathbf{F}. \quad (4.32)$$

\mathbf{T} is a product of two parts \mathbf{T}_s and \mathbf{T}_c , \mathbf{T}_s is used for the separated substructure reduction and \mathbf{T}_c for the simplified substructures coupling. The key of the modal synthesis is the construction of \mathbf{T}_s and \mathbf{T}_c .

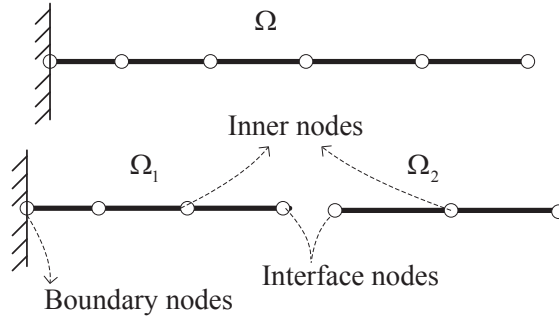


Figure 4.17: A full structure with two substructures and their nodes.

Figure 4.17 shows a full structure (a beam) which is partitioned into two substructures and their nodes. The boundary nodes are the nodes on which the Dirichlet boundary condition is imposed, the interface nodes are the nodes by which the two substructures connected with each other, the remaining ones are the inner nodes.

The discrete control equation for a substructure Ω^s with harmonic loads is

$$\left\{ -w^2 \begin{bmatrix} \mathbf{M}_{ii}^s & \mathbf{M}_{ib}^s \\ \mathbf{M}_{bi}^s & \mathbf{M}_{bb}^s \end{bmatrix} + jw \mathbf{C} + \begin{bmatrix} \mathbf{K}_{ii}^s & \mathbf{K}_{ib}^s \\ \mathbf{K}_{bi}^s & \mathbf{K}_{bb}^s \end{bmatrix} \right\} \begin{Bmatrix} \mathbf{u}_i^s \\ \mathbf{u}_b^s \end{Bmatrix} = \begin{Bmatrix} \mathbf{F}_i^s \\ \mathbf{F}_b^s \end{Bmatrix}. \quad (4.33)$$

Here, i indicates the inner control points and b indicate the interface control points. Equation (4.33) is the control equation after imposing the initial Dirichlet boundary condition.

The Craig-Bampton method uses the selected fixed interface modes and the constraints modes to simplify it. The transformation matrix for substructure t is

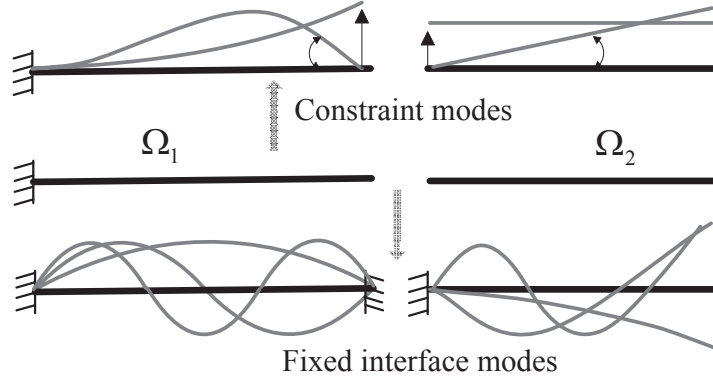


Figure 4.18: A schematic about the substructure modes.

$$\mathbf{T}_s^t = [\Phi_N^t, \Phi_c^t]. \quad (4.34)$$

Here, $\Phi_N^t = \{\phi_1^t, \phi_2^t, \dots, \phi_k^t\}$, ϕ_r^t indicates the r^{th} eigenvector of substructure t with all interface degrees of freedom constrained. It is obtained by a preliminary modal analysis of the substructures. Only the first k eigenvectors are selected. Φ_c^t denotes the constraint mode which is the displacement obtained by applying a unit displacement on each interface degree of freedom and keeping others fully constrained. Figure 4.18 gives a schematic of those modes.

$$\Phi_c^t = \begin{bmatrix} -(K_{ii}^s)^{-1} K_{ib}^s \\ \mathbf{I} \end{bmatrix} \quad (4.35)$$

The condensed substructure equation now can be obtained as

$$(\mathbf{T}_s^t)^T (-w^2 \mathbf{M} + jw \mathbf{C} + \mathbf{K}) (\mathbf{T}_s^t) \mathbf{u} = (\mathbf{T}_s^t)^T \mathbf{F}. \quad (4.36)$$

The simplified substructure model can be viewed as a macro element which only possesses interface degrees of freedom and the inner hanging nodes' degree of freedom. The inner node's dynamics is now approximately considered by the interface degrees of freedom.

4.2.2 Multiple domains coupling

The interface degrees of freedom are kept unchanged during the modal reduction, these interface degrees of freedom from adjacent patches should be connected. Figure 4.19(a) shows two shell substructures and their interface control points. It is worth mentioning that there are no rotational degrees of freedom in the IGA Kirchhoff-Love shell, in order

4. STRUCTURAL ANALYSIS WITH IGA ON MULTIPLE DOMAINS

to transfer the moments between adjacent substructures, the second row of control points should also be viewed as interface nodes. In the case where the substructures are only C^0 connected, which means they can rotate with respect to the interface, only the control points on the interface are treated as interface nodes.

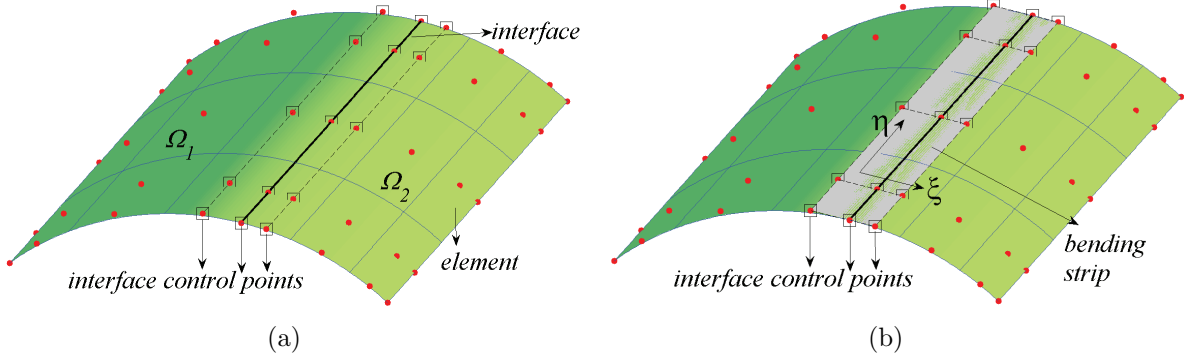


Figure 4.19: The shell substructure and interface control points (a), the bending strip for the substructures coupling (b).

The full structure equation can be obtained by stacking the separated simplified substructure control equation together and then connecting the substructures by the interface degrees of freedom. In the present work, the bending strip method [87] is used. The bending strip is a virtual material layer which only transfers the moments between adjacent substructures. It is modeled by the quadratic NURBS surface with the interface control points. Figure 4.19(b) shows the construction of the bending-strip on the interface. Its material laws are

$$\begin{bmatrix} m^{\xi\xi} \\ m^{\eta\eta} \\ m^{\xi\eta} \end{bmatrix} = h \begin{bmatrix} E_{strip} & 0 & 0 \\ 0 & 0 & 0 \\ 0 & 0 & 0 \end{bmatrix} \begin{bmatrix} \kappa_{\xi\xi} \\ \kappa_{\eta\eta} \\ 2\kappa_{\xi\eta} \end{bmatrix}. \quad (4.37)$$

Here, E_{strip} dominates the rotational coupling stiffness, h is the thickness of the shell. The angle between substructures will be exactly kept as E_{strip} approaches infinity. In applications, $E_{strip} = 10^5 E$ will be a proper choice [87]. With the substructures reduction and coupling, equation (4.30) (4.31) can be simplified with fewer degrees of freedom. The details of the implementation are in the appendix.

4.2.3 Numerical examples

We give examples on modal analysis and harmonic response analysis. The structures are modeled by the Kirchhoff-Love shell and partitioned into a few substructures. The quantities used in the examples are all dimensionless.

L-shape shell modal analysis

Figure 4.20 shows the problem setup. It is partitioned into two substructures. There is a 90° kinks between them. The two substructures are solidly connected. Each substructure is uniformly meshed with 20×10 elements, see figure (a). The control points of the structure are shown in figure (b).

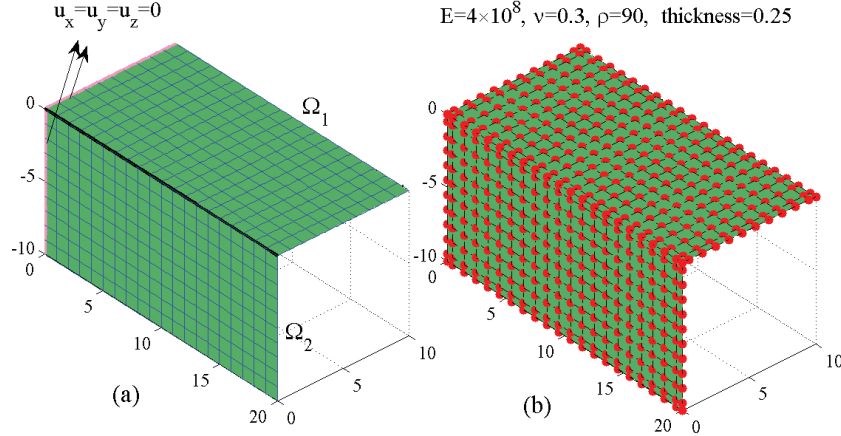


Figure 4.20: L-shape shell problem setup, the elements (a) and the control points (b).

The substructures are connected using the bending strip method. According to the empirical rule that the selected substructure fixed interface frequencies should be two times larger than those expecting from the full structure, we selected each substructure's first twenty fixed interface modes. Each substructure's degrees of freedom are reduced from 792 to 146. Figure 4.21 shows the first twenty frequencies obtained from the modal synthesis and the full structure analysis. The error comes from the truncation of the fixed interface modes. Figure 4.22 shows the relative error when different numbers of fixed interface modes are selected. The errors decrease with an increase in the number of fixed interface modes.

Figure 4.23 shows some modal shapes from the full structure analysis and the modal synthesis method. They fit well with each other. It can be seen that the angle between the substructures are well kept with the help of the bending strip.

Curved shell modal analysis

Figure 4.24(a) shows the problem setup and the material properties. The structure is uniformly partitioned into four substructures. Each substructure is meshed uniformly with 12×12 elements, see figure 4.24(b).

Figure 4.25 shows the natural frequencies obtained from the modal synthesis and the full structure analysis. The full structure is uniformly meshed with 24×24 elements. Each substructure's first ten fixed interface modes are kept. They are selected according to the empirical rule that the selected substructure fixed interface frequencies should be

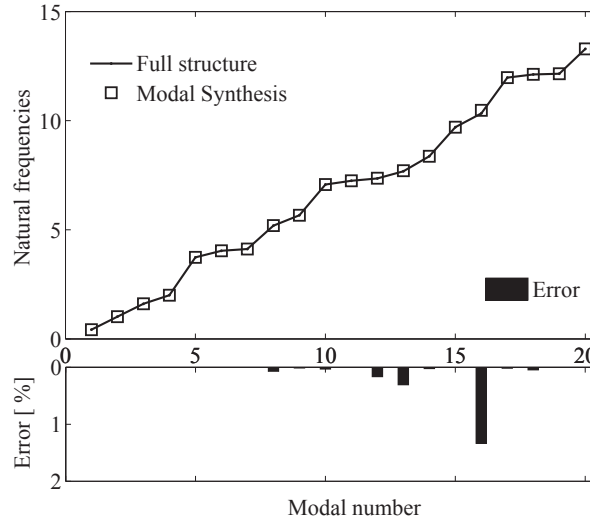


Figure 4.21: L-shape shell, the natural frequencies obtained from the modal synthesis and the full structure analysis.

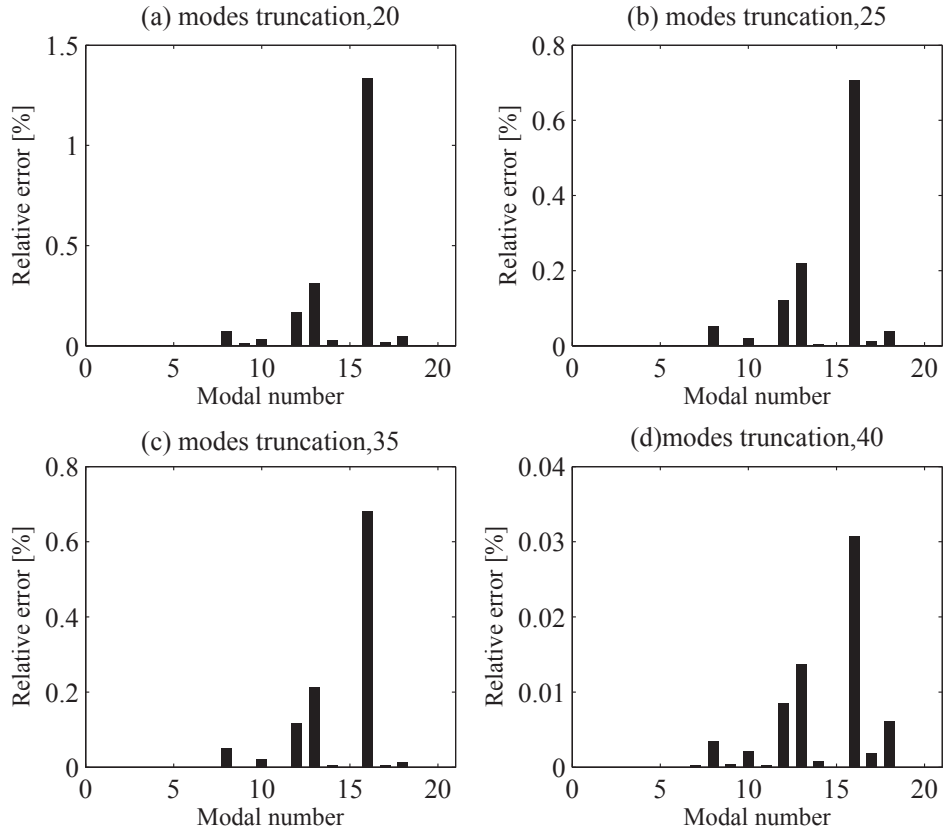


Figure 4.22: L-shape shell, the relative errors between the full structure analysis and the modal synthesis with different number of fixed interface modes: (a)20, (b)25, (c)35, (d)40.

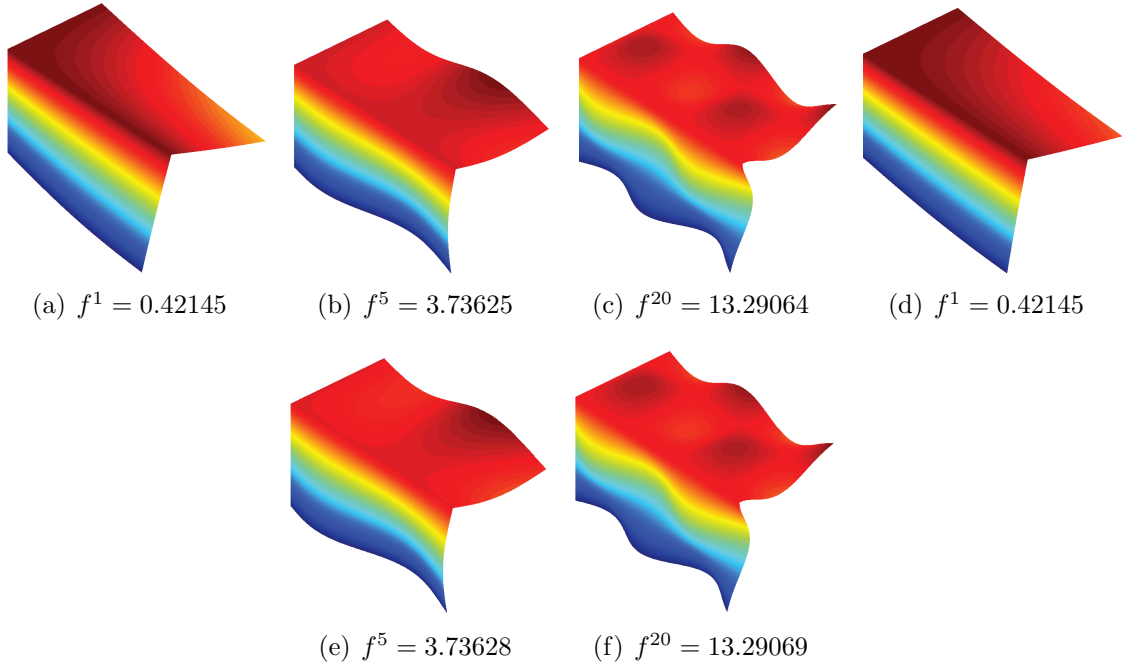


Figure 4.23: L-shape shell, some modal shapes from the full structure analysis ($a \sim c$) and the modal synthesis ($d \sim f$).

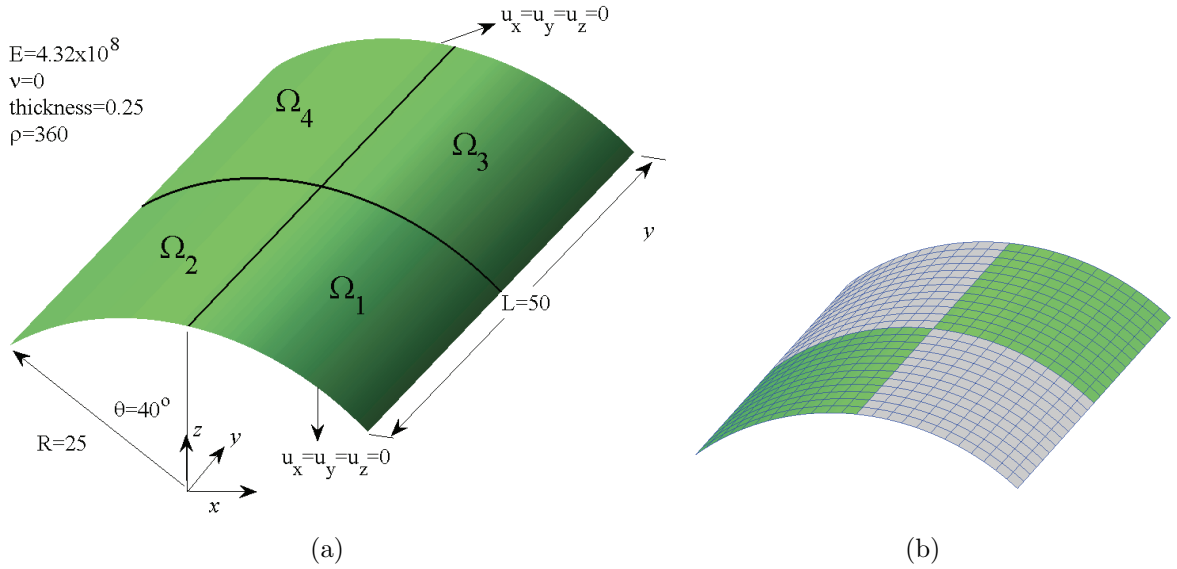


Figure 4.24: The curved shell problem setup, the material properties (a) and the meshes (b).

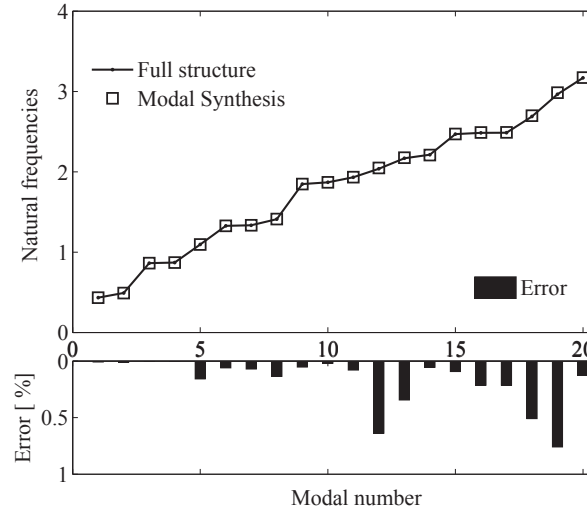


Figure 4.25: The curved shell, the natural frequencies obtained from the modal synthesis and the full structure analysis

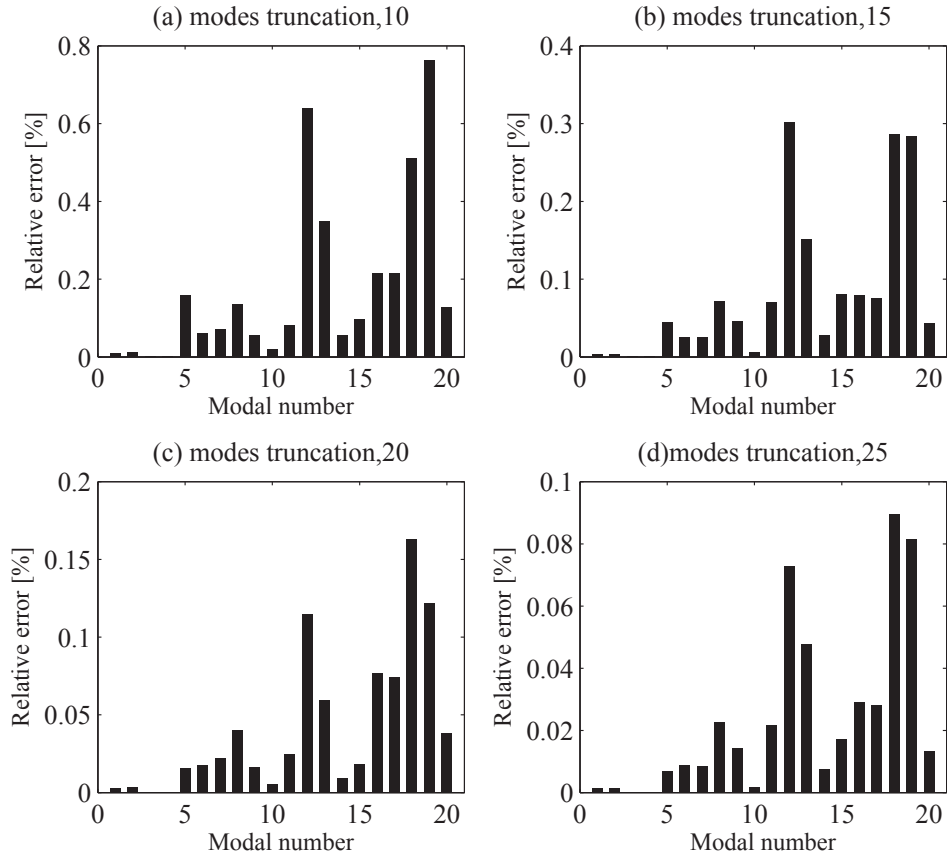


Figure 4.26: The curved shell, the relative errors between the full structure analysis and the modal synthesis with different number of fixed interface modes: (a)10, (b)15, (c)20, and (d)25.

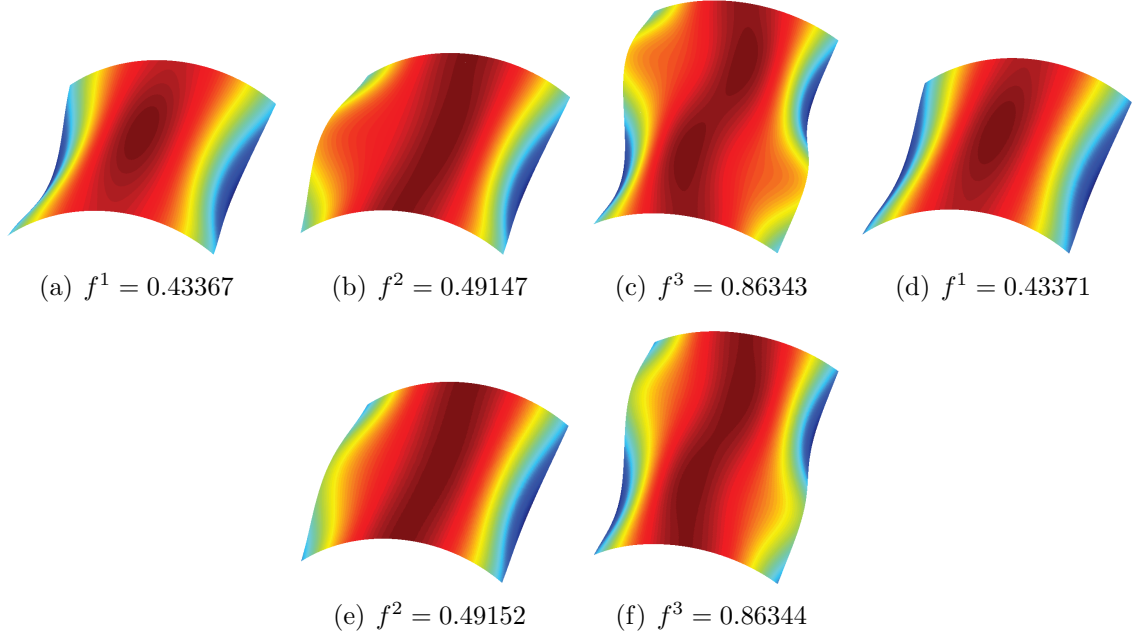


Figure 4.27: The curved shell, the first three modal shapes from the full structure analysis ($a \sim c$) and the modal synthesis ($d \sim f$).

two times larger than those expecting from the full structure. After model reduction, each substructure's degrees of freedom are reduced from 588 to 160. The relative error between the results is also showed at the bottom of the figure. The error comes from the truncation of the substructure modes. It will decrease when more fixed interface modes are selected, see figure 4.26. Figure 4.27 shows the first three modal shapes from the full structure analysis ($a \sim c$) and the modal synthesis ($d \sim f$), they fit with each other well.

Harmonic response analysis

The problem setup and the substructures separation is the same as in the previous example. Figure 4.28 shows the structure mesh. The harmonic excitation is applied at control point L. We will scan the frequencies in the interval $[0.4, 0.9]$ with 180 sample points. The Rayleigh damping is used with the coefficients $\alpha = 0.0035$ and $\beta = 2.4485 \times 10^{-4}$. We will observe the displacement at control point M.

We analyze the model with the full structure analysis and the modal synthesis method. In full structure analysis, the structure is also composed of four patches; a patch connection should also be conducted. We use the bending strip method to connect the patches in both cases.

Figure 4.29 shows the amplitude of the displacement response components u_z at the control point M. The results from the full structure analysis and the component modal synthesis are both depicted. Good accordance can be observed. The resonant frequencies are also marked. They are 0.4338, 0.4914, 0.8637, and 0.8699. The first four natural frequencies obtained from the full structure model analysis are 0.4337, 0.4915, 0.8634,

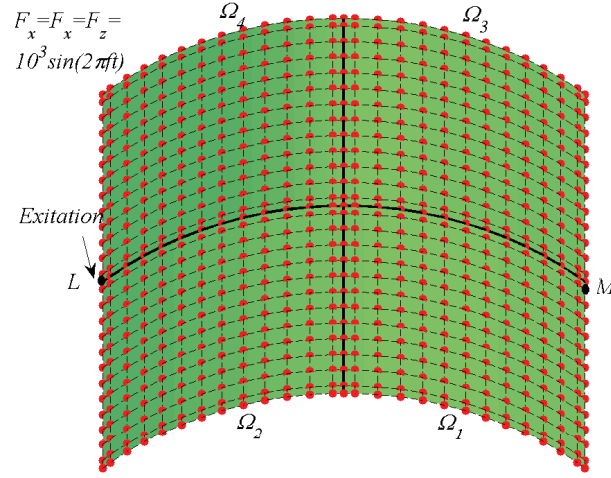


Figure 4.28: The structure mesh and the excitation.

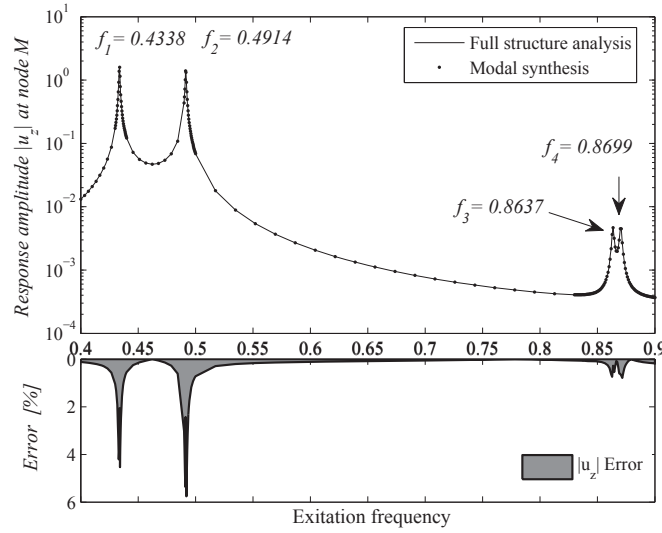


Figure 4.29: The response amplitude $|u_z|$ at control point M from the modal synthesis and full structure analysis

Table 4.2: The number of degrees of freedom and time costs in the harmonic response analysis. The “time” denotes the total time used for solving the structure equation in all sample points. The “modes” denote the “fixed interface modes”.

	Full structure	10 modes	15 modes	20 modes	25 modes
DOFs	2025	481	501	521	541
Time [s]	523.725	11.243	12.634	14.057	16.425

and 0.8703. They fit well with each other. Figure 4.30 shows the u_z relative errors from the modal synthesis with different numbers of substructure fixed interface modes. It can be seen that the error decreases when more fixed interface modes are selected, see figure 4.30. The errors close to the resonance frequencies are larger. It is due to that the response is more sensitive in those regions.

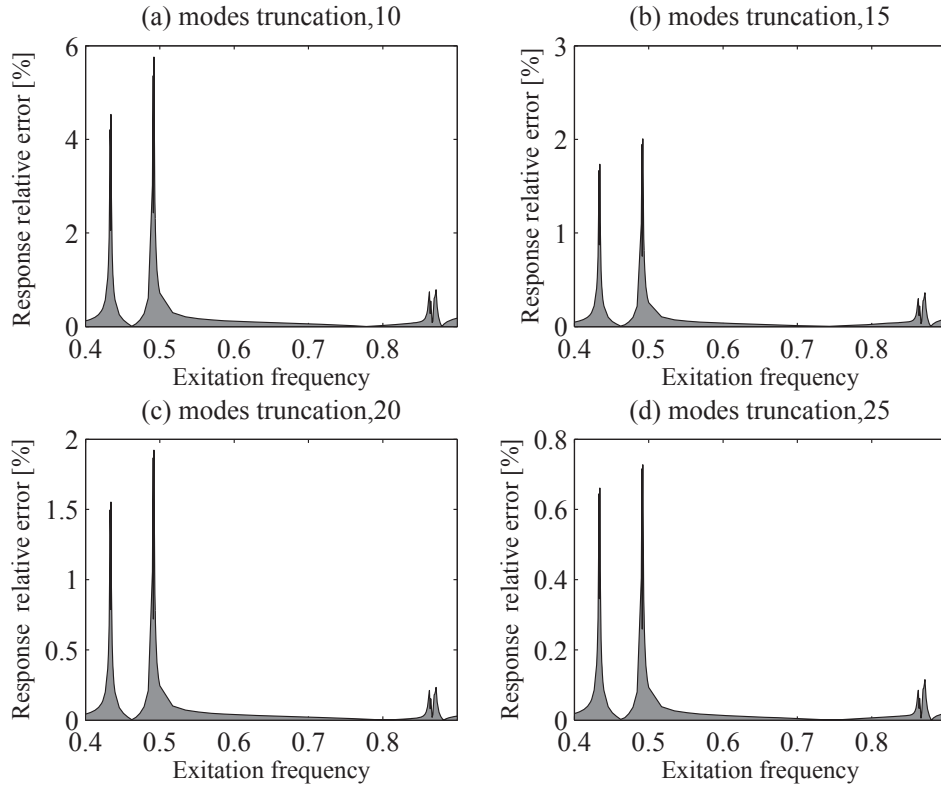


Figure 4.30: The response amplitude $|u_z|$ error between the full structure analysis and the modal synthesis with different number of fixed interface modes: (a) 10, (b) 15, (c) 20 and (d) 25.

Table 4.2 shows the structure degrees of freedom and the time costs in the full structure analysis and the modal synthesis method with different number of fixed interface modes. The CPU of the computer is Intel Core i5-3210M 2.5GHz, the RAM is 4G. The time cost here refers to the total time used for solving the linear equations in all 180 frequency sample points. The time taken for the substructure modal analysis is $0.1 \sim 0.3s$, it is far shorter than the time used for solving the structural equation. Large savings in the

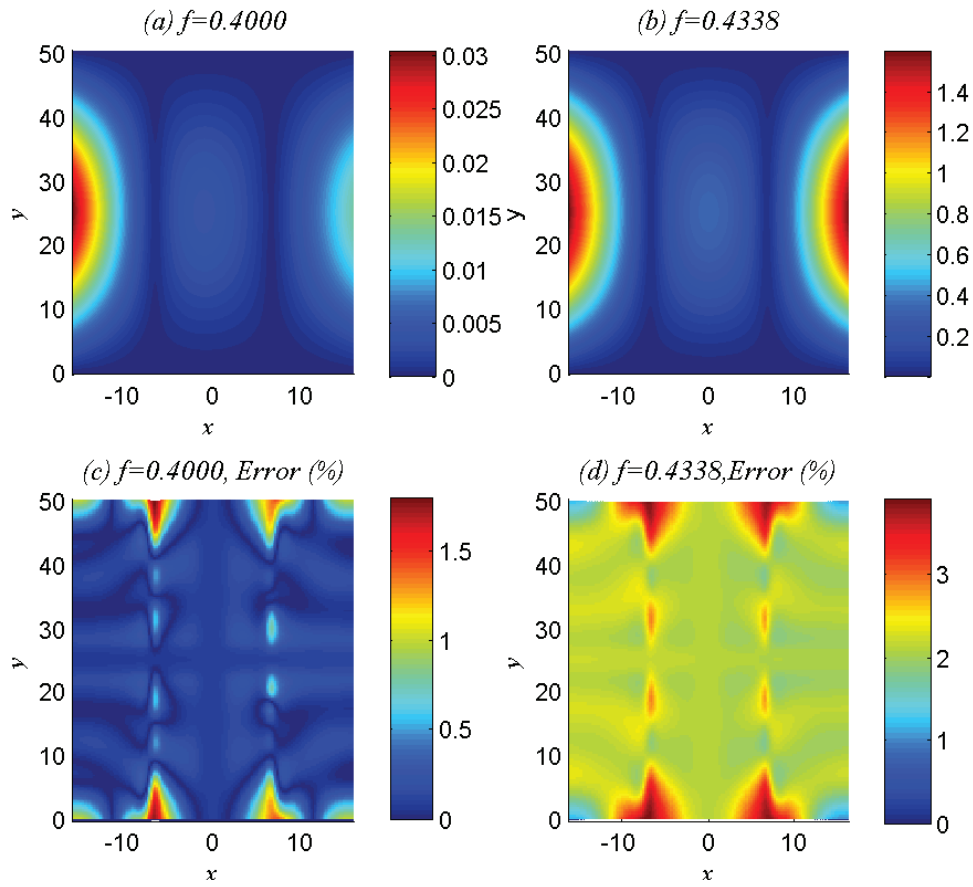


Figure 4.31: The response amplitude $|u_z|$ obtained from the modal synthesis at frequencies 0.4 (a) and 0.4338 (b) and their relative errors with full structure analysis (c) (d)

degrees of freedom and time expense can be found with the modal synthesis method.

Figure 4.31 shows the structure response amplitude $|u_z|$ at frequencies 0.4, 0.4338 obtained from the modal synthesis method. Their relative errors with the full structure analysis is also showed here. It can be seen that when excitation approaching the natural frequencies the overall vibration amplitude is much larger than other cases.

4.2.4 Discussion

In this section, we implemented the modal synthesis with the IGA Kirchhoff-Love shell elements for modal analysis and harmonic response analysis. The results show the effectiveness of the method. All the advantages that the modal synthesis method brings us under the traditional FEM framework now can also be enjoyed in the IGA analysis. The method can be potentially used for the study or optimization of local parameters which only relates to certain parts of the structure, the computational savings are attractive in those applications.

4.3 Summary

In this chapter, we studied the multiple patches coupling problem in IGA analysis. A new patches coupling method is proposed, results show its effectiveness. The modal synthesis method with isogeometric shell elements is also detailed. We will use it in the next chapter to implement the structural optimization for built-up structures where the design variables only relate to certain substructures. During the design iteration, only the relevant parts will be reanalyzed. It will reduce the computational costs.

Chapter 5

Shape optimization

In this chapter, we will present a framework for fast parametric shape optimization. The geometrically exact NURBS based isogeometric Kirchhoff-Love shell elements are used to model such parts. The dynamics criteria are considered. The previously introduced modal synthesis method are used to avoid a repeated evaluation of some substructures where there are no designed variables defined. Another emphasis is on the design sensitivities analysis. We give a sensitivity mapping method to evaluate the design sensitivities. The element-level analytical sensitivity with respect to the intrinsic shape parameters is firstly calculated, from which the design sensitivity is then extracted with the help of a sensitivity map. This framework is efficient for massive design variables optimization problem. Meanwhile, with the IGA method, the optimum structure will be a CAD model, which is more manufacturable.

5.1 Introduction on the IGA based shape optimization

In engineering structural optimization, model reanalysis is an indispensable step. Its efficiency greatly affects the overall efficiency. In the traditional FEM based optimization framework, the fixing of CAD model and creating FEM model account for 80% of overall analysis time cost [37]. With IGA analysis, large saving can be expected in this part, since the mesh refinements no longer need tracing back to the CAD model and are easy to implement [39]. Another advantage that IGA based optimization brings is the manufacturability of the optimum structure, since the optimum shape will be a CAD model rather than a geometry expressed by facets.

IGA provides an explicit map between the parametric domain and the physical domain, the element-level analytical sensitivity of the structural equation ingredients, e.g. stiffness matrix and mass matrix, can thus be obtained [96, 97, 106, 134]. The mesh creation algorithm also establishes maps between the different meshes of the same model, the

5. SHAPE OPTIMIZATION

sensitivity of the fine meshed analysis model can be transferred into the coarse meshed model [97]. This allows an exact model analysis as well as a proper design variable definition. In our work, we generalize the design variables. The design variables could be any combination of the bottom mesh-level nodes (control points in IGA) movement. Since any modification of the design variable will lead to a model movement, and it is finally reflected (or approximated) by the movements of the nodes. The design sensitivities can thus be obtained by retracing with this map. One might think that the similar idea can also be used in the FEM framework, however there is no explicit link between the geometry and the mesh there, which will make the sensitivity retracing impossible. The high efficiency, the exact and efficient sensitivity analysis, the manufacturability of the optimum shape, they constitutes the main reasons to choose IGA based optimization.

The modal synthesis method is a traditional method used for analyzing the built-up structures concerning dynamics aspects. With modal synthesis, the dimension of the problem will be reduced. For some optimization problem concerning structural dynamics aspects, the design variables might only relate to several substructures, it is more computational economical to only reanalyze the corresponding substructures. Modal synthesis is needed in such case. In the present work, we also take advantage of this character to develop a fast optimization framework for structures composed of many substructures.

We have given a general introduction about the optimization problems in the first chapter of the thesis. Our focus is the shape optimization problem. There are two types of shape optimization problem. They are the free form optimization problem and the boundary optimization problem. They are distinguished from each other by the relationship between the analysis domain and the optimization domain. For free shape optimization problem, the analysis domain is the optimization domain. For boundary optimization problem, the design is only the boundary of the domain. In such case, a link should be established to relate the variation of the boundary to the variation of the domain in the boundary optimization problem. Normally, plane elements are adopted for analysis. Our focus is the free shape optimization, it is more applicable for engineering applications.

A theoretical and general description of shape optimization under partial differential equation (PDE) constraints can be found in paper [128]. For structural optimization, the PDE will be the structural equation. A good review of IGA based structural optimization can be found in paper [101]. We are more inclined to present our method as well as the indispensable theoretical content. We will detail it through a structural fundamental frequency maximization problem. However, it does not restrict our approach in such a case.

The problem is formulated as

$$\begin{aligned}
 & \text{find } \mathbf{z} = [z_1, z_2, \dots, z_i] \\
 & \text{maximize } \lambda_1(\mathbf{z}) \\
 & \text{s.t. } m(\mathbf{z}) \leq m_d \\
 & \begin{cases} \mathbf{K}(\mathbf{z}) \mathbf{u}_1 = \lambda_1 \mathbf{M}(\mathbf{z}) \mathbf{u}_1 \\ \mathbf{u}_1^T \mathbf{M} \mathbf{u}_1 = 1 \\ \mathbf{u}_1^T \mathbf{K} \mathbf{u}_1 = \lambda_1 \end{cases}
 \end{aligned} \tag{5.1}$$

Here, \mathbf{z} is the design variable vector. λ_1 is the first eigenvalue, it relates to the fundamental natural frequency with $\lambda_1 = (2\pi f_1)^2$. \mathbf{u}_1 is the corresponding eigenvector. m denotes the structure mass, $m = \frac{1}{3} \text{sum}(\mathbf{M})$. m_d is the user defined maximum mass, here we set it as 3000.

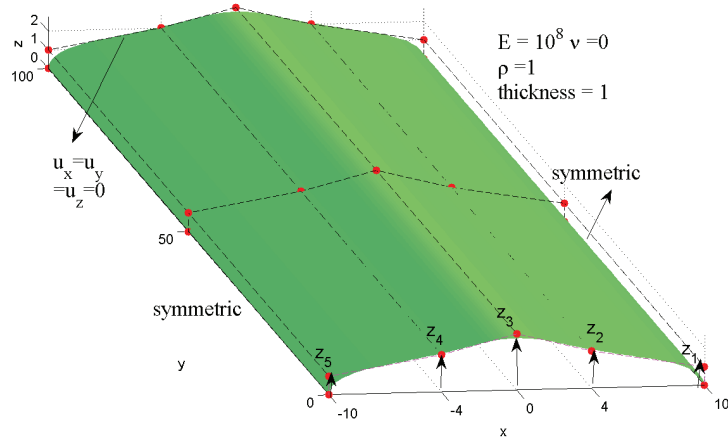


Figure 5.1: Initial structure setup and design parameters.

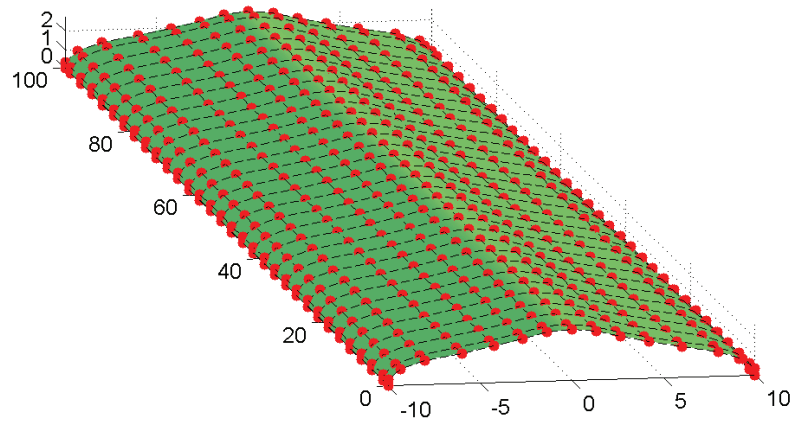


Figure 5.2: The fine meshed analysis model.

Figure 5.1 shows the initial structure, $\mathbf{z}_0 = [1, 2, 3, 2, 1]$. It is extruded by the profile. The structural boundary condition and the material properties are also shown there. They

5. SHAPE OPTIMIZATION

are all dimensionless. The structure is analysed with IGA Kirchhoff-Love shell elements. The design variables are the z coordinates of a certain control points of the profile.

5.2 Sensitivity analysis

We chose gradient based optimization algorithm. The design sensitivity should be evaluated. There are many methods to obtain the sensitivity, e.g. finite difference method(FDM), analytical method, semi-analytical method, continuum method. A good review of those methods can be found in paper [34, 131]. They are the basic concepts in structural optimization. The FDM evaluates the sensitivity directly from the gradient definition. It is the easiest way to obtain the design sensitivity, however, it is neither efficient nor accurate. The analytical sensitivity evaluates the sensitivity by successively differentiating the formulations, it is thus accurate, however it needs profound understanding of the cost function formulations, which are normally cumbersome in real engineering optimization. There are two types of method in this category, continuum based method and discrete based method. The continuum based method could make the evaluation of the sensitivity independent from that of the cost function, it enables the user use the commercial software at the same time obtain the sensitivity by a independent sensitivity subroutine. The discrete sensitivity analysis has a clearer concept, the sensitivity evaluation is based on the derivatives of the discrete form equation. As for the semi-sensitivity analysis, it is a compromise between the analytical method and the FDM.

We choose discrete adjoint method to evaluate the design sensitivity. Since the structural analysis routine is coded by us, it will be more convenient and efficient to include the sensitivity part in the same routine. The sensitivities of the objective function and constraint are needed. We design a sensitivity mapping method to exact the sensitivity from the bottom mesh level sensitivity. Those bottom mesh level sensitivity are obtained from the analysis model, where all the control point positions are considered as design variables. This strategy takes into account both the variable definition and the mechanical analysis.

The cost function gradients for the above problem are

$$\lambda_{1,z_i} = \mathbf{u}_1^T (\mathbf{M}_{,z_i} - \lambda_1 \mathbf{K}_{,z_i}) \mathbf{u}_1 \quad (5.2)$$

$$m_{,z_i} = \frac{1}{3} \text{sum}(\mathbf{M}_{,z_i}). \quad (5.3)$$

5.2.1 Element level sensitivity analysis

The analysis model is shown in figure 5.2, it possesses more degrees of freedom to ensure a reasonable structural response evaluation. In the element level, all the control point

positions are considered as design variables. It assembles the traditional FEM mesh based optimization, where all the node positions are taken as design variables. For i th control point, its perturbed position is

$$\mathbf{p}^i = \mathbf{p}^i + \mathbf{s}^i. \quad (5.4)$$

Here, $\mathbf{p}^i = [p_x^i, p_y^i, p_z^i]^T$ is the i th control point's initial position. $\mathbf{s}^i = [s_x^i, s_y^i, s_z^i]^T$ is the perturbation. The design gradient with respect to s_-^i is concluded into the evaluation of $\mathbf{M}_{,s_-^i}$ and $\mathbf{K}_{,s_-^i}$.

$$M_{ij,s_-^i} = \frac{\partial \int_{S(s_-^i)} \rho N_i N_j dS(s_-^i)}{\partial s_-^i} \quad (5.5)$$

$$K_{lm,s_-^i} = \frac{\partial \delta \Pi_{\text{int}}(s_-^i)}{\partial \delta u_l \partial u_m \partial s_-^i} \quad (5.6)$$

The basic ingredients are $\mathbf{S}_{,s_-^i}(s_-^i)$, $\mathbf{S}_{\alpha,s_-^i}(s_-^i)$ and $\mathbf{S}_{\alpha\beta,s_-^i}(s_-^i)$. The above deduction somewhat assembles the continuum sensitivity analysis [34]. The design variables' NURBS interpolation can be viewed as a single design field, which is the start point of the continuum sensitivity analysis. However, as all the functional analysis, the functional should be in the end expanded in a space, the evaluations are finally concluded into the discrete scalar operations. For the same mesh level defined design variables, the two methods are equivalent [7], although their procedures are different. The complexity of analytical sensitivity analysis is to some extent decided by the complexity of the PDE used, no matter discrete or continuum method are used. Some continuum adjoin sensitivity analysis examples with IGA can be found in paper [33, 137]. Wall et al. [134] and Qian [106] gave a general description about the evaluation of IGA structural ingredients' sensitivity with respect to control points and weight respectively, they use plane stress elements. Nagy et al. [97] use the same element with the present work, one can also find a description there. The essential operation is the successively differentiating of the structural ingredients.

The element-level cost functions sensitivities are obtained with equation (5.2) and (5.3), they are noted as \mathbf{g}_λ^f and \mathbf{g}_m^f , they can be directly used to implement the element level parameter optimization. Figure 5.3 shows the sensitivity of the objective function with respect to the z coordinates of the movable control points of the fine meshed initial configuration ($\mathbf{z}_0 = [1, 2, 3, 2, 1]$), there are 480 mesh level design variables.

5.2.2 Sensitivity mapping

Nagy et al. [97] proposed a multilevel design optimization scheme to transform the fine mesh sensitivity to the coarse mesh sensitivity, it is a good idea that can take into account both the exactness of the analysis and the definition of the design variables. With our method, the design variables not necessary to be the control points. Since we realized that

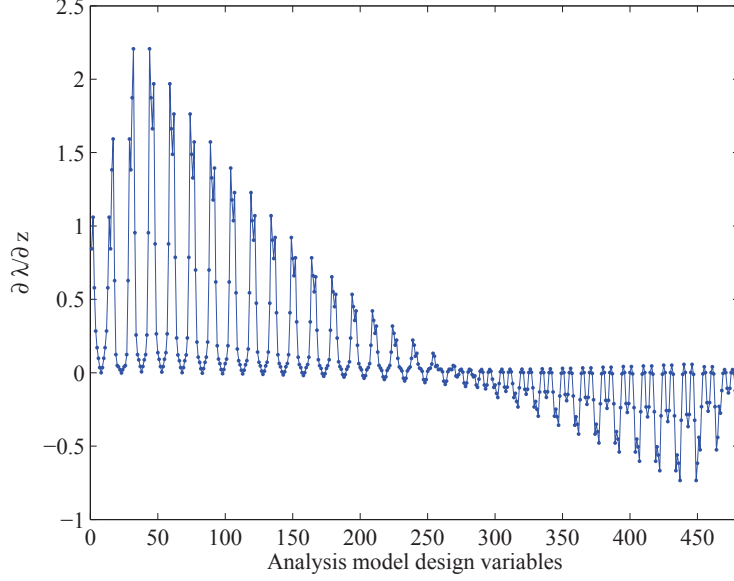


Figure 5.3: The objective function sensitivity w.r.t analysis model movable control point z coordinates.

the geometry change is finally reflected by the movement of the fine mesh model control points, any movement of a set of control points in the fine mesh level can be viewed as a design variable, no matter it is induced by an adjustment of the coarse mesh control points, a modification of the CAD model size or other user defined operations. We also give a FDM operation which is easy for obtaining this relationship. In this example, the design parameters are defined on the profile of the structure. The relationship between the design variables and the fine mesh control points attached design variables should be found. This relation reflects the effect the variation of the design variables on the variation of the fine mesh control points. As mentioned previously, this is the advantage that IGA brings, there is no such link in the FEM based optimization.

The geometric map can be obtained with analytical method or the finite difference method (FDM). The analytical method needs two steps as following,

$$\mathbf{g}_\lambda^c = \mathbf{T} \mathbf{g}_\lambda^f \quad (5.7)$$

$$g_{\lambda, z_i}^d = \sum_{i=1}^3 g_{\lambda, s_z}^{c, i(t)}. \quad (5.8)$$

Step 1: Map the sensitivity from the fine mesh to the coarse mesh. \mathbf{T} is a linear map obtained by the NURBS knot insertion algorithm.

Step 2: Map the control points attached design sensitivity to the design variables sensitivity. In the present example, equation (5.8) it is decided by the fact that this shell surface is an extrusion of the profile.

For complex structures, it is difficult to fix the map between design variables and the

control points attached design variables analytically, especially when the relationship is non-linear or the structure is complex, e.g. the design variable is the weight of the NURBS or the design variable is the radius of an arc. On the other hand, it is not a good choice to go deep into the NURBS operation. So the FDM can be used to obtain the geometric map in a single step. The relationship between the fine mesh sensitivity and the design variables is

$$\mathbf{g}_\lambda^d = \mathbf{T}_d \mathbf{g}_\lambda^f. \quad (5.9)$$

Here, \mathbf{T}_d is obtained by FDM. $[\mathbf{T}_d]_{ij}$ indicates that a unite movement of the i th design variable will lead to a $[\mathbf{T}_d]_{ij}$ movement on the j th fine mesh degrees of freedom. This is a pure geometric study, so it will not take too long time. This method is more practical for treating non-linear geometric map or complex structures. The design variables, no matter size or shape, as long as their movements can lead to the movements of the fine mesh control points, their sensitivity can be retraced by equation (5.9). In this sense, a design variable is a jointly movement of a set of control points.

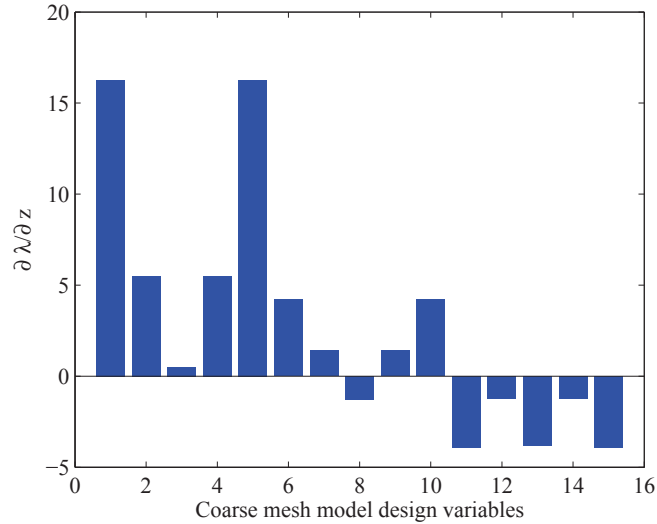


Figure 5.4: Coarse mesh model sensitivity.

Figure 5.4 shows the sensitivity with respect to the coarse meshed control points (15 design variables), obtained with equation (5.7). Figure 5.5 shows the final design variables sensitivity (5 design variables) obtained with equation (5.8).

We also use FDM method to obtain the geometrical map and then obtain the design sensitivity. With this method, we also test the sensitivity of the weight of z^3 attached control points, which is w^3 . In this case, the geometric map is non-linear, and we should calculate all the fine mesh sensitivities instead of only z coordinate sensitivity, since a movement of w^3 relates to the x, y, z movements of the fine mesh control points. We use a FDM step 10^{-6} to determine the geometrical map. The result as well as those from the full analytical result (no weight result) and the full FDM method (step 10^{-5}) are shown

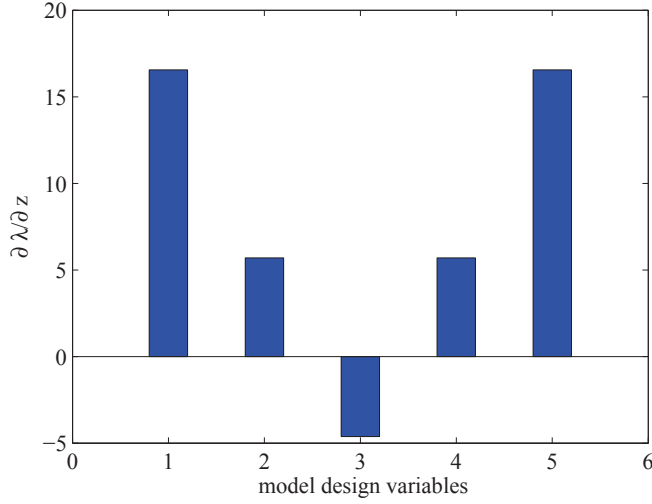


Figure 5.5: Design variables sensitivity.

in table 5.1. It can be seen the two analytical methods obtain the same results, they are reasonable in comparing with the full FDM.

Table 5.1: Design sensitivities obtained from the full FDM method, full analytical method (*Analytical₁*) and FDM-analytical method (*Analytical₂*).

	z^1	z^2	z^3	z^4	z^5	w^3
<i>FDM</i>	16.51388	5.690376	-4.635494	5.690507	16.51380	337.2663
<i>Analytical₁</i>	16.51392	5.690476	-4.635433	5.690476	16.51392	
<i>Analytical₂</i>	16.51392	5.690476	-4.635433	5.690476	16.51392	337.3304

5.3 Numerical examples

We give two examples to validate our method. Example one is a single patch free form surface design problem, its sensitivity evaluation procedure has been introduced before. The structure in example two is composed of two patches. The modal synthesis method is also used to improve the efficiency.

Example 1

The optimization setup was already described in the previous section. We use Matlab *fmincon* function to solve it. The algorithm is “active set” method. We provide the cost functions and their gradients (with full analytical sensitivity analysis). Figure 5.6 shows the optimum structure. Figure 5.7 shows the iteration history. Table 5.2 shows the related results obtained.

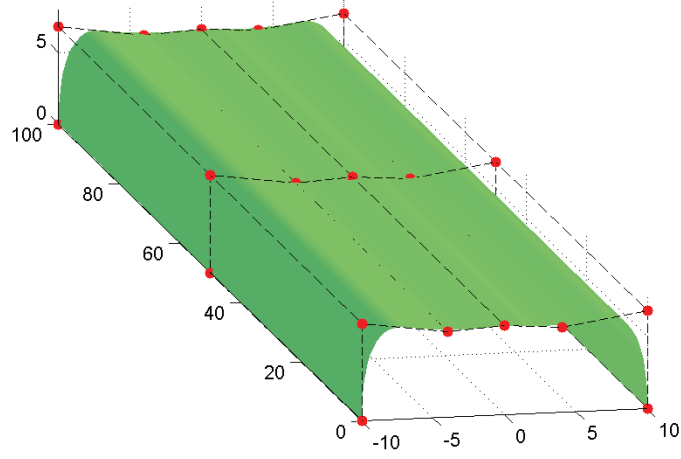


Figure 5.6: Example 1, the optimum shape obtained.

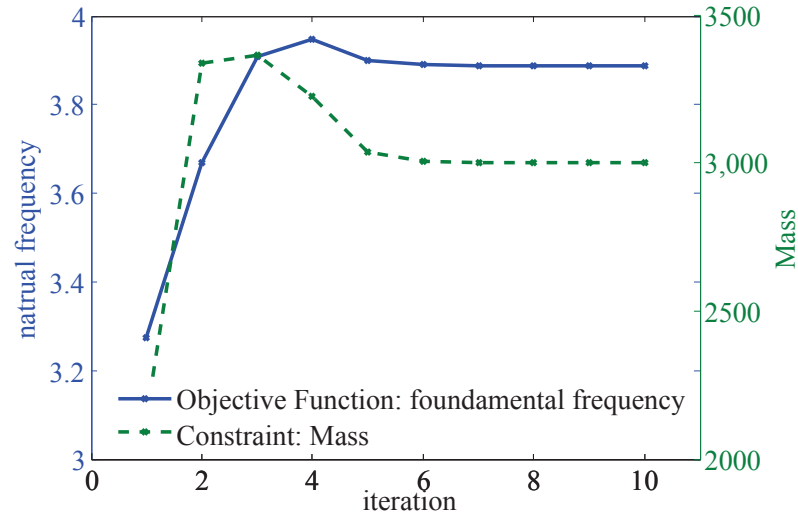


Figure 5.7: Example 1, the optimization iteration history.

Table 5.2: Example 1, The initial and optimum design variable values and the structural response.

	design variables	frequency	mass
initial	1, 2, 3, 2, 1	3.2752	2135.7
optimum	6.8403, 5.9856, 6.2363, 5.9856, 6.8403	3.8891	3000.0

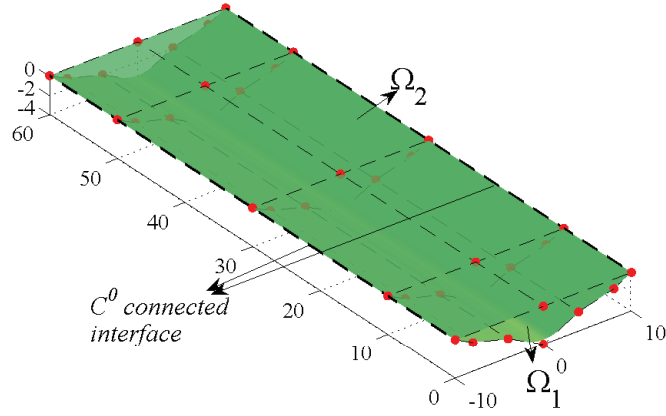


Figure 5.8: Example 2, the geometric model and the substructures.

Example 2

In this example, the structure is composed of two parts, depicted in figure 5.8. We want to maximize the fundamental frequency under mass and compliance constraints. The design parts and the design variables are the z coordinates of some control points, shown in figure 5.9. The analysis model and the analysis setup are shown in figure 5.10.

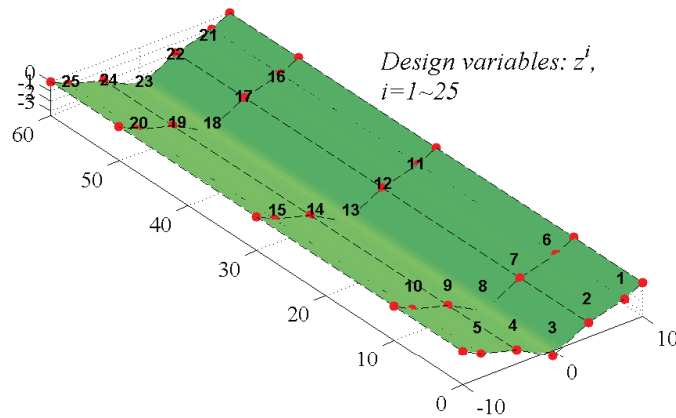


Figure 5.9: Example 2, the design part and the design variables.

The optimization problem is formulated as:

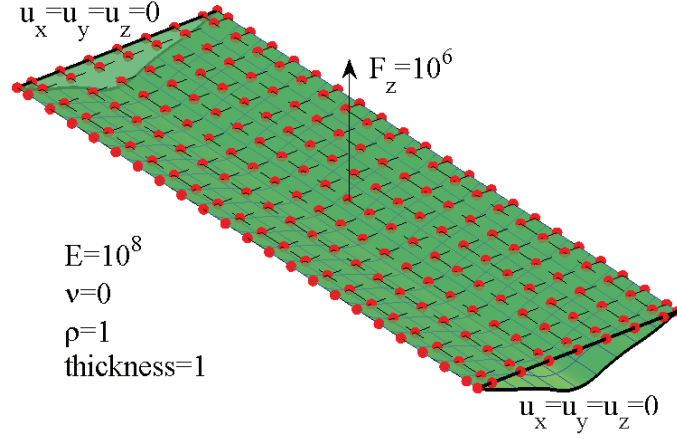


Figure 5.10: Example 2, the analysis model and the problem setup.

$$\begin{aligned}
 & \text{find } \mathbf{z} = [z_1, z_2, \dots, z_i] \\
 & \text{maximize } \lambda_1(\mathbf{z}) \\
 & \text{s.t. } m(\mathbf{z}) \leq m_d \\
 & C = \mathbf{u}^T \mathbf{K}(\mathbf{z}) \mathbf{u} \leq C_d \\
 & \mathbf{K}(\mathbf{z}) \mathbf{u} = \mathbf{F} \\
 & \begin{cases} \mathbf{K}(\mathbf{z}) \mathbf{u}_1 = \lambda_1 \mathbf{M}(\mathbf{z}) \mathbf{u}_1 \\ \mathbf{u}_1^T \mathbf{M} \mathbf{u}_1 = 1 \\ \mathbf{u}_1^T \mathbf{K} \mathbf{u}_1 = \lambda_1 \end{cases}
 \end{aligned} \tag{5.10}$$

In addition to the previously defined constraints, here we also introduce static analysis equation and structure compliance constraints. The substructure Ω_2 is simplified with the pre-mentioned modal synthesis method with only the first 10 fixed interface modes. The degrees of freedom are reduced from 621 to 136, the finer the mesh is, the larger the reduction can be achieved.

The structure compliance sensitivity is

$$C, = -\mathbf{u}^T \mathbf{K}, \mathbf{u}. \tag{5.11}$$

In the present optimization, we set $C_d = 8 \times 10^5$ and $m_d = 2700$. The *fmincon* function in Matlab is also used here, we choose “active set” method. Table 5.3 shows the relevant quantities. Figure 5.11, 5.12 and 5.13 show the iteration history of the cost functions. Figure 5.14 shows the optimum structure shape.

5. SHAPE OPTIMIZATION

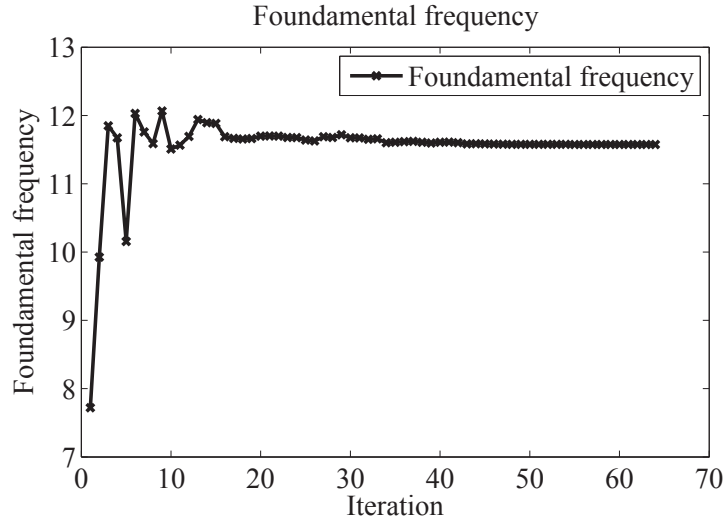


Figure 5.11: Example 2, The optimization history of the objective function.

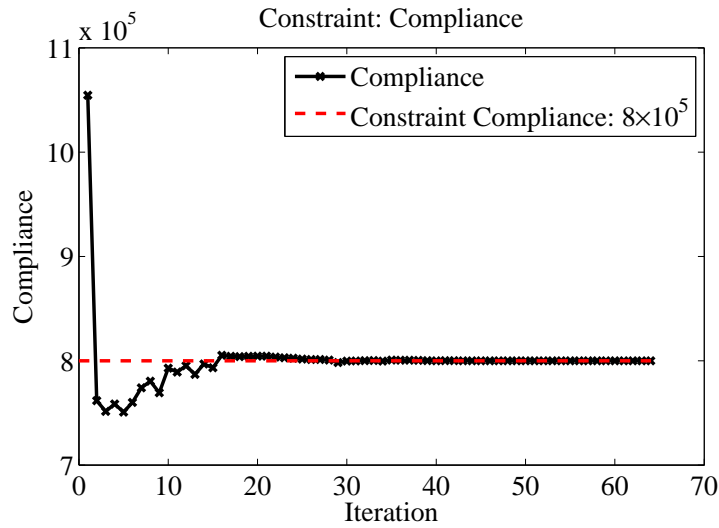


Figure 5.12: Example 2, The optimization history of the compliance constraint.

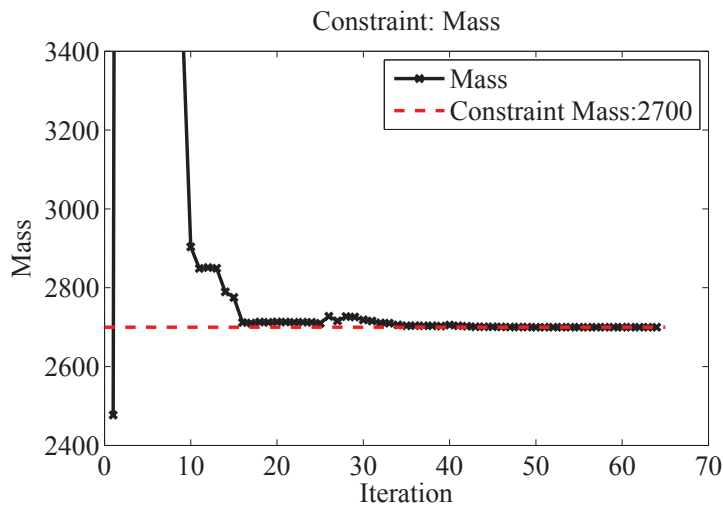


Figure 5.13: Example 2, The optimization history of the mass constraint.

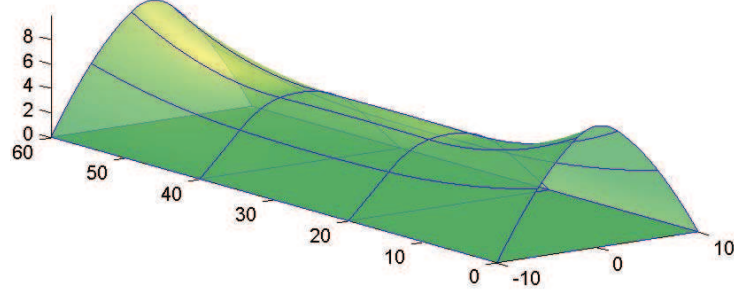


Figure 5.14: Example 2, the optimum structure shape.

Table 5.3: Example 2, the initial and optimum design variable values and the structural response.

	design variables	frequency	mass	compliance
initial	-1,-2,-4,-2,-1,-1,-2,-4,-2,-1,-1,-2,-4 -2,-1,-1,-2,-4,-2,-1,-1,-2,-4,-2,-1	7.7210	2477.0	1.0546×10^6
optimum	3.1609, 7.8490, 10.601, 7.8490, 3.1609 2.0118, 5.4873, 5.5142, 5.4873, 2.0118 1.3932, 5.0478, 6.4851, 5.0478, 1.3932 2.0118, 5.4873, 5.5142, 5.4873, 2.0118 3.1609, 7.8490, 10.6005, 7.8490, 3.1609	11.5760	2700.0	8.0×10^5

Discussion

The optimization framework proposed is flexible for treating various design variables. The bottom structure ingredients sensitivities are evaluated simultaneously with the structure ingredients, they share a lot of intermediate variables, so it will save the computer resource. After this step, the structure ingredients' sensitivity with respect to all degrees of freedom are obtained. Based on them, the sensitivity map transforms the bottom sensitivity to the user defined variables. The user only needs to define the design variables by defining sensitivity map. It also enables the user to adjust the selection of design variables during the iteration, the only thing they need to do is provide a new sensitivity map. The framework is suitable for commercial software.

5.4 Summary

In this chapter, we present a framework for three dimensional shell shape optimization with isogeometric Kirchhoff-Love shell elements. We give a new sensitivity evaluation method. It makes the framework general and flexible. We also use modal synthesis method to avoid a repeated evaluation of the unchanging parts of the structure, only the parts where the design variables are defined are reanalyzed, the full structure response is

5. SHAPE OPTIMIZATION

evaluated with modal synthesis of the substructures. It further improves the efficiency. With the help of IGA method, the optimum structure obtained is a CAD model, which is more manufacturable. The method is suitable for dealing large scale optimization problem concerning structural dynamics criteria.

Chapter 6

Conclusion

6.1 Conclusions

In this thesis, we studied the IGA shell structure analysis and optimization problem. Both the Kirchhoff-Love shell and the Reissner-Mindlin shell are studied. Our focus is on the Reissner-Mindlin shell. We propose mixed grid formulations that can give a natural way to define the fiber directors in IGA Reissner-Mindlin shell. A modified reduced quadrature scheme is also developed to relieve the transverse shear locking and improve the numerical quadrature efficiency. The ultimate aim of our research is to develop a fast shape optimization framework for shell structure optimization concerning structural dynamics aspects. To achieve this goal, the classical modal synthesis method, which is widely used in the structural dynamic analysis, is also studied. A methodology for evaluating the analytical design sensitivity is also developed. The optimization framework proposed is suitable for shell shape design problems with large number of design variables. The results show the effectiveness of the methods.

6.1.1 Mixed grid IGA Reissner-Mindlin shell

A series of mixed grid Reissner-Mindlin shell formulations is developed. It adopts both the interpolatory basis functions, which are from the traditional FEM, and the non-interpolatory basis functions, which are from IGA, to approximate the unknown fields. It gives a natural way to define the fiber vectors in the IGA Reissner-Mindlin shell formulations, where the non-interpolatory nature of IGA basis functions causes complexity.

A modified quadrature scheme is also proposed for our formulations. It is inspired by the particularities the IGA basis functions own. Our quadrature scheme takes into account both the basis function support intervals and their cross element regularity. It can improve the quadrature efficiency without introducing “hourglass” modes. It can also relieve the transverse shear locking in the present formulations.

6.1.2 Modal synthesis with Isogeometric shell elements

We use the classical fixed interface Craig-Bampton method as well as the IGA Kirchhoff-Love shell elements for model reduction. The key problem is the coupling of substructures. It is also a key step for the IGA analysis on multiple domains. We propose a easy method to achieve the patch coupling in IGA analysis. It lays a solid foundation for the optimization of built-up structure, since only the relevant substructures need to be reanalyzed.

6.1.3 IGA based shape optimization

We propose a framework for fast free form surface optimization. The surfaces are modelled with IGA Kirchhoff-Love shell elements. The focus is on the sensitivity analysis. We give a new method to evaluate the design sensitivity analytically. There are normally two models for optimization problem, the design model and the analysis model. They carry the same geometry information. The design model is capable of implementing the analysis directly, however, it is normally too coarse to give reasonable results. On the other hand, the design sensitivity should be obtained from the analysis model. The design variables are defined on the design model. To solve the above problems, we give a sensitivity mapping method. It can extract the design sensitivity from the mesh level analytical sensitivity which is obtained from the analysis model. It enables a flexible design variable definition as well as a reliable structural response evaluation. We use such method as well as the previously introduced modal synthesis method to optimize the built-up structures. It can improve the optimization efficiency.

6.2 Future work

In this thesis, the IGA shell elements developed are all for linear analysis. In industrial applications, large deformation nonlinear shell elements are widely used, like in the inflatable structures. The geometrical nonlinear effect should be taken into consideration. On other hand, the fiber reinforced material is often used in shell structures, its material model needs to be studied and incorporated into shell formulations in order to analyse such type of structures. We could also further optimize the layer stacking of the composite shell structures.

The optimization framework developed can be directly used for some shell optimization problems in the present state. We give examples on natural frequency optimization. As for the sensitivity analysis, the framework proposed is general enough for obtaining the sensitivity of the linear structural analysis ingredients. However, there are various types of cost functions in industrial optimization, such as stress and surface curvature. Their sensitivities should also be considered in the future. Considering the diversity of the cost

functions, it might be difficult to obtain the analytical design sensitivities for every cost function. It might be promising to use the analytical sensitivity and numerical sensitivities simultaneously in the optimization.

The multidisciplinary optimization could also be studied in the future. The engineering problems normally involves many subjects, we should consider many criteria to give a reasonable design. As for the shell shape optimization, it could be used in the design of automotive, the aerodynamic performance should also be considered. At the same time, IGA method use geometrically exact model in the analysis, it might be advantageous to optimize the criteria considering fluid-structure interaction. As for the structural dynamics optimization, we only optimize the natural frequency of the structure. The optimization of modal shapes and harmonic responses could also be studied in the future. They are also of great importance in the real engineering design.

CONCLUSION

Appendix

The implementation of modal synthesis

The full structure Ω is partitioned into N non-overlapping substructures $\Omega = \bigcup_{s=1}^N \Omega^s$. The modal analysis equation for the full structure is

$$\mathbf{M}\ddot{\mathbf{u}} + \mathbf{K}\mathbf{u} = \mathbf{0}. \quad (1)$$

The discrete control equation for substructure Ω^s is

$$\begin{bmatrix} \mathbf{M}_{ii}^s & \mathbf{M}_{ib}^s \\ \mathbf{M}_{bi}^s & \mathbf{M}_{bb}^s \end{bmatrix} \begin{Bmatrix} \ddot{\mathbf{u}}_i^s \\ \ddot{\mathbf{u}}_b^s \end{Bmatrix} + \begin{bmatrix} \mathbf{K}_{ii}^s & \mathbf{K}_{ib}^s \\ \mathbf{K}_{bi}^s & \mathbf{K}_{bb}^s \end{bmatrix} \begin{Bmatrix} \mathbf{u}_i^s \\ \mathbf{u}_b^s \end{Bmatrix} = \begin{Bmatrix} \mathbf{0} \\ \mathbf{F}_b^s \end{Bmatrix}. \quad (2)$$

The footnotes i and b denote the inner nodes and interface nodes related terms respectively. \mathbf{F}_b^s is the interaction force on the interfaces. The procedures of modal synthesis are detailed in the following.

The fixed interface modes

The fixed interface modes are obtained by implementing the following modal analysis

$$\mathbf{M}_{ii}^s \ddot{\mathbf{u}}_i^s + \mathbf{K}_{ii}^s \mathbf{u}_i^s = \mathbf{0}. \quad (3)$$

The eigenvectors are $\boldsymbol{\phi}_j$, $j = 1 \sim i$. Only the first k eigenvectors, $\boldsymbol{\phi}^s = \{\boldsymbol{\phi}_1, \boldsymbol{\phi}_2, \dots, \boldsymbol{\phi}_k\}$, are used to formulate the fixed interface modes as following

$$\boldsymbol{\Phi}_N^s = \begin{bmatrix} \boldsymbol{\phi}^s \\ \mathbf{0} \end{bmatrix}. \quad (4)$$

The constraint modes

The constraint modes are obtained by solving the following static problem

$$\mathbf{K}_{ib}^s \mathbf{u}_b^s + \mathbf{K}_{ii}^s \mathbf{u}_i^s = \mathbf{0}. \quad (5)$$

The linear relation between \mathbf{u}_b^s and \mathbf{u}_i^s can be obtained as

$$\begin{Bmatrix} \mathbf{u}_i^s \\ \mathbf{u}_b^s \end{Bmatrix} = \begin{bmatrix} -(\mathbf{K}_{ii}^s)^{-1} \mathbf{K}_{ib}^s \\ \mathbf{I} \end{bmatrix} \{\mathbf{u}_b^s\}. \quad (6)$$

And the constraint modes are defined as

$$\Phi_c^s = \begin{bmatrix} \phi_c^s \\ \mathbf{I} \end{bmatrix} = \begin{bmatrix} -(\mathbf{K}_{ii}^s)^{-1} \mathbf{K}_{ib}^s \\ \mathbf{I} \end{bmatrix}. \quad (7)$$

The reduced substructure model

The transformation matrix for model reduction is composed by the fixed interface normal modes and the constraint modes.

$$\Phi^s = \{\Phi_N^s, \Phi_c^s\}. \quad (8)$$

The physical coordinates are expressed by mode coordinate as $\mathbf{u}^s = \Phi^s \mathbf{p}^s$. \mathbf{p}^s is the mode coordinate, it includes the inner mode coordinate \mathbf{p}_k^s and interface coordinate \mathbf{u}_b^s .

$$\begin{Bmatrix} \mathbf{u}_i^s \\ \mathbf{u}_b^s \end{Bmatrix} = \begin{bmatrix} \phi^s & \phi_c^s \\ \mathbf{0} & \mathbf{I} \end{bmatrix} \begin{Bmatrix} \mathbf{p}_k^s \\ \mathbf{u}_b^s \end{Bmatrix}. \quad (9)$$

The reduced equation is obtained as

$$\bar{\mathbf{M}}^s \ddot{\mathbf{p}}^s + \bar{\mathbf{K}}^s \mathbf{p}^s = \mathbf{g}^s. \quad (10)$$

The reduced ingredients are

$$\bar{\mathbf{M}}^s = (\Phi^s)^T \mathbf{M}^s \Phi^s, \quad (11)$$

$$\bar{\mathbf{K}}^s = (\Phi^s)^T \mathbf{K}^s \Phi^s, \quad (12)$$

$$\mathbf{g}^s = \left[\mathbf{0}, (\mathbf{F}_b^s)^T \right]^T. \quad (13)$$

Substructure coupling

The simplified substructures should be coupled to get the global equation. For substructures A and B, their reduced equations are

$$\begin{bmatrix} \bar{\mathbf{M}}_{kk}^A & \bar{\mathbf{M}}_{kb}^A \\ \bar{\mathbf{M}}_{bk}^A & \bar{\mathbf{M}}_{bb}^A \end{bmatrix} \begin{Bmatrix} \ddot{\mathbf{p}}^A \\ \ddot{\mathbf{u}}_b^A \end{Bmatrix} + \begin{bmatrix} \bar{\mathbf{K}}_{kk}^A & \bar{\mathbf{K}}_{kb}^A \\ \bar{\mathbf{K}}_{bk}^A & \bar{\mathbf{K}}_{bb}^A \end{bmatrix} \begin{Bmatrix} \mathbf{p}^A \\ \mathbf{u}_b^A \end{Bmatrix} = \begin{Bmatrix} \mathbf{0} \\ \mathbf{F}_b^A \end{Bmatrix}, \quad (14)$$

$$\begin{bmatrix} \bar{\mathbf{M}}_{kk}^B & \bar{\mathbf{M}}_{kb}^B \\ \bar{\mathbf{M}}_{bk}^B & \bar{\mathbf{M}}_{bb}^B \end{bmatrix} \begin{Bmatrix} \ddot{\mathbf{p}}^B \\ \ddot{\mathbf{u}}_b^B \end{Bmatrix} + \begin{bmatrix} \bar{\mathbf{K}}_{kk}^B & \bar{\mathbf{K}}_{kb}^B \\ \bar{\mathbf{K}}_{bk}^B & \bar{\mathbf{K}}_{bb}^A \end{bmatrix} \begin{Bmatrix} \mathbf{p}^B \\ \mathbf{u}_b^B \end{Bmatrix} = \begin{Bmatrix} \mathbf{0} \\ \mathbf{F}_b^B \end{Bmatrix}. \quad (15)$$

After interface coupling, the reduced system equation is

$$\bar{\mathbf{M}}\ddot{\mathbf{q}} + \bar{\mathbf{K}}\mathbf{q} = \mathbf{0}. \quad (16)$$

In the C^0 connected interface case, where the adjacent substructures can rotate along the interface, only those degrees of freedoms which are on the interface are considered as interface degree of freedom. With the displacement relation that $\mathbf{u}_b^A = \mathbf{u}_b^B$, we can get the ingredients detailed as following

$$\mathbf{q} = \left\{ (\mathbf{p}^A)^T, (\mathbf{p}^B)^T, (\mathbf{u}_b^A)^T \right\}^T \quad (17)$$

$$\bar{\mathbf{M}} = \begin{bmatrix} \bar{\mathbf{M}}_{kk}^A & \mathbf{0} & \bar{\mathbf{M}}_{kb}^A \\ \mathbf{0} & \bar{\mathbf{M}}_{ll}^B & \bar{\mathbf{M}}_{lb}^B \\ \bar{\mathbf{M}}_{bk}^A & \bar{\mathbf{M}}_{bl}^B & \bar{\mathbf{M}}_{bb}^A + \bar{\mathbf{M}}_{bb}^B \end{bmatrix} \quad (18)$$

$$\bar{\mathbf{K}} = \begin{bmatrix} \bar{\mathbf{K}}_{kk}^A & \mathbf{0} & \bar{\mathbf{K}}_{kk}^A \\ \mathbf{0} & \bar{\mathbf{K}}_{ll}^B & \bar{\mathbf{K}}_{lb}^B \\ \bar{\mathbf{K}}_{kk}^A & \bar{\mathbf{K}}_{bl}^B & \bar{\mathbf{K}}_{bb}^A + \bar{\mathbf{K}}_{bb}^B \end{bmatrix}. \quad (19)$$

In the rigid connected interface case, the first column of control points near the adjacent interface are also considered as interface nodes. Here, there are two types of interface nodes for each substructure, the nodes which are on the interface are noted by b_0 , the first column of nodes close to the interface are noted by b_1 . Firstly, we couple the adjacent substructure's b_0 type degrees of freedom in the way that we did in the C^0 case. Then, we use bending strip method to take into account the bending stiffness along the interfaces. Hence, the connection operation here is implemented among the parts A, B and the virtual bending strip.

The virtual strip's degrees of freedoms also belong to the two adjacent substructures, we arrange them in the sequence such that they correspond to the substructure A's first column control points near the interface, substructure B's first column control points near the interface, and the substructure A's control points on the interface sequentially. It is detailed as following

$$\mathbf{u}^V = \{\mathbf{u}_{b_1}^{VA}, \mathbf{u}_{b_1}^{VB}, \mathbf{u}_{b_0}^V\}. \quad (20)$$

Its stiffness matrix will be partitioned into nine parts correspondingly as

$$\mathbf{K}^V = \begin{bmatrix} \mathbf{K}_{b_1 b_1}^{VA} & \mathbf{K}_{b_1 b_1}^{VAB} & \mathbf{K}_{b_1 b_0}^{VA} \\ \mathbf{K}_{b_1 b_1}^{VAB} & \mathbf{K}_{b_1 b_1}^{VB} & \mathbf{K}_{b_1 b_0}^{VB} \\ \mathbf{K}_{b_0 b_1}^{VA} & \mathbf{K}_{b_0 b_1}^{VB} & \mathbf{K}_{b_0 b_0}^V \end{bmatrix}. \quad (21)$$

The substructure B's degrees of freedoms which are on the interface are condensed out. The remaining interface degrees of freedom are reinforced by the strip's stiffness matrix. The final ingredients are

$$\mathbf{q} = \left\{ (\mathbf{p}^A)^T, (\mathbf{p}^B)^T, (\mathbf{u}_{b_1}^A)^T, (\mathbf{u}_{b_1}^B)^T, (\mathbf{u}_{b_0}^A)^T \right\}^T \quad (22)$$

$$\bar{\mathbf{M}} = \begin{bmatrix} \bar{\mathbf{M}}_{kk}^A & \mathbf{0} & \bar{\mathbf{M}}_{kb_1}^A & \mathbf{0} & \bar{\mathbf{M}}_{kb_0}^A \\ \mathbf{0} & \bar{\mathbf{M}}_{ll}^B & \mathbf{0} & \bar{\mathbf{M}}_{lb_1}^B & \bar{\mathbf{M}}_{lb_0}^B \\ \bar{\mathbf{M}}_{b_1 k}^A & \mathbf{0} & \bar{\mathbf{M}}_{b_1 b_1}^A & \mathbf{0} & \bar{\mathbf{M}}_{b_1 b_0}^A \\ \mathbf{0} & \bar{\mathbf{M}}_{b_1 l}^B & \mathbf{0} & \bar{\mathbf{M}}_{b_1 b_1}^B & \bar{\mathbf{M}}_{b_1 b_0}^B \\ \bar{\mathbf{M}}_{b_0 k}^A & \bar{\mathbf{M}}_{b_0 l}^B & \bar{\mathbf{M}}_{b_0 b_1}^A & \bar{\mathbf{M}}_{b_0 b_1}^B & \bar{\mathbf{M}}_{b_0 b_0}^A + \bar{\mathbf{M}}_{b_0 b_0}^B \end{bmatrix} \quad (23)$$

$$\bar{\mathbf{K}} = \begin{bmatrix} \bar{\mathbf{K}}_{kk}^A & \mathbf{0} & \bar{\mathbf{K}}_{kb_1}^A & \mathbf{0} & \bar{\mathbf{K}}_{kb_0}^A \\ \mathbf{0} & \bar{\mathbf{K}}_{ll}^B & \mathbf{0} & \bar{\mathbf{K}}_{lb_1}^B & \bar{\mathbf{K}}_{lb_0}^B \\ \bar{\mathbf{K}}_{b_1 k}^A & \mathbf{0} & \bar{\mathbf{K}}_{b_1 b_1}^A + \bar{\mathbf{K}}_{b_1 b_1}^{VA} & \bar{\mathbf{K}}_{b_1 b_1}^{VAB} & \bar{\mathbf{K}}_{b_1 b_0}^A + \bar{\mathbf{K}}_{b_1 b_0}^{VA} \\ \mathbf{0} & \bar{\mathbf{K}}_{b_1 l}^B & \bar{\mathbf{K}}_{b_1 b_1}^{VAB} & \bar{\mathbf{K}}_{b_1 b_1}^B + \bar{\mathbf{K}}_{b_1 b_1}^{VB} & \bar{\mathbf{K}}_{b_1 b_0}^B + \bar{\mathbf{K}}_{b_1 b_0}^{VB} \\ \bar{\mathbf{K}}_{b_0 k}^A & \bar{\mathbf{K}}_{b_0 l}^B & \bar{\mathbf{K}}_{b_0 b_1}^A + \bar{\mathbf{K}}_{b_0 b_1}^{VA} & \bar{\mathbf{K}}_{b_0 b_1}^B + \bar{\mathbf{K}}_{b_0 b_1}^{VB} & \bar{\mathbf{K}}_{b_0 b_0}^A + \bar{\mathbf{K}}_{b_0 b_0}^B + \bar{\mathbf{K}}_{b_0 b_0}^V \end{bmatrix}. \quad (24)$$

Reconstruction

After solving the reduced equation (16), we can obtain the condensed response field \mathbf{q} . The initial variable \mathbf{u} can be reconstructed in the sequence $\mathbf{q} \rightarrow \mathbf{p} \rightarrow \mathbf{u}$.

In the first reconstruction step $\mathbf{q} \rightarrow \mathbf{p}$, the relation $\mathbf{u}_b^A = \mathbf{u}_b^B$ or $\mathbf{u}_{b_0}^A = \mathbf{u}_{b_0}^B$ should be used. In the second step $\mathbf{p} \rightarrow \mathbf{u}$, the physical displacement field can be reconstructed with the help of the reduced modes in equation (9).

References

- [1] URL http://carat.st.bv.tum.de/caratuserswiki/index.php/Users:Structural_Optimization/General_Formulation. xiii, 6
- [2] C Adam, S Bouabdallah, M Zarroug, and H Maitournam. Improved numerical integration for locking treatment in isogeometric structural elements, part i: Beams. *Comput. Meth. Appl. Mech. Eng.*, 279:1–28, 2014. 65, 70, 71
- [3] C Adam, S Bouabdallah, M Zarroug, and H Maitournam. Improved numerical integration for locking treatment in isogeometric structural elements. part ii: Plates and shells. *Comput. Meth. Appl. Mech. Eng.*, 284:106–137, 2015. 62, 65, 67, 70, 71
- [4] Love AEH. On the small vibrations and deformations of thin elastic shells. *Philos. Trans. R. Soc.*, 179:491, 1888. 2
- [5] S Ahmad, BM Irons, and OC Zienkiewicz. Analysis of thick and thin shell structures by curved elements. *Int. J. Numer. Methods Eng*, 2:419–451, 1970. 2
- [6] Sohrabuddin Ahmad, Bruce M Irons, and Olgierd C Zienkiewicz. Curved thick shell and membrane elements with particular reference to axisymmetric problems. Technical report, DTIC Document, 1968. 2
- [7] Jalal Akbari, Nam H Kim, and MT Ahmadi. Shape sensitivity analysis with design-dependent loadingsequivalence between continuum and discrete derivatives. *Struct Multidiscip O*, 40(1-6):353–364, 2010. 113
- [8] Andreas Apostolatos, Robert Schmidt, Roland Wüchner, and Kai-Uwe Bletzinger. A nitsche-type formulation and comparison of the most common domain decomposition methods in isogeometric analysis. *Int. J. Numer. Methods Eng.*, 97(7): 473–504, 2014. 79
- [9] F Auricchio, L Beirão da Veiga, TJR Hughes, A Reali, and G Sangalli. Isogeometric collocation for elastostatics and explicit dynamics. *Comput. Meth. Appl. Mech. Eng.*, 249:2–14, 2012. 78

REFERENCES

- [10] F Auricchio, Francesco Calabro, TJR Hughes, A Reali, and G Sangalli. A simple algorithm for obtaining nearly optimal quadrature rules for nurbs-based isogeometric analysis. *Comput. Meth. Appl. Mech. Eng.*, 249:15–27, 2012. [59](#), [68](#), [70](#)
- [11] MCC Bampton and JR RR Craig, R. Coupling of substructures for dynamic analyses. *AIAA Journal*, 6(7):1313–1319, 1968. [95](#)
- [12] Robert E Barnhill and Richard F Riesenfeld. *Computer aided geometric design*. Academic Press, 2014. [23](#)
- [13] Timothy J Barth. Numerical methods for gasdynamic systems on unstructured meshes. In *An introduction to recent developments in theory and numerics for conservation laws*, pages 195–285. Springer, 1999. [3](#)
- [14] Y Bazilevs, L Beirao da Veiga, JA Cottrell, TJR Hughes, and G Sangalli. Isogeometric analysis: approximation, stability and error estimates for h-refined meshes. *Math. Models Methods Appl. Sci.*, 16(07):1031–1090, 2006. [4](#)
- [15] Y Bazilevs, VM Calo, TJR Hughes, and Y Zhang. Isogeometric fluid-structure interaction: theory, algorithms, and computations. *Comput. Mech.*, 43(1):3–37, 2008. [4](#), [34](#)
- [16] Yuri Bazilevs and Thomas JR Hughes. Weak imposition of dirichlet boundary conditions in fluid mechanics. *Computers & Fluids*, 36(1):12–26, 2007. [36](#)
- [17] Yuri Bazilevs, Victor M Calo, John A Cottrell, John A Evans, TJR Hughes, S Lipton, MA Scott, and TW Sederberg. Isogeometric analysis using t-splines. *Comput. Meth. Appl. Mech. Eng.*, 199(5):229–263, 2010. [4](#), [78](#)
- [18] LOURENCO Beirão da Veiga, A Buffa, D Cho, and G Sangalli. Isogeometric analysis using t-splines on two-patch geometries. *Comput. Meth. Appl. Mech. Eng.*, 200(21):1787–1803, 2011. [78](#)
- [19] Ted Belytschko, Henryk Stolarski, Wing Kam Liu, Nicholas Carpenter, and Jame SJ Ong. Stress projection for membrane and shear locking in shell finite elements. *Comput. Meth. Appl. Mech. Eng.*, 51(1):221–258, 1985. [42](#), [52](#), [92](#)
- [20] DJ Benson, Y Bazilevs, MC Hsu, and TJR Hughes. Isogeometric shell analysis: the reissner–mindlin shell. *Comput. Meth. Appl. Mech. Eng.*, 199(5):276–289, 2010. [xiv](#), [39](#), [54](#), [55](#), [56](#), [58](#)
- [21] DJ Benson, Y Bazilevs, M-C Hsu, and TJR Hughes. A large deformation, rotation-free, isogeometric shell. *Comput. Meth. Appl. Mech. Eng.*, 200(13):1367–1378, 2011. [39](#), [40](#)

-
- [22] DJ Benson, S Hartmann, Y Bazilevs, M-C Hsu, and TJR Hughes. Blended isogeometric shells. *Comput. Meth. Appl. Mech. Eng.*, 255:133–146, 2013. [39](#)
- [23] M Bischoff, K-U Bletzinger, WA Wall, and E Ramm. Models and finite elements for thin-walled structures. *Encyclopedia of computational mechanics*, 2004. [3](#), [12](#), [21](#), [65](#)
- [24] Kai-Uwe Bletzinger, Manfred Bischoff, and Ekkehard Ramm. A unified approach for shear-locking-free triangular and rectangular shell finite elements. *Computers & Structures*, 75(3):321–334, 2000. [65](#)
- [25] Wolfgang Boehm. Inserting new knots into b-spline curves. 1980. [24](#), [32](#)
- [26] Robin Bouclier, Thomas Elguedj, and Alain Combescure. Locking free isogeometric formulations of curved thick beams. *Comput. Meth. Appl. Mech. Eng.*, 245:144–162, 2012. [65](#)
- [27] Robin Bouclier, Thomas Elguedj, and Alain Combescure. On the development of nurbs-based isogeometric solid shell elements: 2d problems and preliminary extension to 3d. *Comput. Mech.*, 52(5):1085–1112, 2013. [65](#)
- [28] Robin Bouclier, Thomas Elguedj, and Alain Combescure. Efficient isogeometric nurbs-based solid-shell elements: Mixed formulation and-method. *Comput. Meth. Appl. Mech. Eng.*, 267:86–110, 2013. [39](#), [42](#), [54](#)
- [29] A Buffa, G Sangalli, and R Vázquez. Isogeometric analysis in electromagnetics: B-splines approximation. *Comput. Meth. Appl. Mech. Eng.*, 199(17):1143–1152, 2010. [4](#), [34](#)
- [30] Scott A Burns. *Recent advances in optimal structural design*. ASCE Publications, 2002. [6](#)
- [31] Rui PR Cardoso and JMA Cesar de Sa. The enhanced assumed strain method for the isogeometric analysis of nearly incompressible deformation of solids. *Int. J. Numer. Methods Eng.*, 92(1):56–78, 2012. [65](#)
- [32] Dominique Chapelle and Klaus-Jürgen Bathe. Fundamental considerations for the finite element analysis of shell structures. *Computers & Structures*, 66(1):19–36, 1998. [2](#)
- [33] Seonho Cho and Seung-Hyun Ha. Isogeometric shape design optimization: exact geometry and enhanced sensitivity. *Struct Multidiscip O*, 38(1):53–70, 2009. [95](#), [113](#)
- [34] Kyung K Choi and Nam-Ho Kim. *Structural sensitivity analysis and optimization 1: linear systems*. Springer Science & Business Media, 2006. [6](#), [112](#), [113](#)

REFERENCES

- [35] Elaine Cohen, Tom Lyche, and Richard Riesenfeld. Discrete b-splines and subdivision techniques in computer-aided geometric design and computer graphics. *Comput Vision Graph*, 14(2):87–111, 1980. [3](#), [24](#), [32](#), [80](#)
- [36] Steven A Coons. Surfaces for computer aided design. Technical report, Technical report, 1964. [23](#)
- [37] J Austin Cottrell, Thomas JR Hughes, and Yuri Bazilevs. *Isogeometric analysis: toward integration of CAD and FEA*. John Wiley & Sons, 2009. [xiii](#), [xix](#), [4](#), [7](#), [36](#), [109](#)
- [38] JA Cottrell, A Reali, Y Bazilevs, and TJR Hughes. Isogeometric analysis of structural vibrations. *Comput. Meth. Appl. Mech. Eng.*, 195(41):5257–5296, 2006. [4](#), [78](#)
- [39] JA Cottrell, TJR Hughes, and A Reali. Studies of refinement and continuity in isogeometric structural analysis. *Comput. Meth. Appl. Mech. Eng.*, 196(41):4160–4183, 2007. [78](#), [79](#), [109](#)
- [40] Maurice G Cox. The numerical evaluation of b-splines. *IMA J. Appl. Math.*, 10(2):134–149, 1972. [3](#), [23](#)
- [41] R Craig and C-J Chang. Free-interface methods of substructure coupling for dynamic analysis. *AIAA Journal*, 14(11):1633–1635, 1976. [95](#)
- [42] Roy R Craig. Coupling of substructures for dynamic analyses: an overview. In *Proceedings of AIAA/ASME/ASCE/AHS/ASC structures, structural dynamics, and materials conference and exhibit*, pages 1573–1584, 2000. [95](#)
- [43] RR Craig. Substructure methods in vibration. *J. Vib. Acoust.*, 117(B):207–213, 1995. [95](#)
- [44] A Curnier. On three modal synthesis variants. *J. Sound Vib.*, 90(4):527–540, 1983. [95](#)
- [45] Kirchhoff G. Uber das. Gleichgewicht und die bewegung einer elastischen scheibe. *J. Reine Angew. Math.*, 40:51–58, 1850. [2](#)
- [46] Carl De Boor. On calculating with b-splines. *J Approx Theory*, 6(1):50–62, 1972. [3](#), [23](#)
- [47] Carl De Boor. A practical guide to splines. *Math. Comput.*, 1978. [3](#), [32](#)
- [48] Tor Dokken, Tom Lyche, and Kjell Fredrik Pettersen. Polynomial splines over locally refined box-partitions. *Comput Aided Geom D*, 30(3):331–356, 2013. [4](#), [78](#)

-
- [49] W Dornisch and S Klinkel. Treatment of reissner–mindlin shells with kinks without the need for drilling rotation stabilization in an isogeometric framework. *Comput. Meth. Appl. Mech. Eng.*, 276:35–66, 2014. [39](#)
 - [50] W Dornisch, S Klinkel, and B Simeon. Isogeometric reissner–mindlin shell analysis with exactly calculated director vectors. *Comput. Meth. Appl. Mech. Eng.*, 253: 491–504, 2013. [xiv](#), [xv](#), [39](#), [49](#), [50](#), [52](#), [53](#), [54](#), [55](#), [56](#), [57](#), [58](#)
 - [51] Reissner E. The effect of transverse shear deformation on the bending of elastic plates. *J. Appl. Mech.*, 12:69C76, 1945. [2](#)
 - [52] R Echter, B Oesterle, and M Bischoff. A hierarchic family of isogeometric shell finite elements. *Comput. Meth. Appl. Mech. Eng.*, 254:170–180, 2013. [39](#), [65](#)
 - [53] Ralph Echter and Manfred Bischoff. Numerical efficiency, locking and unlocking of nurbs finite elements. *Comput. Meth. Appl. Mech. Eng.*, 199(5):374–382, 2010. [65](#)
 - [54] T Elguedj, Y Bazilevs, VM Calo, and TJR Hughes. B^- and f^- projection methods for nearly incompressible linear and non-linear elasticity and plasticity using higher-order nurbs elements. *Comput. Meth. Appl. Mech. Eng.*, 197(33-40):2732–2762, 2008. [65](#)
 - [55] Anand Embar, John Dolbow, and Isaac Harari. Imposing dirichlet boundary conditions with nitsche’s method and spline-based finite elements. *Int. J. Numer. Methods Eng.*, 83(7):877–898, 2010. [79](#)
 - [56] Gerald Farin, J Hoschek, and MS Kim. A history of curves and surfaces in cagd. *Handbook of Computer Aided Geometric Design*, pages 1–23, 2002. [23](#)
 - [57] Carlos A Felippa. Introduction to finite element methods. *University of Colorado, Boulder*, [http://www. colorado. edu/engineering/CAS/courses. d/IFEM. d](http://www.colorado.edu/engineering/CAS/courses.d/IFEM.d), 2004. [84](#)
 - [58] J.C. Ferguson. Multivariable curve interpolation. *Journal of ACM*, (2):221–228, 1964. [23](#)
 - [59] J.C. Ferguson. Multivariable curve interpolation. *Report D2-22504*, 43(4):67–97, 1990. [23](#)
 - [60] A Robin Forrest. Interactive interpolation and approximation by bézier polynomials. *The Computer Journal*, 15(1):71–79, 1972. [23](#), [24](#), [32](#)
 - [61] Alexander IJ Forrester and Andy J Keane. Recent advances in surrogate-based optimization. *Prog. Aerosp. Sci.*, 45(1):50–79, 2009. [6](#)

REFERENCES

- [62] Carlotta Giannelli, Bert Jüttler, and Hendrik Speleers. Thb-splines: The truncated basis for hierarchical splines. *Comput Aided Geom D*, 29(7):485–498, 2012. [4](#), [78](#)
- [63] Ronald N Goldman and Tom Lyche. *Knot insertion and deletion algorithms for B-spline curves and surfaces*, volume 36. SIAM, 1993. [32](#)
- [64] Héctor Gómez, Victor M Calo, Yuri Bazilevs, and Thomas JR Hughes. Isogeometric analysis of the cahn–hilliard phase-field model. *Comput. Meth. Appl. Mech. Eng.*, 197(49):4333–4352, 2008. [34](#), [36](#)
- [65] Hector Gomez, Thomas JR Hughes, Xesús Nogueira, and Victor M Calo. Isogeometric analysis of the isothermal navier–stokes–korteweg equations. *Comput. Meth. Appl. Mech. Eng.*, 199(25):1828–1840, 2010. [4](#), [34](#)
- [66] William J Gordon. *Free-form surface interpolation through curve networks*. Research Laboratories, General Motors Corporation, 1969. [23](#)
- [67] William J Gordon. Spline-blended surface interpolation through curve networks. *J Math Mech*, 18(10):931, 1969. [23](#)
- [68] William J Gordon and Richard F Riesenfeld. B-spline curves and surfaces. *Comput Aided Geom D*, 167:95, 1974. [23](#)
- [69] Robert J Guyan. Reduction of stiffness and mass matrices. *AIAA journal*, 3(2):380–380, 1965. [95](#)
- [70] ZOO-HWAN Hah, HYUN-JUNG Kim, J.-Y., and SUNG-KIE Youn, S.-K. A hierarchically superimposing local refinement method for isogeometric analysis. *Int. J. Comput. Methods*, 2013. [78](#)
- [71] R Hauptmann and K Schweizerhof. A systematic development of solid-shell element formulations for linear and non-linear analyses employing only displacement degrees of freedom. *Int. J. Numer. Methods Eng.*, 42(1):49–69, 1998. [2](#)
- [72] Kristian Holm-Jørgensen and Søren RK Nielsen. A component mode synthesis algorithm for multibody dynamics of wind turbines. *J. Sound Vib.*, 86(3):753–767, 2009. [95](#)
- [73] Saman Hosseini, Joris JC Remmers, Clemens V Verhoosel, and René Borst. An isogeometric solid-like shell element for nonlinear analysis. *Int. J. Numer. Methods Eng.*, 95(3):238–256, 2013. [39](#)
- [74] SN Hou. Review of modal synthesis techniques and a new approach. *Shock and vibration bulletin*, 40(4):25–39, 1969. [95](#)

-
- [75] Ming-Chen Hsu and Yuri Bazilevs. Fluid–structure interaction modeling of wind turbines: simulating the full machine. *Comput. Mech.*, 50(6):821–833, 2012. [78](#)
- [76] Qi-Xing Huang, Shi-Min Hu, and Ralph R Martin. Fast degree elevation and knot insertion for b-spline curves. *Comput Aided Geom D*, 22(2):183–197, 2005. [32](#)
- [77] Thomas JR Hughes. *The finite element method: linear static and dynamic finite element analysis*. Courier Corporation, 2012. [21](#), [45](#), [47](#), [48](#), [65](#)
- [78] Thomas JR Hughes and Wing Kam Liu. Nonlinear finite element analysis of shells: Part i. three-dimensional shells. *Comput. Meth. Appl. Mech. Eng.*, 26(3):331–362, 1981. [2](#)
- [79] Thomas JR Hughes, John A Cottrell, and Yuri Bazilevs. Isogeometric analysis: Cad, finite elements, nurbs, exact geometry and mesh refinement. *Comput. Meth. Appl. Mech. Eng.*, 194(39):4135–4195, 2005. [xiii](#), [3](#), [4](#), [32](#), [36](#), [95](#)
- [80] Thomas JR Hughes, A Reali, and G Sangalli. Efficient quadrature for nurbs-based isogeometric analysis. *Comput. Meth. Appl. Mech. Eng.*, 199(5):301–313, 2010. [59](#), [68](#)
- [81] Walter C Hurty. Dynamic analysis of structural systems using component modes. *AIAA journal*, 3(4):678–685, 1965. [95](#)
- [82] Walter C Hurty, Jon D Collins, and Gary C Hart. Dynamic analysis of large structures by modal synthesis techniques. *Computers & Structures*, 1(4):535–563, 1971. [95](#)
- [83] L Jezequel and HD Seito. Component modal synthesis methods based on hybrid models, part i: Theory of hybrid models and modal truncation methods. *J. Appl. Mech.*, 61(1):100–108, 1994. [95](#)
- [84] L Jezequel and HD Setio. Component modal synthesis methods based on hybrid models, part ii: Numerical tests and experimental identification of hybrid models. *J. Appl. Mech.*, 61(1):109–116, 1994. [95](#)
- [85] J. Kiendl. *Isogeometric analysis and shape optimal design of shell structures*. PhD thesis, Technical University of Munich, 2011. [85](#)
- [86] J Kiendl, K-U Bletzinger, J Linhard, and R Wüchner. Isogeometric shell analysis with kirchhoff–love elements. *Comput. Meth. Appl. Mech. Eng.*, 198(49):3902–3914, 2009. [39](#), [40](#), [42](#), [54](#), [85](#), [90](#), [92](#)

REFERENCES

- [87] J Kiendl, Y Bazilevs, M-C Hsu, R Wüchner, and K-U Bletzinger. The bending strip method for isogeometric analysis of kirchhoff–love shell structures comprised of multiple patches. *Comput. Meth. Appl. Mech. Eng.*, 199(37):2403–2416, 2010. [xvii](#), [40](#), [78](#), [86](#), [90](#), [92](#), [98](#)
- [88] Stefan K Kleiss, Clemens Pechstein, Bert Jüttler, and Satyendra Tomar. Ieti-isogeometric tearing and interconnecting. *Comput. Meth. Appl. Mech. Eng.*, 2012. [78](#)
- [89] D de Klerk, DJ Rixen, and SN Voormeeren. General framework for dynamic substructuring: history, review and classification of techniques. *AIAA journal*, 46(5): 1169–1181, 2008. [95](#)
- [90] Sven Klinkel and Sanjay Govindjee. Using finite strain 3d-material models in beam and shell elements. *Eng Computation*, 19(8):902–921, 2002. [2](#)
- [91] Yanan Liu, Liang Sun, Yinghua Liu, and Zhangzhi Cen. Multi-scale b-spline method for 2-d elastic problems. *Appl. Math. Modell.*, 35(8):3685–3697, 2011. [78](#)
- [92] Jia Lu. Isogeometric contact analysis: Geometric basis and formulation for frictionless contact. *Comput. Meth. Appl. Mech. Eng.*, 200(5):726–741, 2011. [4](#), [34](#)
- [93] Richard H MacNeal. A hybrid method of component mode synthesis. *Computers & Structures*, 1(4):581–601, 1971. [95](#)
- [94] Richard H Macneal. A simple quadrilateral shell element. *Computers & Structures*, 8(2):175–183, 1978. [2](#)
- [95] Rubin MB. *Cosserat Theoris: Shells, Rods and Points*. Kluwer, 2000. [2](#)
- [96] Attila P Nagy, Mostafa M Abdalla, and Zafer Gürdal. Isogeometric sizing and shape optimisation of beam structures. *Comput. Meth. Appl. Mech. Eng.*, 199(17): 1216–1230, 2010. [109](#)
- [97] Attila P Nagy, Samuel T IJsselmuiden, and Mostafa M Abdalla. Isogeometric design of anisotropic shells: optimal form and material distribution. *Comput. Meth. Appl. Mech. Eng.*, 264:145–162, 2013. [109](#), [110](#), [113](#)
- [98] N Nguyen-Thanh, H Nguyen-Xuan, Stephane Pierre Alain Bordas, and T Rabczuk. Isogeometric analysis using polynomial splines over hierarchical t-meshes for two-dimensional elastic solids. *Comput. Meth. Appl. Mech. Eng.*, 200(21):1892–1908, 2011. [4](#), [78](#)
- [99] Ahmed K Noor and W Scott Burton. Assessment of shear deformation theories for multilayered composite plates. *Appl. Mech. Rev.*, 42(1):1–13, 1989. [21](#)

-
- [100] Ahmed K Noor and W Scott Burton. Assessment of computational models for multilayered composite shells. *Appl. Mech. Rev*, 43(4):67–97, 1990. [21](#)
 - [101] Byong-Ug Park, Yu-Deok Seo, Ole Sigmund, and Sung-Kie Youn. Shape optimization of the stokes flow problem based on isogeometric analysis. *Struct Multidiscip O*, 48(5):965–977, 2013. [110](#)
 - [102] THH Pian and K Sumihara. Rational approach for assumed stress finite elements. *Int. J. Numer. Methods Eng.*, 20(9):1685–1695, 1984. [65](#)
 - [103] L Piegl and W Tiller. The nurbs book. monograph in visual communication. *Springer-Verleg*, 1997. [32](#)
 - [104] Les A Piegl and Wayne Tiller. *The NURBS book*. Springer, 1997. [82](#)
 - [105] Hartmut Prautzsch and Bruce Piper. A fast algorithm to raise the degree of spline curves. *Comput Aided Geom D*, 8(4):253–265, 1991. [24](#), [32](#)
 - [106] Xiaoping Qian. Full analytical sensitivities in nurbs based isogeometric shape optimization. *Comput. Meth. Appl. Mech. Eng.*, 199(29):2059–2071, 2010. [95](#), [109](#), [113](#)
 - [107] Nestor V Queipo, Raphael T Haftka, Wei Shyy, Tushar Goel, Rajkumar Vaidyanathan, and P Kevin Tucker. Surrogate-based analysis and optimization. *Prog. Aerosp. Sci.*, 41(1):1–28, 2005. [6](#)
 - [108] Mindlin RD. Influence of rotatory inertia and shear flexural motions of isotropic elastic plates. *J. Appl. Mech.*, 18:31C38, 1951. [2](#)
 - [109] Junuthula Narasimha Reddy. *Theory and analysis of elastic plates and shells*. CRC press, 2006. [16](#), [19](#)
 - [110] Richard Franklin Riesenfeld. Applications of b-spline approximation to geometric problems of computer-aided design. 1973. [3](#)
 - [111] David F Rogers. *An introduction to NURBS: with historical perspective*. Elsevier, 2000. [3](#), [24](#)
 - [112] George IN Rozvany. A critical review of established methods of structural topology optimization. *Struct Multidiscip O*, 37(3):217–237, 2009. [6](#)
 - [113] Martin Ruess, Dominik Schillinger, Ali I Özcan, and Ernst Rank. Weak coupling for isogeometric analysis of non-matching and trimmed multi-patch geometries. *Comput. Meth. Appl. Mech. Eng.*, 269:46–71, 2014. [79](#)

REFERENCES

- [114] Kazuhiro Saitou, Kazuhiro Izui, Shinji Nishiwaki, and Panos Papalambros. A survey of structural optimization in mechanical product development. *J. Comput. Inf. Sci. Eng.*, 5(3):214–226, 2005. [5](#)
- [115] Dominik Schillinger, John A Evans, Alessandro Reali, Michael A Scott, and Thomas JR Hughes. Isogeometric collocation: cost comparison with galerkin methods and extension to adaptive hierarchical nurbs discretizations. *Comput. Meth. Appl. Mech. Eng.*, 267:170–232, 2013. [71](#)
- [116] Dominik Schillinger, Shaikh J Hossain, and Thomas JR Hughes. Reduced bézier element quadrature rules for quadratic and cubic splines in isogeometric analysis. *Comput. Meth. Appl. Mech. Eng.*, 277:1–45, 2014. [68](#), [70](#)
- [117] R Schmidt, J Kiendl, K-U Bletzinger, and R Wüchner. Realization of an integrated structural design process: analysis-suitable geometric modelling and isogeometric analysis. *Comput. Visual. Sci.*, 13(7):315–330, 2010. [77](#)
- [118] Robert Schmidt, Roland Wüchner, and Kai-Uwe Bletzinger. Isogeometric analysis of trimmed nurbs geometries. *Comput. Meth. Appl. Mech. Eng.*, 241:93–111, 2012. [78](#)
- [119] I.J. Schoenberg. On spline function. *O. eds. Inequalities*, 1967. [23](#)
- [120] Thomas W Sederberg, Jianmin Zheng, Almaz Bakenov, and Ahmad Nasri. T-splines and t-nurccs. In *ACM transactions on graphics (TOG)*, volume 22, pages 477–484. ACM, 2003. [24](#)
- [121] Thomas W Sederberg, David L Cardon, G Thomas Finnigan, Nicholas S North, Jianmin Zheng, and Tom Lyche. T-spline simplification and local refinement. In *ACM Transactions on Graphics (TOG)*, volume 23, pages 276–283. ACM, 2004. [24](#)
- [122] S Shojaee, E Izadpanah, N Valizadeh, and J Kiendl. Free vibration analysis of thin plates by using a nurbs-based isogeometric approach. *Finite Elem. Anal. Des.*, 61: 23–34, 2012. [78](#)
- [123] Juan C Simo and David D Fox. On a stress resultant geometrically exact shell model. part i: Formulation and optimal parametrization. *Comput. Meth. Appl. Mech. Eng.*, 72(3):267–304, 1989. [2](#)
- [124] Juan C Simo and MS Rifai. A class of mixed assumed strain methods and the method of incompatible modes. *Int. J. Numer. Methods Eng.*, 29(8):1595–1638, 1990. [3](#)
- [125] Timoshenko SP. *History of Strength of Materials*. McGraw-Hill, 1953. [1](#), [2](#)

-
- [126] J.N. Goodier S.P. Timoshenko. *Theory of Elasticity, third ed.*, McGraw-Hill, 1970. 86
- [127] Gary Mitchel Stanley. Continuum-based shell elements. *Dissertation Abstracts International Part B: Science and Engineering*[DISS. ABST. INT. PT. B- SCI. & ENG.], 46(12), 1986. 3
- [128] Shlomo Taasan. Introduction to shape design and control. URL: <http://www.math.cmu.edu/shlomo/VKI-Lectures/lecture1/index.html>, 2001. 110
- [129] Stephen Timoshenko, Sergius Woinowsky-Krieger, and S Woinowsky-Krieger. *Theory of plates and shells*, volume 2. McGraw-hill New York, 1959. 65
- [130] Tae-Kyoung Uhm and Sung-Kie Youn. T-spline finite element method for the analysis of shell structures. *Int. J. Numer. Methods Eng.*, 80(4):507–536, 2009. 39, 49
- [131] F Van Keulen, RT Haftka, and NH Kim. Review of options for structural design sensitivity analysis. part 1: Linear systems. *Comput. Meth. Appl. Mech. Eng.*, 194(30):3213–3243, 2005. 112
- [132] Kenneth James Versprille. Computer-aided design applications of the rational b-spline approximation form. 1975. 3, 24
- [133] A-V Vuong, Carlotta Giannelli, Bert Jüttler, and Bernd Simeon. A hierarchical approach to adaptive local refinement in isogeometric analysis. *Comput. Meth. Appl. Mech. Eng.*, 200(49):3554–3567, 2011. 4, 78
- [134] Wolfgang A Wall, Moritz A Frenzel, and Christian Cyron. Isogeometric structural shape optimization. *Comput. Meth. Appl. Mech. Eng.*, 197(33):2976–2988, 2008. 109, 113
- [135] Dongdong Wang and Junchang Xuan. An improved nurbs-based isogeometric analysis with enhanced treatment of essential boundary conditions. *Comput. Meth. Appl. Mech. Eng.*, 199(37):2425–2436, 2010. 34, 36
- [136] Ping Wang, Jinlan Xu, Jiansong Deng, and Falai Chen. Adaptive isogeometric analysis using rational pht-splines. *Comput.-Aided Des.*, 43(11):1438–1448, 2011. 4, 78
- [137] Minho Yoon, Seung-Hyun Ha, and Seonho Cho. Isogeometric shape design optimization of heat conduction problems. *Int. J. Heat Mass Transfer*, 62:272–285, 2013. 113

REFERENCES

- [138] Shiwei Zhou and Michael Yu Wang. Multimaterial structural topology optimization with a generalized cahn–hilliard model of multiphase transition. *Struct Multidiscip O*, 33(2):89–111, 2007. [36](#)
- [139] J Zhu, ZRL Taylor, and OC Zienkiewicz. The finite element method: its basis and fundamentals, 2005. [45](#), [48](#), [79](#), [85](#)
- [140] OC Zienkiewicz, RL Taylor, and JM Too. Reduced integration technique in general analysis of plates and shells. *Int. J. Numer. Methods Eng.*, 3(2):275–290, 1971. [2](#), [65](#)
- [141] Olek C Zienkiewicz and Robert L Taylor. *The finite element method for solid and structural mechanics*. Butterworth-heinemann, 2005. [59](#), [60](#), [61](#)

AUTORISATION DE SOUTENANCE

Vu les dispositions de l'arrêté du 7 août 2006,

Vu la demande du Directeur de Thèse

Monsieur L. JEZEQUEL

et les rapports de

Monsieur S. COGAN
Chargé de Recherche HDR - FEMTP-ST - Département Mécanique Appliquée - 24 chemin de l'Epitaphe
25000 Besançon

Et de

Monsieur T. TISON
Professeur - LAMIH - UMR CNRS-UVHC 8201 - Université de Valenciennes - Le Mont Houy - Bât. CISIT
59313 Valenciennes cedex 9

Monsieur LEI Zhen

est autorisé à soutenir une thèse pour l'obtention du grade de **DOCTEUR**

Ecole doctorale MECANIQUE , ENERGETIQUE, GENIE CIVIL ET ACOUSTIQUE

Fait à Ecully, le 9 octobre 2015

P/Le directeur de l'E.C.L.
La directrice des Etudes

